PTF and EHT
Research on hot Subdwarf B stars

-Masterarbeit aus der Physik-

Markus Schindewolf

Dr. Karl Remeis-Sternwarte Bamberg
Astronomisches Institut der
Friedrich-Alexander-Universität
Erlangen-Nürnberg
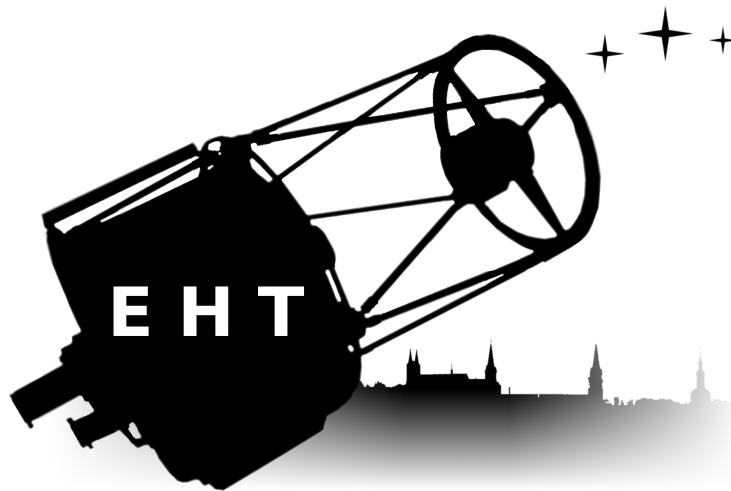
27.11.2014

Betreuer: Herr Prof. Dr. Ulrich Heber

Abstract

This thesis consists of two primary parts.

At first it deals with the installation, setup and scientific usage of the Ernst-Hartwig-Telescope (EHT) at the Remeis Observatory in Bamberg. After the description of the adjustment process and the presentation of the results, the conducted photometric observations are explained. To determine the accuracy of the photometry, results have been compared to data from a larger telescope. The telescope was used to provide eclipse timing to contribute to searches for exoplanets. A total of 15 mid eclipse timings of six different targets have been measured to search for variations in the orbital period of binaries by using O-C diagrams. For one target, V470 Cam, such a diagram could be computed from EHT data only. In addition one target was checked for brightness fluctuations in course of the MUCHFUSS project. At the end, a new photometric follow-up campaign is presented.

In the second part a binary system discovered by the Palomar Transient Factory was analysed from light- and radial velocity curves using, beside others, the MORO code. PTF 072456+125301 is a subdwarf B star with a faint companion. From the lightcurve an orbital period of $0.0997 \pm 0.00005\,\mathrm{d}$ and an inclination of $83.56 \pm 0.3°$ is derived. The radial velocity curve revealed a semi-amplitude of $K_1 = 101.25 \pm 3.2\,\mathrm{km\ s^{-1}}$. The mass of the primary was determined to $0.526\,\mathrm{M_\odot}$. From the analysis of blue spectra, a temperature of $34000\,\mathrm{K}$ and a surface gravity of $\log g = 5.74$ was found. The companion does not contribute to the optical light, except through the reflection effect. Its mass is about $0.174\mathrm{M_\odot}$. Therefore it is considered an M-dwarf. This indicates that the system is of HW Vir type, number 15 of its class.

Abstract

Die vorliegende Masterarbeit gliedert sich in zwei Teile.

Zum Einen wird das Ernst-Hartwig-Teleskop (EHT) der Remeis Sternwarte in Bamberg behandelt. Nach der Beschreibung der Justage und der Präsentation der hierbei erreichten Resultate werden die mit dem Gerät durchgeführten, photometrischen Messungen erläutert. Um die Genauigkeit dieser Beobachtungen einschätzen zu können, wurden die Ergebnisse mit Messdaten größerer, professioneller Forschungsteleskope verglichen. Das Teleskop wurde dazu genutzt Bedeckungszeiten von Binärsystemen zu messen um damit zur Suche nach Exoplaneten beizutragen. Insgesamt wurden 15 Zeitpunkte der maximalen Bedeckung von sechs verschiedenen Systemen bestimmt um nach Abweichungen in der Periodenlänge mittels O-C Diagrammen zu suchen. Für ein System, V470 Cam, konnte ein solches Diagramm allein aus Daten erstellt werden die mit dem EHT gewonnen wurden. Des weiteren wurde ein Objekt, im Rahmen des MUCHFUSS Projekts, auf Helligkeitsschwankungen hin untersucht. Am Schluss wird eine neue, photometrische Beobachtungskampagne präsentiert.

Der zweite große Teil der Arbeit bestand in der Analyse eine Binärsystems, welches von der Palomar Transient Factory entdeckt wurde. Bei PTF 072456+125301 handelt es sich um einen Subdwarf B Stern mit einem leuchtschwachen Begleiter. Aus der Lichtkurve wurde eine Periode von 0.0997 ± 0.00005 d und eine Inklination von $83.56 \pm 0.3°$ ermittelt. Aus der Radialgeschwindigkeitskurve folgte eine Halbamplitude von $K_1 = 101.25 \pm 3.2$ km s^{-1}. Die Masse des Primärsterns wurde zu 0.526 M$_\odot$ bestimmt. Aus der Analyse der blauen Spektren ergab sich eine Temperatur von 34000 K und eine Schwerebeschleunigung von log g $= 5.74$. Bis auf einen ausgeprägten Reflektionseffekt trägt der Begleitstern nicht zum optischen Gesamtfluss bei. Er hat eine Masse von ca. 0.174M$_\odot$. Dies begründet die Annahme dass es sich um einen M-Zwerg handelt. Damit lässt sich schlussfolgern, dass es sich bei PTF0724 um ein HW Vir System, das 15. dieser Art, handelt.

Contents

X

1. Introduction

The Remeis Observatory in Bamberg was founded in 1886. It is named after Dr. Karl Remeis, a wealthy lawyer. He had a strong interest in science, especially in astronomy. In his own words,

[Astronomy] is the science helping the people to find the right awareness of themselves and their place in the universe, but at the same time enables them to find the eternal laws of outer space, rethink the thought of creation and feel a godly spark inside.

Dr. Karl Remeis

In his last will he donated most of his money to the city of Bamberg to build an observatory. The construction was finished in 1889 and Ernst Hartwig became the first director. His main research interest focused on variable stars. Observations were made with the telescopes mounted in both domes and other instruments in the meridian hall.

The second director, Ernst Zinner, turned the Bamberg photometric sky patrol into a large collaborative project with observatories in Sonneberg and Berlin-Babelsberg. As it became very hard to acquire enough money to keep the institute running, director Wolfgang Strohmeier decided to cooperate with the University of Erlangen and in 1962 the observatory became the official astronomical institute of the University Erlangen-Nürnberg.

Over the years the sky conditions for observations in Bamberg became worse and with the technical abilities of those times it was no longer worthwhile to spend time and money on them. Instead it was decided to set up an observing station at Boyden, South Africa. Observations there continued till 1974 and resulted in a large amount of photographic plates which analysis continues until today. The decision to start the ESO meant the end for small monitoring campaigns like the one in Boyden. In our times, roughly 50 years after the last observations in Bamberg, there have been vast changes in the technical possibilities regarding telescopes, mounts and cameras. These changes were encouraging enough to give scientific observations a chance again. Despite the erection of huge facilities, small telescopes, like the new one in Bamberg, can contribute to scientific results, in particular when long series of observations are required.

An archetype for observations with comparatively small telescopes was found in the DWARF project. The aim was to find evidence for exoplanets in the orbit around or both stars. Exoplanets have been a hot topic for several years now and the number of new discoveries rapidly grows.The monitored systems are binaries systems consisting of two stars. In addition nearly all systems contained an sdB star. Despite being studied for several decades now, sdB stars are not yet completely understood and are still subject of several research projects.

But possible planets are not the only interesting thing about binaries. They offer a variety of possibilities regarding their analysis and the derivable parameters. Therefore such a system is described and analyzed in detail in the last chapter, presenting

moderns methods of analysis, based on high quality data gained with large, modern telescopes.

The other parts of this thesis deal with the observations made in Bamberg with the Ernst-Hartwig-Telescope (EHT) and describes them in detail. Furthermore theoretical foundation for understanding the objects of interest is presented, followed by a detailed description of the new technical accouterments.

2. Fundamental theory

In this chapter, some fundamental groundwork for understanding binaries, with or without subdwarf B stars (sdBs hereafter) will be explained. At first, different types of binaries and their characteristic properties will be explained. Thereafter the main methods of analyzing for those systems are described. At the end an overview of sdB stars is presented, followed by a short summary on the detection of unseen companions, in particular extrasolar planets, in binary systems.

2.1. Binaries

While looking at the night sky, most stars that can be seen appear to be single ones. But in reality, the majority of stars in our galaxy are located in binaries - two stars in an orbit around the common center of mass. Most of them are not optically resolvable, even with the largest of today's telescopes.

However, binaries play an important role in modern astrophysics. They allow us to measure and estimate fundamental parameters of the stars, especially their masses and radii. For the determination of the mass, it is necessary that the object gravitationally interacts with an other object. The other object can be another star, a planet, or even something exotic like a black hole. By knowing the mass of a star (together with some other parameters), we can make profound statements about its age or its evolution.

For a single star however, we can only conduct a spectroscopic analysis of the stellar light and derive the effective temperature of the star, the chemical abundances and the surface gravity. But only in combination with the examination of double stars, we are able to draw a complete picture of what is going on in the nightsky.

Of course, there are different types of binaries that all differ from each other by certain properties.

In general, double stars can be divided in wide- and close binaries. In wide binaries the distance between the stars is so large that they do not affect each others evolution or appearance. The most famous example is probably β Cygnus, called Albireo.

In close binaries, the stars can interact with each other, e.g. by mass transfer, radiation or magnetic fields. This significantly changes their evolutionary paths. But close binary systems are more uncommon than wide system.

In the following, a general model to describe binary systems, the Roche Model, is presented. Thereafter different types and appearances of double stars will be presented.

2.1.1. Roche model

Especially close binary systems are hard to describe due to the influence each star has onto its companion. A suitable model, that takes the ellipsoidal deformation caused

by tidal forces into account, is the Roche Model (named after Edouard Albert Roche, 1820 - 1883). It is based on the common three-body-problem. Several assumptions are made to simplify the model:

- All stars are treated as point masses

- The stars move on circular orbits around their common center of mass

- The rotational axis of the stars are perpendicular to the orbital plane

- The rotation of the stars is synchronized to the orbit (bound rotation). However this is irrelevant for point masses.

If we assume that the two stars are separated by a distance a and are at position r_1 and r_2 with respect to the center of mass, the following equations holds.

$$r_1 + r_2 = a \tag{2.1}$$

and

$$M_1 r_1 = M_2 r_2 \tag{2.2}$$

The effective gravitational potential Φ can be calculated to

$$\Phi = -G \frac{M_1}{s_1} - \frac{M_2}{s_2} - \frac{\omega^2}{2} r^2 \tag{2.3}$$

In this step, the centrifugal potential $\frac{1}{2}\omega^2 r^2$ was included and the following abbreviations were used.

$$\omega^2 = \frac{G(M_1 + M_2)}{a^3} \tag{2.4}$$

$$r_x = r_x^2 + r^2 + 2r_x r \cos \Theta \tag{2.5}$$

and

$$s_y^2 = r_y^2 + r^2 - 2r_y r \cos \Theta \tag{2.6}$$

Figure 2.1 shows a graphical representation of the co-rotating coordinate system. To describe a star system surfaces with the same Roche potential, the equipotential surfaces, can be used. Figure 2.2 shows such a Roche potential and the equipotential surfaces as well as the five Lagrangian points.

2.1.2. Visual and astrometric binaries

The first class of systems are visual binaries. In these systems each component of the system can be resolved with a telescope or even with the naked eye. If one component is too dark to be seen, one can provide evidence for the second component nevertheless. As both stars orbit around their common center of mass, the visible star seems to undergo a periodic movement. In this case the system is called „astrometric binary". A famous example is Sirius A, the brightest star in the night sky. It is accompanied by a white dwarf, Sirius B, whose existence could only be verified by observing the track of Sirius A and the small, periodic variations caused by the white dwarf companion. Figure 2.3 shows the observed trajectories of the two stars over several decades.
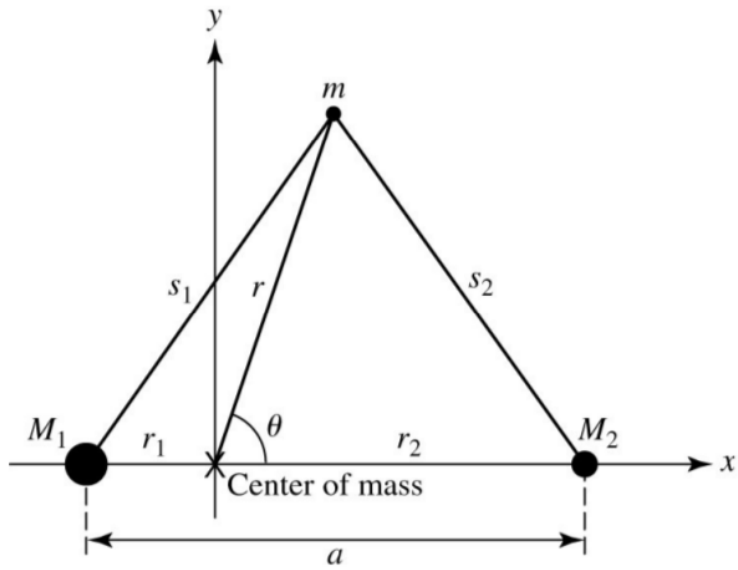
Figure 2.1.: Co-rotating coordinate system in a binary[1]
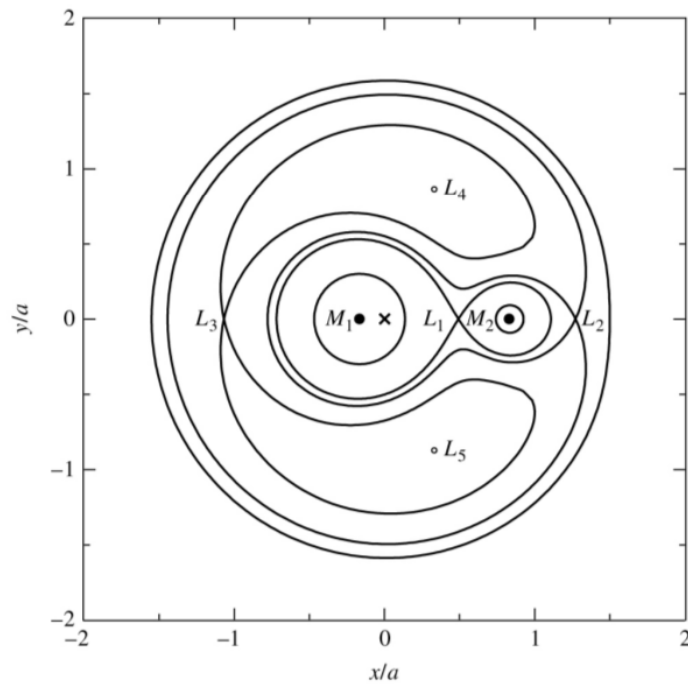
Figure 2.2.: Equipotential surface in a binary[1]

Statements on the total mass of the two stars can be made if its is possible to measure the system's period P, its semi-major axis a and the parallax p. By using Kepler's third law and inserting the observed parameters, the total mass can be

---

[1][Carroll and Ostlie, 2007]
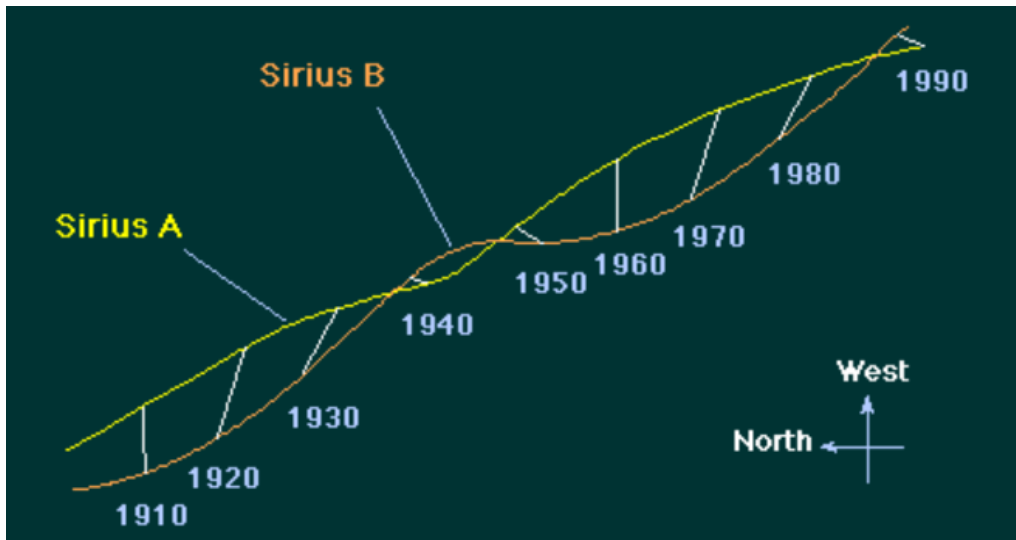
Figure 2.3.: Trajectories of Sirius A + B [1]

calculated.

$$M_1 + M_2 = \frac{P^2 a^3}{p^3} \tag{2.7}$$

If both semimajor axes and the inclinations of a visual binary can be measured, both masses can be calculated separately.

2.1.3. Spectroscopic binaries

If a binary system cannot be resolved optically but shows periodic variations in the position of spectral lines, it is called a spectroscopic binary. When two stars are in an orbit around each other, there are phases when one star moves towards the observer and phases when it veers away from him. Because of the Doppler effect, this movement causes changes in the wavelength of the emitted light. It can be described via

$$\frac{\Delta\lambda}{\lambda} = \frac{v}{c}\sin i \tag{2.8}$$

where v is the relative speed of the star, $\Delta\lambda$ is the shift between the expected and the observed wavelength and i equals the inclination of the system. The light can be either blue- or red-shifted, depending on the direction of the movement.
In a majority of cases only one of the stars can be seen in the spectra. The companion is usually to faint. However, bright companions may be present by a second system of spectral lines. In this case, the system would be classified as double lined and one system of lines would be blue-shifted while the other one suffers from a red-shift and vive versa after half an orbital period.

---

[1] http://csep10.phys.utk.edu/astr162/lect/binaries/astrometric.html

2.1.4. Eclipsing binaries

A special case of spectroscopic binaries are eclipsing binaries. In these systems, the orbital plane lies in, or very close to, the line of sight of the observer. This leads to eclipses when one component occults the other one. They can either be total (if one star covers the other one completely) or grazing, when the coverage is only partial. Of course there are several subtypes of eclipsing binaries, which will be explained in the following.

When it comes to classification of eclipsing systems, there are two different approaches. One focuses on the shape of the system, the other one describes the systems by the differences in their lightcurves.

The **morphological classification** is based on the Roche model. It divides between *detached* systems, where no component of the double star system fills its Roche lobe (Figure 2.4c), *semidetached* systems, where only one component fills its Roche lobe completely (Figure 2.4d) and *contact* systems (Figure 2.4b). In the last case both stars fill their Roche lobes and matter can be transferred via the inner Lagrangian point. If they even overfill the Roche lobe, an *overcontact* system is formed (Figure 2.4a). The stars in overcontact systems share a common envelope which also allows mass to be transferred between the components.
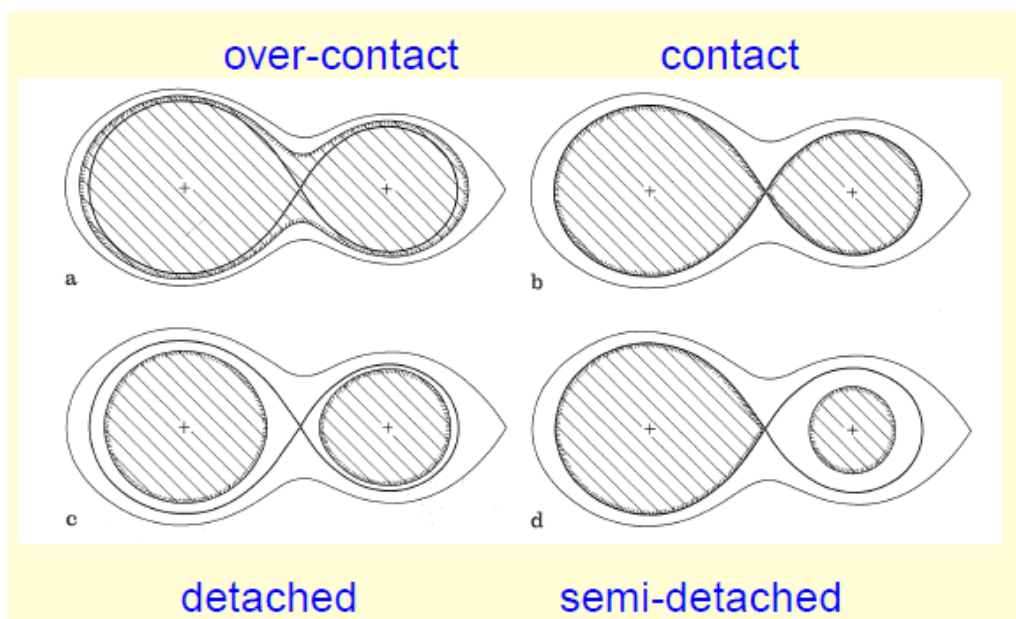
Figure 2.4.: Different systems according to the morphological classification[1]

The **phenomenological classification** is based on the shape of the lightcurve. Depending on parameters like the size of the stars and the separation, the form of the lightcurve differs. It can be distinguished between three basic types, named after the first star that was discovered to have this characteristic form of the lightcurve.

---

[1]`http://www.sternwarte.uni-erlangen.de/~drechsel/vorlesungen/physiksterne/HD/`
   `eclipse/ds-allgemein.pdf`

- β **Lyrae**

  β Lyrae systems show a constant change in luminosity. This is caused by the ellipsoidal deformation of one star. Usually the depth of the eclipses is not equal. One of the components has filled its Roche lobe.
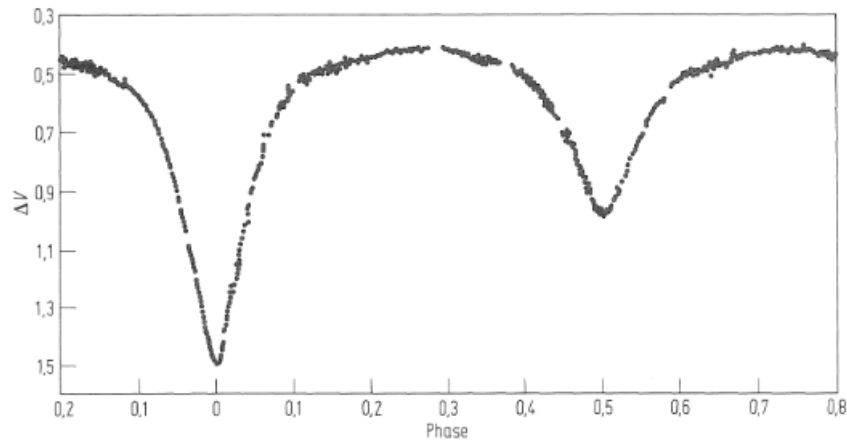
Figure 2.5.: Lightcurve β Lyrae type[1]

- **W UMa**

  In W UMa systems, both stars have filled their Roche lobe and formed an (over-) contact system. Therefore, the luminosity changes constantly, but the the minima show a similar depth.
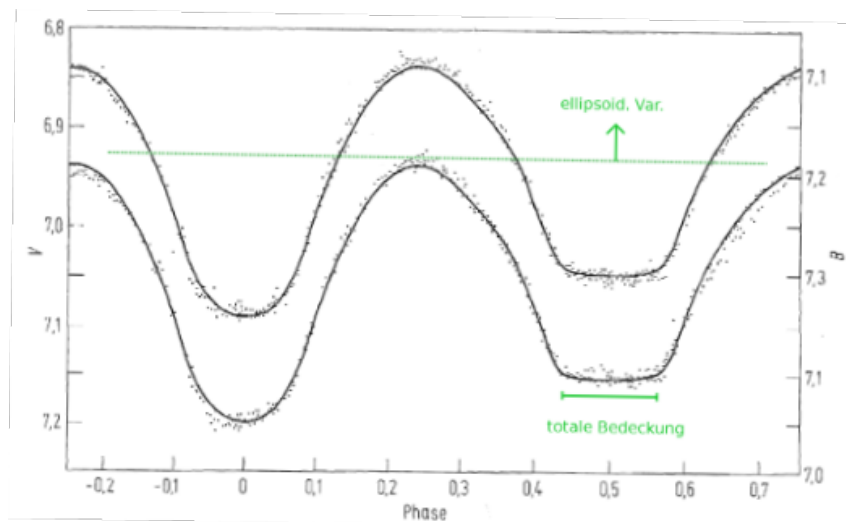
Figure 2.6.: Lightcurve, W UMa type[1]

- **Algol**

  Algol systems consist of separated, detached stars and show an almost constant

---

[1]http://www.sternwarte.uni-erlangen.de/~drechsel/vorlesungen/physiksterne/HD/
  eclipse/ds-lichtkurvenanalyse.pdf

luminosity outside of the minima. As one star is usually much brighter than the other one, the primary- and the secondary minima have different depths. For some systems a reflection effect (see Section 2.2.2) can be observed.
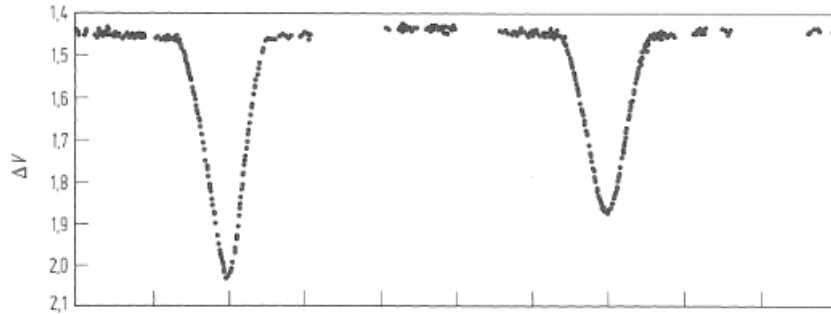
Figure 2.7.: Lightcurve Algol type[1]

2.2. Analysis of binary systems

To gain all possible parameters of a binary system, one has to perform three different types of analysis. Only the combination of spectroscopic-, photometric analysis and the identification of the proper motions of a system makes it possible to understand such a system in detail. In the following sections all three methods and the programs needed are described.

2.2.1. Spectroscopic Analysis

Usually the first step in the analysis of stars is looking at the spectra. They can tell a lot about the properties of the star. The radial velocity, the effective temperature, chemical abundances and the surface gravity can be derived from a quantitative spectral analysis using model atmospheres. The properties are calculated from the shape and the position of several spectral lines.

- The **radial velocity** is calculated from the position of a spectral line in comparison with the position measured in the laboratory.

- The **absolute temperature** can be estimated by measuring the depth and shape of a line with respect to the continuum and other lines of the same chemical elements.

- The helium abundance **log y** is linked to the commonness of helium related lines.

- The surface gravity **log g** can be calculated from the flanks of the Balmer lines. These lines are sensitive to pressure broadening by the Stark effect.

By calculating the radial velocity from several spectra and plotting it against the time of observations, a radial-velocity-curve is generated. If the orbit of the binary is circular, the form of the radial-velocity curve is sinusoidal. The semi-amplitude

is called K. One has to remember that the velocity of the system cannot be determined by the radial velocity curve only. From the extrema of the RV curve and the inclination of the system, the true velocity can be calculated.

$$v_0 = \frac{v}{\sin i} \tag{2.9}$$

If the inclination is unknown, the measured radial velocity can be seen as a lower limit.

Another important information that can be extracted from a spectroscopic analysis is the total mass of a system or at least the mass ratio of the components.

By combining the mass function (for the single-lined case)

$$f(M_1, M_2) = \frac{M_2^3 \sin(i)^3}{(M_1 + M_2)^2} = \frac{K_1^3 P}{2\pi G} \tag{2.10}$$

with an expression for the mass ratio

$$q = \frac{M_2}{M_1} = \frac{K_1}{K_2} \tag{2.11}$$

a function for the mass with dependence for the inclination is generated.

$$M_j \sin(i)^3 = \frac{P}{2\pi G} \frac{K_j^3 (q + 1)^3}{q^3} \tag{2.12}$$

Often, the mass of the primary can be roughly estimated from its effective temperature and surface gravity. Using this estimation offers a possibility to find a lower limit to the mass.

The analysis of spectra was done by using the program SPAS, the *Spectra Plotting and analysis suite* by Heiko Hirsch [Hirsch, 2009]. It is a reimplementation of Ralf Napiwotzki's *FITSB2*, upgraded with a graphical user interface and some other features. The program fits synthetic spectra to the observed data. The user can select certain lines and change the width used for the fit. The fitting is done via a downhill simplex algorithm, the synthetic spectra are calculated from grids of LTE model atmospheres including metal line blanketing [Heber et al., 2000], the errors are calculated with the Bootstrapping algorithm.

At first, no model atmospheres are used. In this step only the shift between the observed position of the line and the expected position is calculated by fitting a combination of Gaussians and Lorentzians to the line profiles. The user can select the lines with the best signal to noise ratio and exclude those that are not visible. Afterwards the model atmospheres are taken into account to calculate the effective temperature, gravity and helium abundance. This can be done for each spectrum separately or after coadding them to improve the S/N ratio and therefore the visibility of the lines. In Figure 2.8, a screenshot of *SPAS* output showing fits to several Balmer lines is displayed.
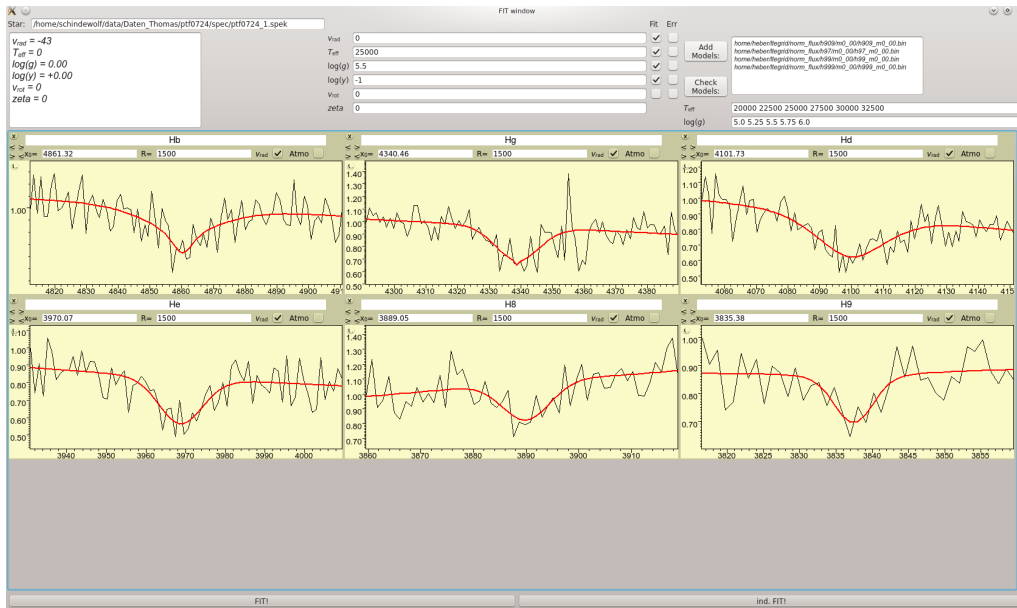
Figure 2.8.: Screenshot of SPAS output, showing fits to several Balmer lines of a faint sdB star

2.2.2. Lightcurve analysis

To perform an analysis of a lightcurve and extract stellar parameters from it, the star system has to be described via theoretical models that allow calculating the observed flux in a certain direction. From these models a synthetic lightcurve can be calculated and compared to the observational data. By varying a number of parameters in the theoretical models, different lightcurves can be produced, each fitting the observations to a certain degree.

A common approach to model light variations in binaries was presented by Wilson and Devinney [1971]. For every orbital phase the monochromatic radiation flux towards an observer is calculated. The geometry of the system is based on the Roche model. In this process several effects have to be taken into account.

- **Reflection effect**
  In a binary system, both stars irradiate each other and heat up the photosphere of the other component. As a higher temperature results in a higher brightness, an increased flux can be detected from an irradiated stellar atmosphere. To describe the percentage of the reflected light, the Albedo A can be used. Its value can exceed unity due to atmospheric interaction and reprocessing of radiation. The increase of the temperature due to the reflection can be described using

$$T_R = T_2 \cdot \left(1 + \frac{A_2 F_1}{F_2}\right)^{\frac{1}{4}} \tag{2.13}$$

  with $F_{1,2}$ the flux emitted by the primary and the secondary [Schaffenroth, 2010]. In the Wilson-Devinney approach the reflection effect is taken into

account by the reflection coefficient R,

$$R = \frac{I_{\text{ref}}}{I_{\text{noref}}} = \frac{e^{\frac{\hbar c}{\lambda k T_2}} - 1}{e^{\frac{\hbar c}{\lambda k T_R} - 1}} \tag{2.14}$$

which corresponds to the ratio of reflected and not-reflected intensity.

- **Limb darkening**
  Limb darkening is the gradual decrease in brightness of a star's disk. As the atmosphere's temperature increases with depth, more light is emitted from deeper and therefore warmer layers. If the limb of a star is observed, only the upper and cooler layers can be observed, as the angle under which we look at the atmosphere becomes flatter. A linear limb-darkening coefficient is adopted in the Wilson-Devinney model:

$$D = \frac{I(\gamma)}{I(\gamma = 0)} = 1 - x + x \cos \gamma \tag{2.15}$$

with γ, the angle between the line of sight and the normal to the surface of the star [Schaffenroth, 2010].

- **Gravitational darkening**
  The gravitational darkening is based on the rotation of a star. If the rotation is fast enough, the shape of the star is changed in an oblate way. Therefore, it has a larger radius at the equator, resulting in a lower surface gravity, surface temperature and brightness. Hence the star appears brighter at the rotation poles than at the equator.
  The change in flux can be calculated via

$$F_l = F_p \left(\frac{g_l}{g_p} \right)^g \tag{2.16}$$

with g the gravity acceleration and the index l for the equatorial value and index p for the polar one [Schaffenroth, 2010].
Depending on the mass of the star, more precisely its type of envelope, the value for the exponent g changes. If the envelope is fully convective g is ≈ 0.32 [Lucy, 1967]. If the envelope is fully radiative, g is in accordance with 1.0 [von Zeipel, 1924]. The gravitational darkening factor can be written as

$$G = \frac{I_{\text{local}}}{I_{\text{pol}}} = \frac{e^{\frac{\hbar c}{\lambda k T_p}} - 1}{e^{\frac{\hbar c}{\lambda k T_l} - 1}} \tag{2.17}$$

Each star is divided into small areas. To calculate the total flux, the flux from all sectors visible to an observer are added. According to Schaffenroth [2010], the flux from a single sector can be described as

$$l(\theta) = r^2 \sin \theta \Delta \theta \Delta \phi \frac{\cos \gamma}{\cos \beta} GDRI \tag{2.18}$$

The angles are explained in Figure 2.9.

12
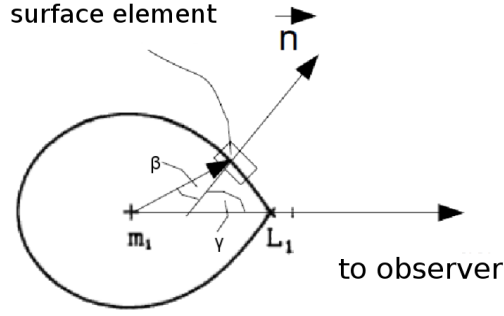
Figure 2.9.: sketch for calculation the radiative flux, taken from [Schaffenroth, 2010]

To perform the analysis of lightcurves in this thesis, the program MORO (MOdified ROche model) was used [Drechsel et al., 1995]. The program is based on the Wilson-Devinney approach, but uses a modified Roche model that takes the radiative pressure of the stars into account. Basically Wilson-Devinney mode 2 has been used. It is suitable for detached and semi-detached systems and couples the luminosity of the secondary L_2 to its effective temperature T_2. No other constraints are set up. The optimisation of parameters is achieved by χ^2-minimisation and the simplex algorithm [Kallrath and Linnell, 1987].

By starting with m different parameters, m+1 different sets of these parameters are generated around the values of the parameters, specified by the user. These sets are called the simplex. For every single subset of the simplex, a synthetic light curve and its standard deviation $\sigma_{\text{fit}}(x)$ are calculated.

$$\sigma_{\text{fit}}(x) = \sqrt{\frac{n}{n-m} \frac{1}{\sum_{\nu=1}^{n}} \sum_{\nu=1}^{n} \omega_\nu d_\nu^2(x)} \qquad (2.19)$$

d_ν are the residuals, the difference between observational data and the calculated model and ω_ν is a weight that can be used to increasingly emphasize the most important data points, e.g. the bottom of the primary eclipse [Schaffenroth, 2010]. The parameter set with the worst σ_{fit} is deleted and a new set is created automatically. Therefore a minimum is always reached. But it cannot be ensured that the reached minimum is corresponding to the global one. It is more likely to be one of the local minima, distributed in the simplex. This disadvantage is enforced by the large number of free parameters and their correlation to each other.

For a single light curve 17 parameters have to be adjusted. They are shown in Table 2.1. Especially the mass ratio, one of the most important solution parameters, is strongly correlated with other parameters and causes a degeneracy of solutions. Therefore, in a first step, the mass ratio is fixed while the other parameters are adjusted. Thereafter, the mass ratio was changed by a certain increment and the iterative process started again. Some of the parameters, e.g. T_2, q or $x_{1,2}$, can be constrained from spectroscopic observations or tables (e.g. the coefficients for gravitational darkening). Too many free parameters tend to generate under-determined solutions with no guarantee of uniqueness. To select a specific solution, the σ_{fit} of all solutions have to be compared. The solution with the smallest value is most likely the best one. However, it has to be checked if the calculated parameters are

parameter	description
i	inclination
q	mass ratio
g_1, g_2	coefficients for gravitational darkening
T_1, T_2	effective temperatures
A_1, A_2	Albedos
Ω_1, Ω_2	surface potentials
δ_1, δ_2	radiation pressure parameters
$L_1(\lambda), L_2(\lambda)$	luminosities
$x_1(\lambda), x_2(\lambda)$	coefficients for limb darkening
l_3	third light

Table 2.1.: parameters used for calculation of artificial light curves

physically reasonable. Especially too high radiation pressure parameters occurred very often and were an indicator for rejecting a specific solution.

2.2.3. Proper motions & kinematics

To study the motion of the stars in the Galaxy, we need to know their present position (α, δ), distance and the radial- and transversal velocity components. The later is the most difficult to determine as it is based on the distance and the proper motion of the star itself.

By knowing the proper motion and the position of a star, it is possible to calculate its track and gain information about its origin and the way it will take through the galaxy.

To calculate the proper motion of a star, its position is measured with respect to a reference background. As the movement is usually very small, a long time base covering several decades is desirable. In former times, pictures of stars have not been made with CCD cameras but with a photographic emulsion placed on glass plates. These plates have been digitised so that the examination is possible with modern, computer based approaches.

The reference background is made up by small galaxies. Their distance is so large that small movements are unimportant and can be neglected. Their position on the photographic plate is determined by fitting 2-dimensional Gaussians to the center of the brightness distribution. The position of the target star is measured with the same method. This leads to a lot of coordinates for every single plate. Of course the same objects have to be selected on every plate available. By comparing the position of the object on all the plates with the reference background, moving objects can be identified.

It is often desirable to know the motion of an object with respect to the Galactic plane. To derive the orbital tracks of an object and get an estimation of the errors of the Galactic velocities, Monte-Carlo simulations can be performed. The orbital tracks show the path of an object in the Galactic gravitational potential. To compare the object to a sample of other stars, it can be helpful to calculate the Galactic radial-velocity U and the Galactic rotational velocity V.

Another approach to calculate the proper motion of an object and an application of

the Galactic velocities is presented in Chapter G in the appendix.

2.3. Subdwarf B Stars

(If not marked otherwise, all information in this section are taken from Heber [2009].)
In this section detailed information about subdwarf B stars (sdBs hereafter) are
given. After describing their properties, several possible formation channels are
discussed, followed by a brief review of sdBs in binary systems

2.3.1. Properties

Subdwarf B stars were discovered in the 1950s. They are core helium-burning stars
with very thin hydrogen envelopes. The envelope mass is about $M_e < 0.02\,M_\odot$.
Therefore no H-burning takes place.
These stars dominate the population of faint, blue stars at high galactic latitudes
and can be found in the old disk and the halo [Ferraro et al., 1997].
They have a high surface temperature between 20000 and 40000 K and a surface
gravity of $\log g = 5.0 \simeq 6.0$. The high temperature leads to an increased emission of
UV radiation, which makes them a good candidate for the UV-Upturn phenomenon
in elliptical galaxies. These galaxies were thought to consist mainly of old, red stars,
but show a contradictingly high radiation in the UV regime [Brown, 1997]. Subdwarf
B stars are located on the Extreme Horizontal Branch (EHB) in the Hertzsprung-
Russel-Diagram as it can be seen in Figure 2.10. The EHB is the blue end of the
Horizontal Branch where the luminosity produced by H-shell burning is negligible.
At the end of their life on the EHB they evolve directly to White Dwarfs because
they do not have enough hydrogen in their shells to sustain H-burning.
If the mass of an sdB star is too small to ignite core He-burning, it is called a post-
RGB star.
By inspecting their spectra, it can be recognized that He I lines are comparatively
weak, due to helium diffusion. In addition, the Balmer lines, although clearly visible,
are unusually broadened. This is caused by the high surface gravity.
Figure 2.11 shows the mass distribution of several known sdB systems. It can be seen
that masses of $0.47\,M_\odot$, the so called canonical mass, are most frequent. However,
stars with both, much lower and much higher masses have been found, too.

2.3.2. Possibilities of formation

The formation process of sdB stars is still a topic of today's research. It is not fully
understood how a star could lose almost its entire envelope while still being able to
ignite helium in the remaining core. However, several possible formation channels
have been discovered throughout the years. It turned out, that mass loss or -transfer
in close binaries is an important option. The most prominent ones are explained
hereafter.

2.3.2.1. Roche Lobe Overflow channel

In this channel, the sdB stars are formed in binaries with long periods (10 to
500 days). Unlike in the Common-Envelope channel, the mass transfer from a red
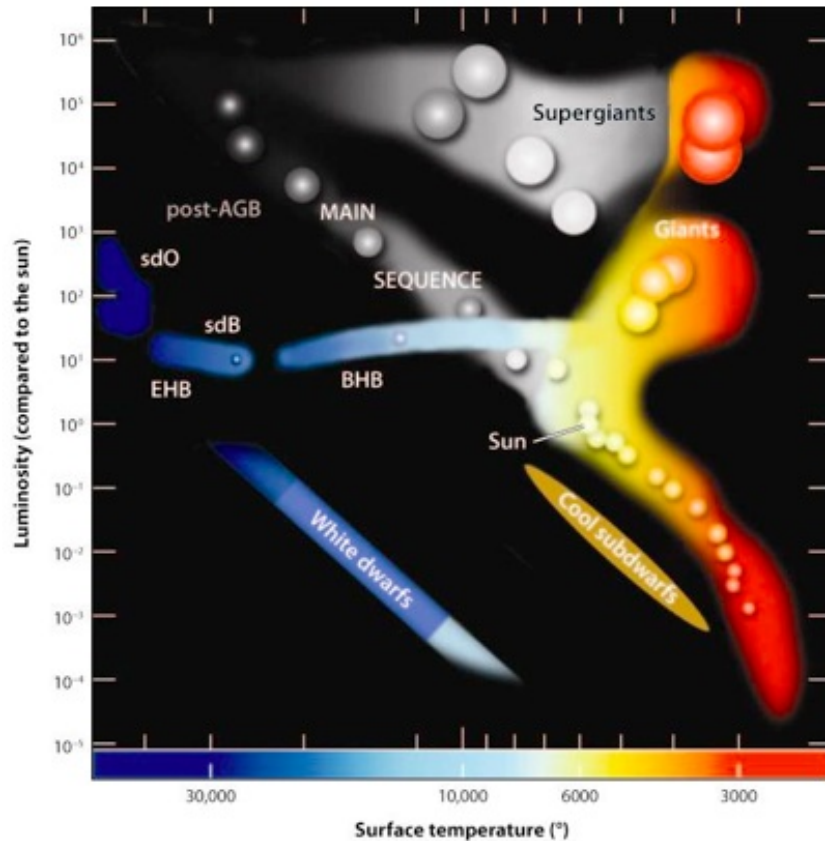
Figure 2.10.: Hertzsprung-Russell diagram[1]

giant to the secondary main sequence star is stable. Therefore no common envelope is formed. This requires an initial mass ratio smaller than 1.2 to 1.5, according to model calculations. The giant loses most of its envelope, but the mass transfer stops when the hydrogen-rich envelope is sufficiently reduced and the star no longer fills its Roche lobe. Afterwards, the radius of the star decreases and a helium flash is possible (depending on the mass of the remaining, degenerate He-core).

2.3.2.2. Common-Envelope Ejection channel

In the common envelope ejection (CEE) channel, a star during its red giant phase in a binary system fills its Roche lobe and mass is transferred to the secondary star dynamically at such a high rate that the secondary cannot accrete the matter. The mass ratio of the two stars is approximately 1.2 to 1.5. Otherwise the mass transfer could be stable and it would be more likely that the evolution of the systems follows the RLOF channel.

At some point, the Roche lobe of the secondary is overfilled. This leads to the formation of a common envelope around both stars. Due to friction in the envelope,

---

[1]http://physics.highpoint.edu/~bbarlow/subdwarfs.html
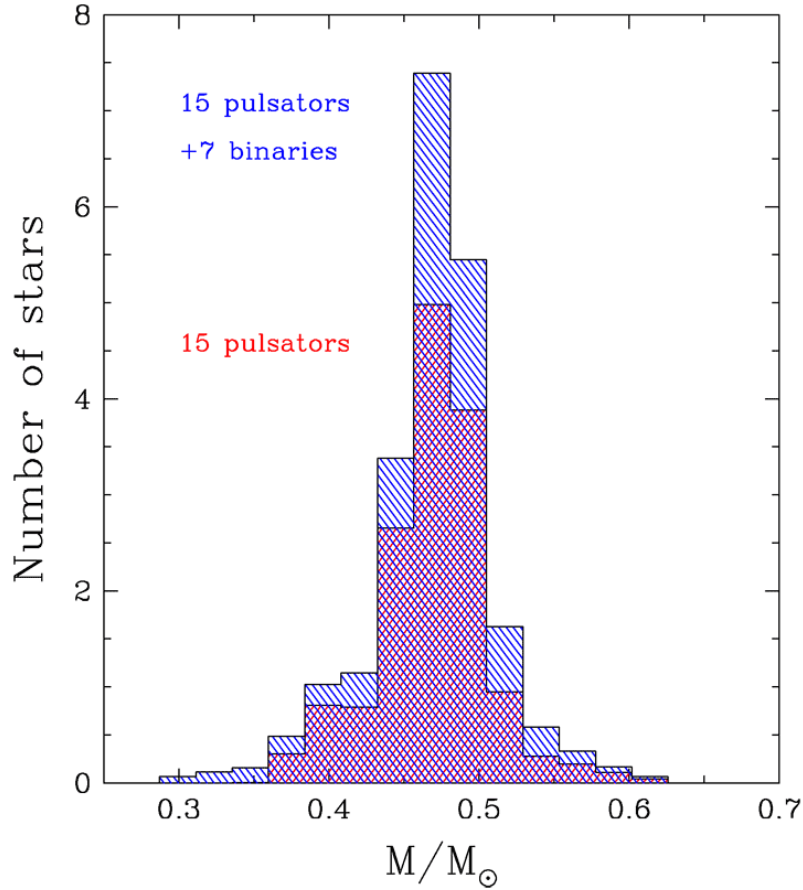
Figure 2.11.: Mass distribution of sdB stars[1]

both stars approach each other. This leads to a release of orbital energy that is used to eject the envelope when its binding energy is exceeded.

The resulting binary system consists of the core of the former red giant and the main sequence companion. Those systems have periods between 0.1 and 10 days.

2.3.2.3. Double He-core White Dwarf merger channel

The merger channel can explain the existence of single sdBs. It assumes a binary system with two He-core white dwarfs on shrinking orbits. The separation becomes smaller due to the loss of energy by the emission of gravitational waves [Webbink, 1984]. If the white dwarfs are close enough, the less massive object will get disrupted and be accreted by the more massive white dwarf. As a result He burning could start. That would lead to a sdB star with a thin hydrogen envelope that follows a wide mass distribution.

The problem with this scenario is the spin-up of the remnant sdB star, which therefore should rotate very quickly. This, however is not observed.

---

[1][Fontaine et al., 2012]

2.3.2.4. Mass loss triggered by stellar winds

Another possibility to produce a single sdB was first discussed by D'Cruz et al. [1996]. He showed that a star on the Red Giant Branch could lose its envelope due to strong stellar winds. As soon as helium is ignited in the core, the star should evolve to an sdB.

On the other hand it is very unlikely that the required mass loss is only caused by the stellar winds. This would require fine tuned parameters and could not explain all the single sdB stars found so far.

2.3.3. Subdwarf B stars in binaries

With regard to the formation processes, it is very likely to find an sdB in a close binary system. The chances of finding an eclipsing system grow with closer systems. Therefore binaries containing an sdB play an important role. As already mentioned beforehand, eclipsing systems allow the determination of the mass and radius of their components. About 50% of the known sdBs reside in close binary systems with periods less than 30 days [Maxted et al., 2001]. An overview provided by Ritter and Kolb [2003] containing 81 sdB binaries is shown in Figure 2.13. Most of the systems have periods shorter than 0.1 days.
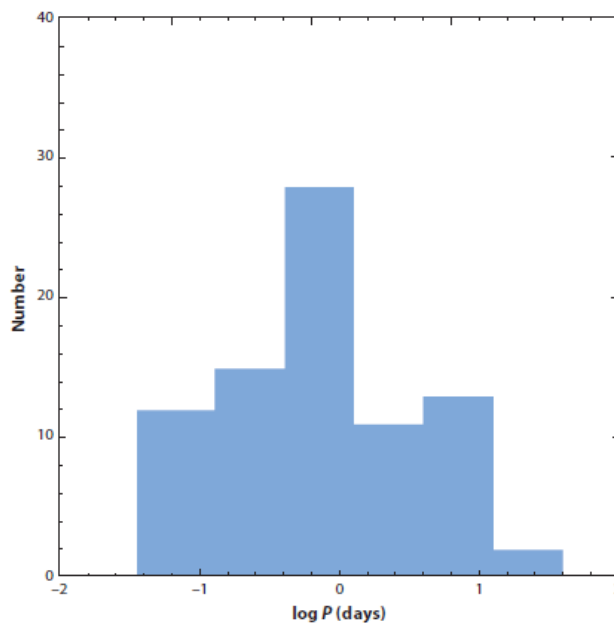
Figure 2.12.: Period distribution of sdB stars[1]

A special and very interesting type of sdB binaries are HW Vir systems. Those eclipsing systems contain an sdB and a late M dwarf. SdBs and M dwarfs have roughly the same size. This circumstance allows the formation of very close systems with results in very short periods. The period is roughly ~ 0.1 days. They were first discovered in 1986 and are named after the prototype, HW Virginis. The short

---

[1][Ritter and Kolb, 2003]

period of these systems indicate that they originate from a common envelope phase. Up to now, only fourteen such systems are known.

The M dwarf is usually not visible in the spectra (single-lined) and can only be detected by the reflection effect (see Section 2.2.2). Therefore HW Vir systems usually have a very characteristic lightcurve. Despite the M dwarfs, other companions like brown dwarfs have been discovered.

In some of the systems, such as NY Vir, the sdB was found to be pulsating with
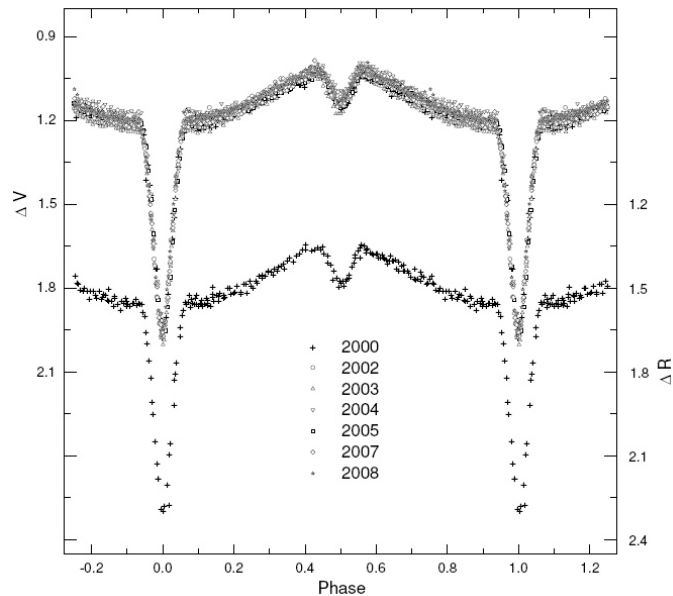
Figure 2.13.: Lightcurve of HW Vir[1]

a period of a few minutes (see Section 4.3.3.2, caused by an iron opacity bump in sub-photospheric layers [Kilkenny et al., 1997]. This offers promising opportunities for astroseismology.

Another important and interesting aspect about HW Vir systems is the existence of low mass „third bodies" like giant planets or brown dwarfs. They neither contribute to the spectra nor to the light curve. This subject will be discussed in the following section.

2.4. Search for exoplanets and unseen companions

The first exoplanets orbiting a star were discovered in 1995 [Mayor and Queloz, 1995]. In 2004 the first planet in an orbit around a brown dwarfs was imaged directly with an optical telescope [Chauvin et al., 2004]. Up to now, roughly 1800 exoplanets have been discovered, several thousand candidates are still waiting for confirmation.

Although living on a planet orbiting a single star, planets in binary systems are likely to provide the majority, and planetary formation in these systems became a more and more important issue in research. Binary planets can be divided in S- and P-types. S type planets orbit only one component of the binary and their period is much

---

[1]http://www.astro.cz/clanek/3478

smaller than the binary period. P type planets on the other hand are circumbinary, meaning that they orbit around the center of mass of both components. Their period exceeds the binary period. The P type planets are supposed to survive longer than S-type ones [Muterspaugh et al., 2007].

Third bodies in binary systems can be discovered in various ways. The three most common ones are explained afterwards. But only the eclipse timing method will be explained in detail, as it can be used with the telescopes in Bamberg.

2.4.1. RV variations

In binary systems two components are in an orbit around the common center of mass. This leads to periodic changes in the observed radial velocity (RV) of one or both components. Third bodies, like planets, also cause variations in the observed radial velocity because of their long periods and low masses. However, these changes usually lie in the regime of a few $\frac{m}{s}$ (depending on the mass of the planet) and therefore are only minor compared to the changes in RV caused by the orbiting stars.

It is very difficult to exclude all effects on the RV curve that are not produced by a third body. This method can usually only be applied to very good data with a high S/N ration obtained with high resolution.

If the system is a close binary, the tidal spin-up of the components worsens the situation as the projected rotational velocity may exceed about $100\frac{km}{s}$ and therefore compromises the precision of a RV measurement.

Although the Remeis Observatory is equipped with a BACHES Spectrograph [1], the RV accuracy obtained in combination with the EHT is not good enough to legitimate a deeper research activity with this method.

2.4.2. Direct eclipses

Regarding the number of detected (and confirmed) exoplanets, the second approach seems to be much more promising.

It is based on photometric observations of a target to find the eclipse of the planet in front of its host star. These observations can be conducted by ground-based telescopes like SuperWASP or by satellite missions like Kepler or COROT.

Wether a transit can be detected or not depends on the inclination of the system. Furthermore it is necessary to observe a system for a longer period of time as the period of circulation for exoplanets usually lies in the magnitude of years. The effect on the measured change in brightness of the system is commonly very small (milli-mag) and therefore requires high photometric accuracy.

Although the accuracy could be achieved with the telescopes in Bamberg (at least for giant gas planets , the very time consuming observations without a guarantee of finding an object make this approach less interesting.

2.4.3. Eclipse timing/LITE

The most promising method to be used with the EHT is the eclipse timing method (or light time travel effect - LITE).

---

[1] http://www.baader-planetarium.de/news/baches/baches.htm

Circumbinary companions can cause timing variations of the eclipse in the double star system, due to the finite speed of light and the reflex motion of the binary around the centre of mass. It is based on the periodicity of eclipses. If there is no third body, the time between two primary eclipses would be exactly one period. A third mass would move the center of mass over a long period of time which results in little aperiodic trends, meaning that the time difference between two repeating features of the lightcurve is no longer exactly one period. This effect can even be observed if the inclination of the system does not allow a direct observation of planetary eclipses. Other period-changing events, like the emission of gravitational waves distort the period on a much longer timescale..

From the O-C (observed - calculated) curve parameters like the mass of the third body can be roughly estimated. The LITE effect is visible as periodic sinusoidal variations in the graph. Some other effects can be seen as well. A magnetic interaction between the stars in the system would shorten the period and would cause a parabolic variation [Schaffenroth, 2010].

Pribulla et al. [2012] showed that the amplitude of the observed LITE increases with the orbital period P_3 of the substellar companion and its mass M_3:

$$\Delta T = \frac{2M_3 G^{1/3}}{c} \left(\frac{P_3}{2\pi(M_1 + M_2)} \right)^{2/3} \tag{2.20}$$

If a timing precision of about $\pm 10\,s$ can be achieved, it should be possible to detect planets with around $\sim 10\,M_{jup}$ in orbits of 10 to 20 years [Ribas, 2006].

According to Pribulla et al. [2012] the timing precision depends on several parameters, like the duration of the eclipse D, the depth in magnitudes d and the number of datapoints during the eclipse N.

$$\Delta t = \frac{D\sigma}{2d\sqrt{N}} \tag{2.21}$$

σ is the brightness uncertainty for a single measurement. Of course the diameter of the telescope and the exposure time play an important role in determining the expected precision of minima. By neglecting the read-out noise of a camera the uncertainty of a single data point σ can be described via

$$\sigma \sim \frac{1}{\sqrt{\pi \left(\frac{A}{2} \right)^2 E}} \tag{2.22}$$

using the exposure time E and the aperture of the telescope A [Pribulla et al., 2012]. To be able to compare the data from different observers and different epochs it is necessary to convert the observation time to the so called TCB, the Barycentric Coordinate Time. The common Julian Date (JD) is transformed to the TCB by adding or subtracting a certain factor which can be calculated by various programs. This factor is dependent on the time of the observations, the coordinates of the observed object and the geographic coordinates of the observing site. The TCB compensates the variations of timings that are due to the movement of the Earth (and the observer) around the common center of mass in the solar system.

However it is very important to make new observations, even if a system seems

already solved. The binary HW Vir has been observed for several decades now. It soon became clear that a third body has to be involved in the system, as variations were detected with O-C diagrams. The monitoring of this system and the resulting large database allowed to set up models for the third body. Up to 2010 the model suggested by Lee et al. [2009] seemed to describe the system and the variations correctly. But the latest observations of HW Vir revealed that the period variations have undergone an unpredicted development. Figure 2.14 shows the visualization of a new O-C model for HW Vir, presented by Beuermann et al. [2012b]. It can be seen that the former model, presented by Lee et al., was not able to predict the latest trend in the dataset. Therefore it is necessary to observe as many eclipsing
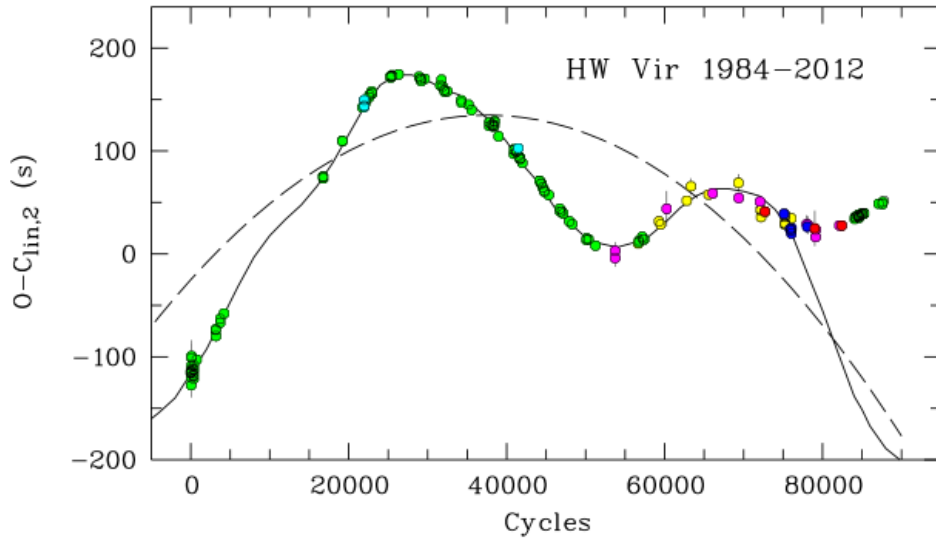
Figure 2.14.: O-C residuals of the mid-eclipse times from the linear ephemeris used by Lee et al. (2009) along with their model curves for the two-companion model (solid) and the underlying quadratic ephemeris (dashed), taken from Beuermann et al. [2012b]

binary systems as possible, even if they already seem to be correctly described by any models.

The LITE observations with the EHT and data reduction performed afterwards are described in Chapter 4.

3. Technical Equipment

Before August 2013 the observational equipment of the Karl Remeis Observatory mainly consisted of two telescopes. The first one is a 40 cm *Meade ACF*[1] telescope on an *AstroPhysics 1200 GTO*[2] mount in the West-Dome and the second one was a 60 cm Cassegrain telescope in the East-Dome. Both, telescope and mount, were manufactured by *Zeiss*[3].

They were mainly used for the education of lab-students and for taking „pretty pictures“. Scientific research has not been done since the early 60's due to the increasing light pollution and the unsuficient technical facilities. In particular the 60 cm telescope suffers from a slow aperture (40 cm: f/10, 60 cm: f/18) and an old mount that leads to a limitation of the exposure time, as well as difficult, time consuming handling and guiding . In combination with the slow aperture, the break-even-magnitude was too high for serious research. The opportunity of guiding the mounts was available, but the error-proneness made it unattractive for use.

From 2005 to 2013 German universities were allowed to impose enrollment fees. Those were designated to improve the condition of studies and the accouterments of the single institutes. As a result the Remeis Observatory purchased a new telescope, mount and camera to replace the old instrumentation in the East-Dome.

The following sections give an overview of the new hardware and their technical specifications.

3.1. Planewave CDK 20”

3.1.1. Optical layout

The new telescope is a „Corrected Dall Kirkham“ type (CDK), manufactured by *Planewave*[4]. These telescopes have an elliptical main mirror and a spherical secondary mirror. It has a diameter of 51 cm and focal length of 3454 mm. This results in an aperture ratio of f/6.8[5], which is quite fast for a telescope of that size. An additional pair of lenses is placed inside the ocular extension to provide a flat visual field without any aberrations and a diameter of 52 mm. The optical layout of the telescope can be seen in Figure 3.1. Furthermore, the new telescope is equipped with an electrical motor focus, which will be explained later on.

The telescope has been officially named Ernst-Hartwig-Telescope (EHT), after the first director of Remeis Observatory.

Since February 2014 a guiding scope has been attached to the tube. This 115 mm APO-refractor can be used for guiding purposes or for capturing large-field-images.

---

[1] http://www.bresser.de/ACF/

[2] http://www.astro-physics.com/index.htm?products/mounts/1200gto/1200gto

[3] www.zeiss.de

[4] www.planewave.com

[5] www.baader-planetarium.de/planewave/planewave_htm/cdk-20.htm
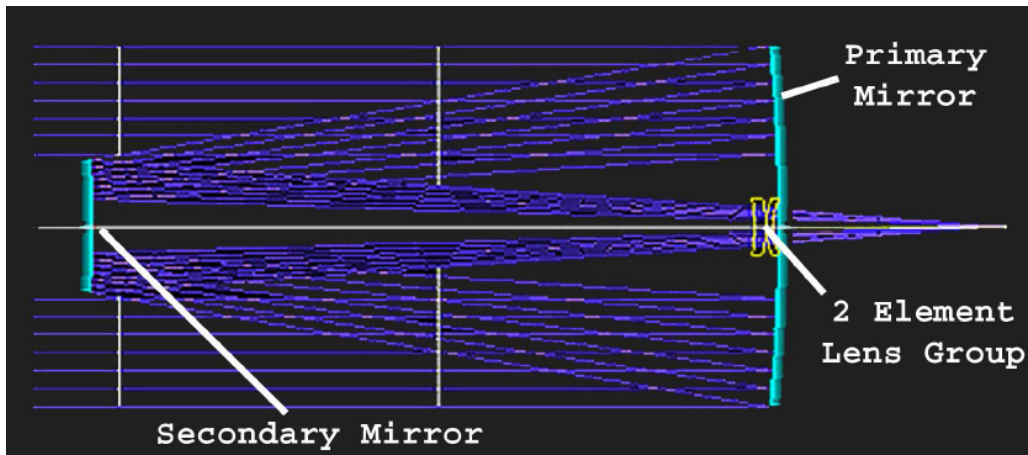
Figure 3.1.: Optical layout of a CDK-telescope[1]

3.1.2. Optical adjustments

Before the telescope could be used for scientific purposes a few adjustments had to be made so that it could develop its best, optical performance. In detail this meant centering the secondary mirror and optimizing the distance between the main- and the secondary mirror.

- **Centering**
  The secondary mirror is tiltably mounted with three spring-supported screws. By turning one of these screws, the mirror can be tilted. The mirror has to be adjusted to reflect the light exactly back into the center of the main mirror. Otherwise, images of stars would no longer be point like but elongated in one direction.
  To achieve the best-possible result, a webcam was attached to the eye piece extension and a video of a bright star was captured. The telescope was defocussed until the shadow of the secondary mirror was visible in the star disk. Afterwards the shadow was centered by loosening and tightening the screws mentioned above.
  Figure 3.2 shows a composite of 40 single frames that were taken after finishing the alignment. The flat spot at eight o'clock in the image is due to a screw of the extension tube used at this setting, that extended a little bit into the optical path.

- **Distance between mirrors**
  The distance between the main- and the secondary mirror is crucial to get the best possible optical results.
  As the main mirror is fixed inside the tube and cannot be moved, again the secondary mirror has to be adjusted. Changing the distance is possible without adulterating the centering.
  To determine the correct distance a Ronchi-Ocular was used. If the distance is not correct, bright light sources (stars) show characteristic stripes. These stripes disappear when approaching the correct distance between the mirrors.

---

[1] http://www.baader-planetarium.de/planewave/planewave_htm/cdk-opt-design.htm
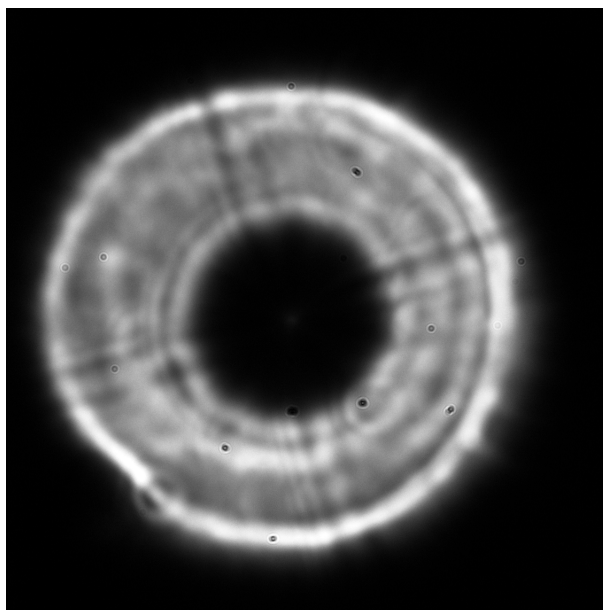
Figure 3.2.: Final result after centering

Because of the structural features of the eye-piece, it was not possible to attach a camera. But Figure 3.3 shows a computer simulation of the view through the ocular. If the interspace between the mirrors is correct, no stripes should be visible (left image).

Now the optical adjustment was finished. It should be checked (and improved when indicated) on a regular basis because temperature fluctuations or vibrations could cause an aggravation.

3.1.3. Motor focus

As mentioned above, the telescope features an electronic motorfocus. By attaching it to a computer it is capable of compensating the focus drift caused by changes in the main mirror's temperature. To make use of this feature, it has to be determined how much the focuspoint moves if the temperature changes by a certain value.
The temperature can be measured with a sensor attached to the back of the main mirror. The focus point was determined with a *Baader* clear filter, (or an IDAS filter, depending on the target for the night's observation) and a Bathinov mask. Figure A in the Appendix shows the typical pattern that indicates a correct focus. Figure 3.4 represents the data points gained in different nights. It can be seen that the focus tends to move inwards (closer to the backplate of the telescope) as the temperature drops.
For the clear filter the fit-equation

$$f(T) = (0.02927 \pm 0.01523)\,\frac{\mathrm{mm}}{1°} \cdot T + 7.585\,\mathrm{mm} \tag{3.1}$$

is found and respectively for the IDAS filter

$$f(T) = (0.04479 \pm 0.08909)\,\frac{\mathrm{mm}}{1°} \cdot T + 7.683\,\mathrm{mm} \tag{3.2}$$
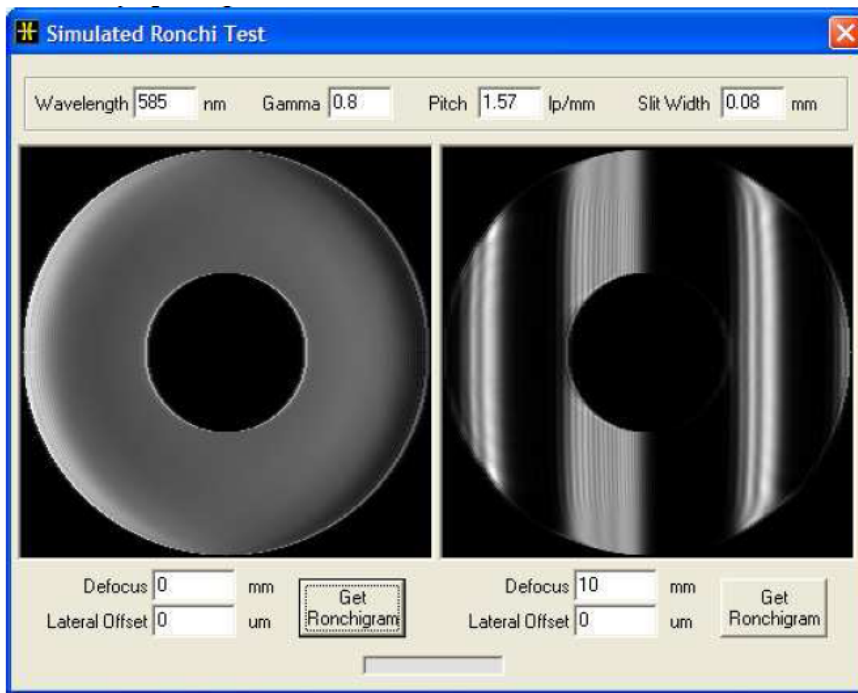
Figure 3.3.: Simulation of the pattern, visible while using a ronchi ocular. Left:
correct distance between the mirrors; Right: missalignment of 10 mm[1]
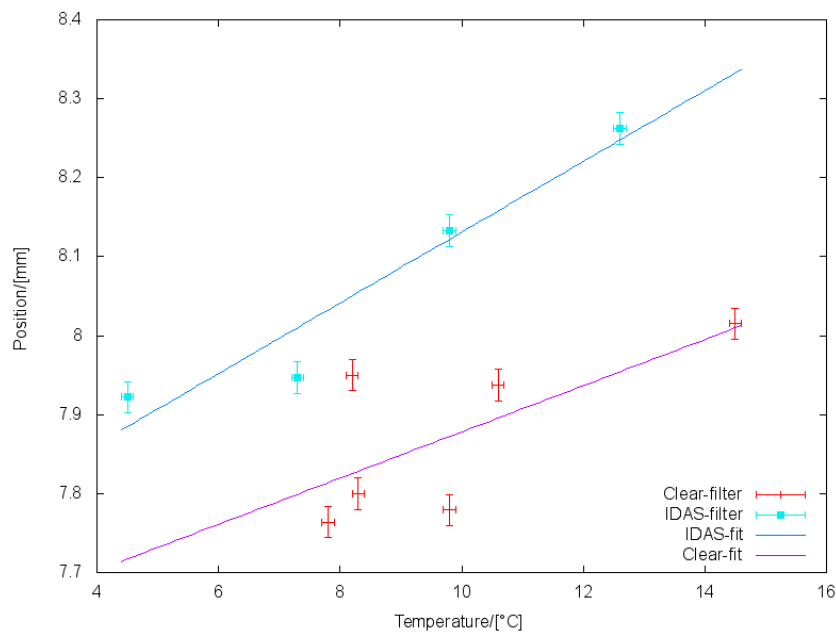
Figure 3.4.: Focusdrift for different filters

However, the results are not reliable. The datapoints show a high scatter caused by
the limited accuracy of the Bathinov mask. Even with the fast aperture of the EHT
the correct position of the focus can only be determined to within about 0.02 mm.
This is caused by the seeing that leads to a fluctuation of the diffraction pattern of

---

[1][Baader-Planetarium]

the mask and leaves room for interpretation as to which position results in the best focus.

Furthermore, the direction of the focus is inconsistent with information from the manufacturer. PlaneWave-Instruments claims that the focus should move outwards as the temperature declines. This is not compatible with the presented results. However, a satisfying explanation has not been found yet.

During the night shifts it turned out that a focus correction is usually not necessary. The focus drifts caused by the temperature are too small to be noticed. If the temperature should drop for 10 or more degrees, it is sufficient to move the focus manually for some μm. But it remains necessary to check the focus when filters are switched.

3.2. 10Micron 4000 HPS Mount

There are basically three types of mounts on the market: The conventional mounts with worm gear drive, the direct-drive mounts and the worm-driven mounts with absolute encoders. Each layout has its advantages and disadvantages. The requirements for the new mount of the observatory are:

- high payload

- high accuracy

- stand-alone capability

Only the worm-driven mount with absolute encoders fulfill all requests. The other concepts were either not precise enough (worm-driven without encoders) or did not offer the stand-alone capability (direct-driven).

In the high-end market for mounts with encoders, capable of being operated with telescopes the size of a CDK 20, there are only very few manufacturers. In the end it was decided to acquire a *GM 4000 HPS (High Precision and Speed)*, produced by *10Micron*[1] in Italy.

3.2.1. Technical data

The GM 4000 HPS is a German equatorial mount with a weight of about 120 kg. The maximal instrument payload capacity ranges from 125 kg to 150 kg, depending if it is used for imaging or just for observing with the naked eye. It reaches a pointing speed up to $5°/s$[1] . The pointing accuracy varies around one arc-minute (according to the manufacturer), while we found an accuracy of about five arc-minutes during nightly use. According to *10Micron* the average (RMS) tracking accuracy is 0.6 arc-seconds. We could verify this value, but only under optimal conditions (see Section 3.2.4 for further information).

3.2.2. Mechanical setup of the mount

The mechanical setup of the mount can be divided into two different control loops, shown in Figure 3.5. The first control loop contains one motor per axis and a

---

[1]www.10micron.com

[1]10micron.de/products/gm-4000-hps-en/gm-4000-hps-goto-mount-1454010/?lang=en
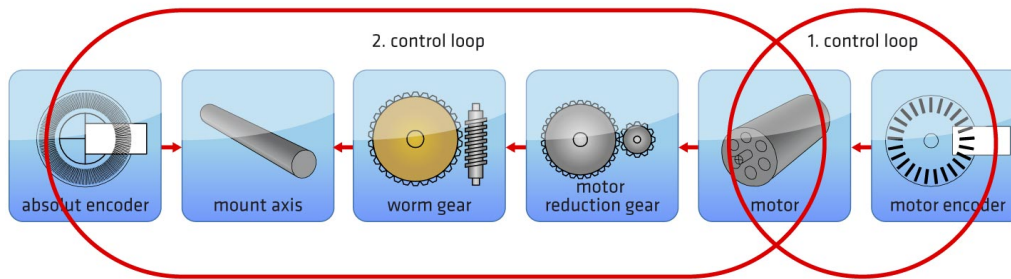
Figure 3.5.: Setup of a HPS mount[1]

motor-encoder. The encoder has a mediocre resolution and monitors the movement generated by the motor, more precisely the rotational speed of the motor axis. By mounting it directly on the motor axis, disturbances caused by the motor itself or other components can be measured by the encoder and be compensated. The motor encoder alone cannot guarantee a satisfactorily smooth run of the mount.

This is allowed for by the second control loop. It follows up the motor and consists of the motor's reduction gear, the worm gear, the mount axis and an absolute-encoder which is directly attached to it. The gear regulates the motor's pitch speed as appropriate for an accurate tracking. The worm gear transmits the movement to a bronze cogwheel in whose middle the mount-axis is affixed.

Mechanical imprecisenesses, e.g. uneven depth of cogs, backlash of the worm gear etc. can cause aberrations from the exact tracking speed. According to *10Micron*, these aberrations can sum up to about $4\,\text{arcseconds}$ per rotation of the bronze cog wheel[1] (Cheaper mounts suffer from errors up to $20\,\text{arcseconds}$ per period).

The absolute-encoder records these errors. This encoder has a very high resolution of 10 million increments per 360°. When any deviations from the predicted position are discovered, a correction signal is sent to the controls. By using this device the remaining error covers a range of about $0.25\,\text{arcseconds}$[1]. This lies way below the average seeing in Bamberg.

Another advantage of the absolute encoder is the impassiveness of the mount against accidental movements. Even when its turned off or pushed by hand, the mount never loses the orientation and can return to the desired position. This saved a lot of re-calibration time after a power outage during an observing session.

At this point another feature of the control unit should be mentioned. If a „traditional" mount is used, correction-signals (from a guider or an encoder) may happen to be over-transposed. This mainly happens with the declination-axis, because normally it is not moved during observing (disregarding the initial pointing sequence). If the motor of the axis receives a signal, it has to overbear the cohesion/the friction until the axis starts to turn. If the necessary force is exceeded, the axis makes a little jump. To avoid this behavior, the control unit constantly moves the declination axis back and forth, albeit only for some hundredth of arcseconds. This is small enough not to cause any visible errors in the pictures and enough for correction signals to be processed without overcompensation [Heinicke, 2012].

---

[1] 10micron.de/informations/difference-between-mount-drives/?lang=en

3.2.3. Assembling and startup

The new mount was installed together with the new telescope in September 2013. Beforehand an extension for the old *Zeiss* pillar was manufactured, which placed the mount $\sim 2.5\,\mathrm{m}$ above the ground level of the dome. This enables observations of objects with a lower declination and without the risk of getting trees or parts of the building in the visual field. The extension was fixed with screws to the upper part of the old pillar. The end plate is an adapter on which the mount was fixed using lock screws. But the height of the telescope is a disadvantage at the same time. If one wants to change the camera or use a Bathinov mask, it is necessary to use a ladder.

If two ore more cameras are operated at the same time, it is better not to power them with the same electrical circuit, or at least not the same plug socket. Otherwise interference could not be excluded. Therefore two different multi power outlet strips were mounted on the pillar (Main Bus A+B). It is suggested that only one camera is supplied by one power bus at the same time. However, the limitation concerning the power supply does not affect the data transfer. So it is possible to readout multiple cameras with only one active USB HUB (Data Bus). Some hook and pile fasteners were glued to the pillar to provide storage for hex wrenches or the hand pad. Figure 3.6 and 3.7 show a photo of the current configuration of the pillar with the main buses, the data bus and the fasteners.

The next step after completing the assembly of the mount was the pole-adjustment.
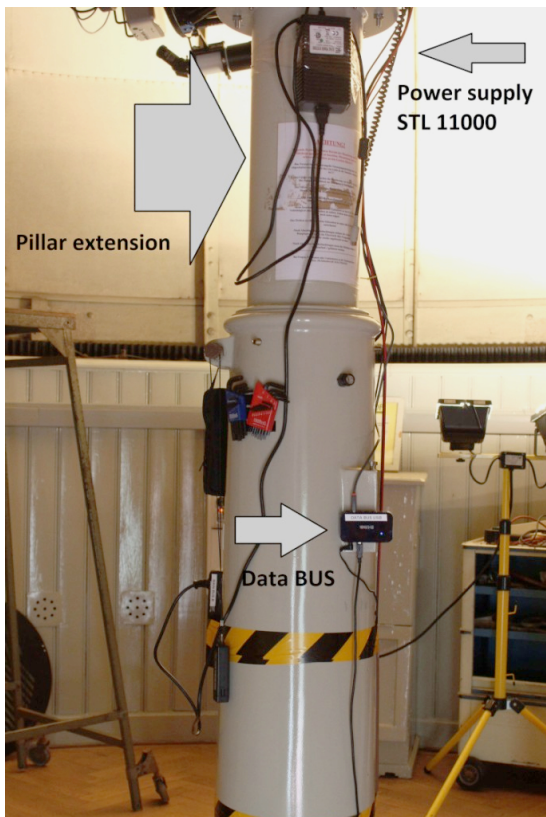
Figure 3.6.: Pillar, view from west   Figure 3.7.: Pillar, view from east
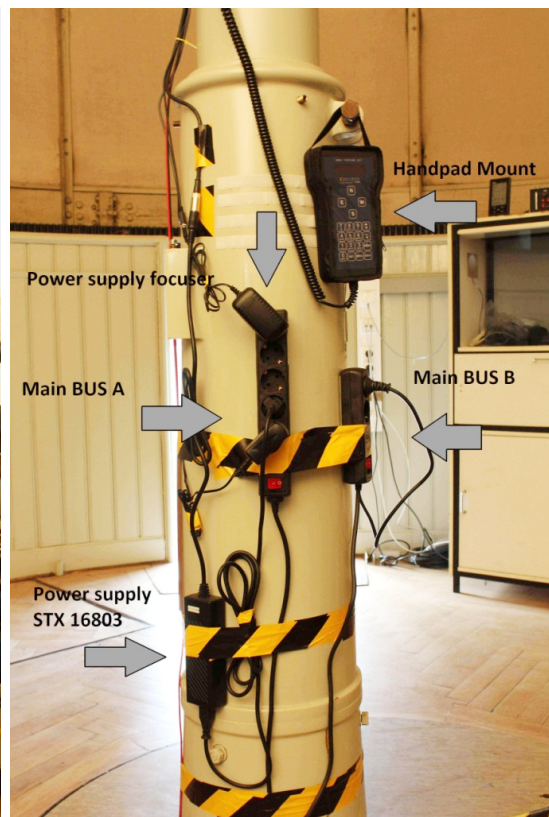
This means the orientation of the right ascension axis towards the celestial pole. The *10Micron* control software offers a comfortable solution. The mount points consecu-

tively at several stars which the observer has to center in the field of view. From the diversion of the initial position from the adjusted position, the deviation is derived. To guarantee the same center-position for all stars, a digital camera was used in combination with a digital cross hair. Additionally a Telrad-Finder[1] was installed. At first, only three stars were positioned. Afterwards a rough alignment was done. To do so, on the one hand the pole height was adjusted with the according screw, and on the other hand the mount was turned on the adapter plate to achieve a proper orientation in azimuth. Afterwards the aligned stars were deleted from the control unit, realigned and several other stars were chosen in addition. This procedure was repeated a few times until the pole-error was reduced to an acceptable value. During the last steps a maximum of 25 alignment stars were used.

From the position of these stars the control system calculates a pointing model. This model takes pointing errors into account as they arise from the remaining pole error, as well as the errors in position that are caused by the telescope, i.e. by the bending of the stiffeners supporting the secondary mirror. Furthermore the calculated pole error is used to derive a correction speed for the tracking of the declination axis. This is necessary for unguided, long exposures to compensate for field rotation.

After the alignment had been completed, a final pole-error of 41 arcseconds remained according to the software output.

To check the accuracy of the mount and the control software, the Single Axis Mount dynamics were determined by using the corresponding function in the camera control software *CCDops*[2].

The STX 16803 camera was connected to the mount via the ST-4 guiding port. The orientation of the camera, as determined by the adapters, aligned the movement in the x-axis along the chip alongside the right ascension axis and the y-movement alongside a movement in declination. However, a small misalignment of about 5° remained.

The camera took a picture of 3 s and a single, unsaturated star close to the optical axis was chosen and the position on the chip was determined. Afterwards the camera moved the mount for 0.1 s by activating the +X-relays for a tenth of a second and re-measured the position. This procedure was repeated until the star reached the edge of the pre-selected area. Then the -X-relays were activated for the same timespan and with the same step size. For an ideal mount in an ideal environment, the star would be detected at the exactly same positions as during the use of the +X-relays.

In reality the atmospheric seeing introduces an error to the measurement of the position. The exposure time of 3 s should average out most of the influence on the measurement, but a little error remains which was estimated to 0.5 pixels. The results of the measurement can be seen in Figure 3.8 for the R.A. axis and Figure 3.9 for the Dec. axis. Under ideal circumstances, both lines would be superimposed. Backlash, periodic errors or jumps of the mount could be seen as discontinuities or sinusoidal variations[3].

Despite a small error in declination (the starting point and the end point do not line up) the mount shows an almost perfect result. The displayed errors are within the

---

[1] http://de.wikipedia.org/wiki/Telrad-Sucher

[2] www.sbig.com/site/assets/files/18240/opsman4.pdf

[3] http://www.phys.vt.edu/~jhs/phys3154/TenThingsCCDOps.pdf
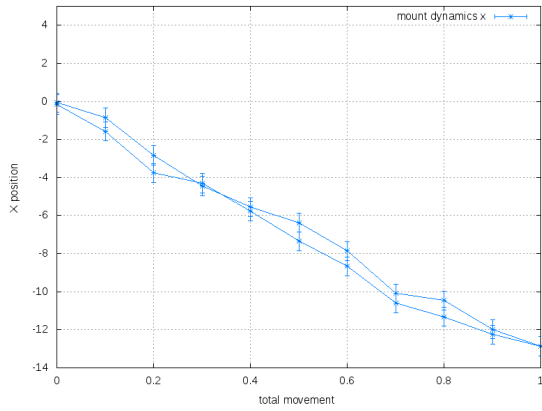
Figure 3.8.: mount-dynamics for x-move- Figure 3.9.: mount-dynamics for y-move-
            ment 0.1 s   ment 0.1 s
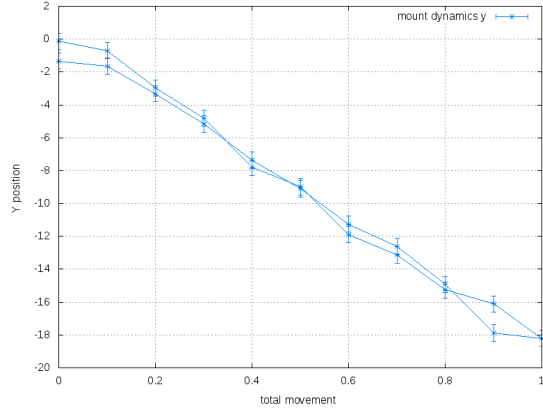
error-margin induced by the seeing.

If the resolution of the mount dynamics is enhanced, the picture changes a bit. Figure 3.10 and Figure 3.11 show the results with a total of 50 steps. Each lasted for 0.04 s. A clear backlash in both axis is visible. However, the result should not be
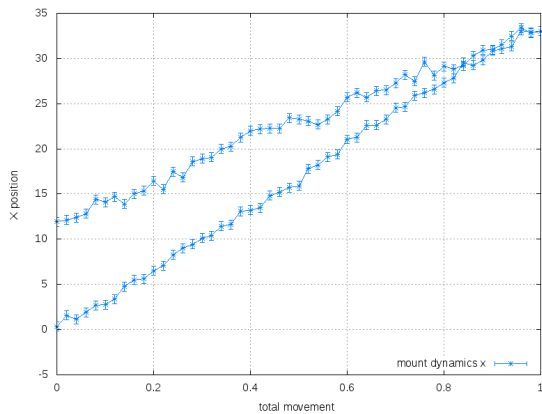
Figure 3.10.: mount-dynamics   for   x- Figure 3.11.: mount-dynamics   for   y-
             movement 0.04 s   movement 0.04 s
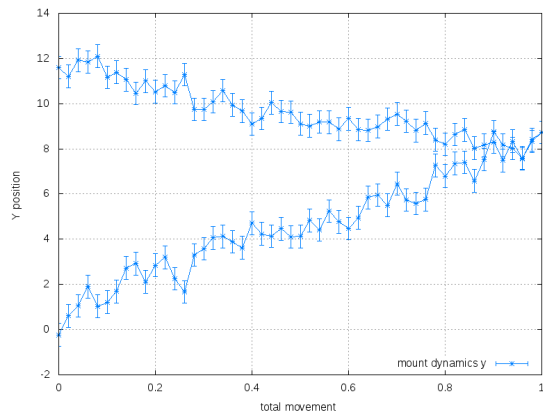
over-interpreted. According to the distributor, a stepsize of 0.04 s is in the absolute limit of the mechanical possibilities of the mount. In addition the ST-4 port should not be used for mount-diagnostics of this accuracy and has not been designed to handle such short signals correctly. But as the results gained with a stepsize of 0.1 s looked correctly, no further investigation on this topic was undertaken.

A larger version of all figures concerning the mound-dynamics can be found in Section C in the Appendix.

By selecting no relay in the mount dynamics dialogue, the program just monitors the movement of the mount during tracking. The results will be discussed in the following section.

3.2.4. Trouble shooting

During the first few weeks, the mount showed a remarkable tracking performance. It was possible to take pictures with an exposure time of about 10 min without any

external guiding control.

As winter approached and the temperatures during the nights began to drop, so did the tracking performance. At some point, exposures of two minute duration only were possible to achieve point-like stars on the chip of the camera. Several sources of error were examined, among others:

- imbalance of the scope

- backlash between camera and telescope

- movement of the pillar

Finally, it turned out, the mount suffers from a temperature-dependent tracking error, caused by the electronics of the control unit.

The tracking speed and the internal clock are controlled by an integrated quartz crystal. This oscillator dictates, together with the feedback signal of the encoders, the tracking speed for both axis. If the quartz crystal is oscillating too slow or too fast, the real tracking speed differs from the optimal/calculated one without being recognized by the control unit. It is not implicitly caused by the quartz itself. Other components of the control system could be responsible as well. Up to now, it could not be clarified if all *10Micron*-mounts suffer from this problem or if it is caused by an inaccurate element in the mount's control unit. So far no statement of the manufacturers has been made upon this topic.

To compensate for the problem, there are two possibilities: External guiding or an internal correction of the crystal's oscillation speed.

The first one, guiding, brings the disadvantage of more sources of error and a time consuming setup. Therefore it was decided to make use of a software feature of *10Micron* mounts, the oscillation speed-control [Heinicke, 2012]. To use this program, the observer has to determine the discrepancy between the actual- and the required tracking speed. To simplify this process, a little *Python*-script was been written during this thesis, which can be found in Section B.1 in the Appendix.

The program requires the exposure time of an image, the length of a startrail in right ascension and the declination of the observed object. The input works with while-loops to increase user friendliness and to avoid aborts due to incorrect inputs. The program calculates the tracking speed from the length of a startrail and the field of view for one camera-pixel in consideration of the exposure time. This value is compared to the theoretical tracking speed at the selected declination.

The STL 11000M features a field of view of $35.83' \times 24.38'$ and a pixel array of 4008×2672 which results in a field of view per pixel of $0.537''$.

This program works for the SBIG STL 11000M and the SBIG STX 16803 as their sensors have the same pixel-size of $9\,\mu m$ and the same number of pixels in the direction of right ascension. It does not work for smaller chips, CCDs with smaller pixels or color-chips.

To test both, program and mount, a single $900\,\text{s}$ image of M1, the Crab Nebula, was taken. Beforehand the correction factor for the quartz oscillator was calculated and applied. The image is shown in Figure 3.12. As one can see, the stars are round. This means that the tracking is accurate and that the image field is flat and free from aberrations, as promised by the manufactures.

To gain a direct comparison between the corrected and non-corrected performance, the mount dynamics explained in the previous section were used. By selecting no

Figure 3.12.: Messier 1, Crab Nebula with 900 s exposure time

relay the program simply monitored the movement of the star that is caused by seeing and impreciseness of the tracking. Figure 3.13 shows the results. The camera's orientation was chosen to overlay the X-axis of the chip and the right ascension axis. For the red curve, no correction was applied. After roughly 300 seconds a drift of up to 4 pixels was reached. Afterwards the correction factor was determined to 0.04% and the measurement was repeated. Now the fluctuations of the position lie within ±1 pixel. The observable scattering is most likely due to the seeing limitations. During the usage of the mount, tracking corrections for several different temperatures were applied. The temperature was measured with the internal temperature sensor on the back of the main mirror. It is not equivalent to the temperature of the control unit or the quartz, but as this should only lead to an offset and not change the basic variations of the correction factor, therefore it was neglected here.

Figure 3.14 shows the data collected so far. The error of the temperature measurement was estimated to $\pm 0.5°\,C$ and the error for the correction factor was set to 0.005 or 0.01, depending on the quality of the image, used for the calculation. So far it seems that the correction factor would remain constant at temperatures above $20°\,C$. Below that, a strong temperature dependence can be seen.

Probably some parts of the quartz-control suffer from an error at low temperatures that is slowly compensated by other elements as the outside temperature rises. When a certain temperature regime is reached, the error is negligible and only a constant offset remains.

During the preparations for the MAPLE Project (see Chapter 7) the performance of the alignment model was investigated. It turned out, that the mount is capable to perform even longer exposure times than the 900 s mentioned beforehand, but only for certain areas of the sky. If the target is close to the zenith and the correction factor is applied, exposure times over 20 min are possible. Figure 3.15 shows an exposure of 20 min of NGC 7380, the Wizard Nebula. A magnification of the innermost part of the picture is placed in the bottom right corner. All stars are
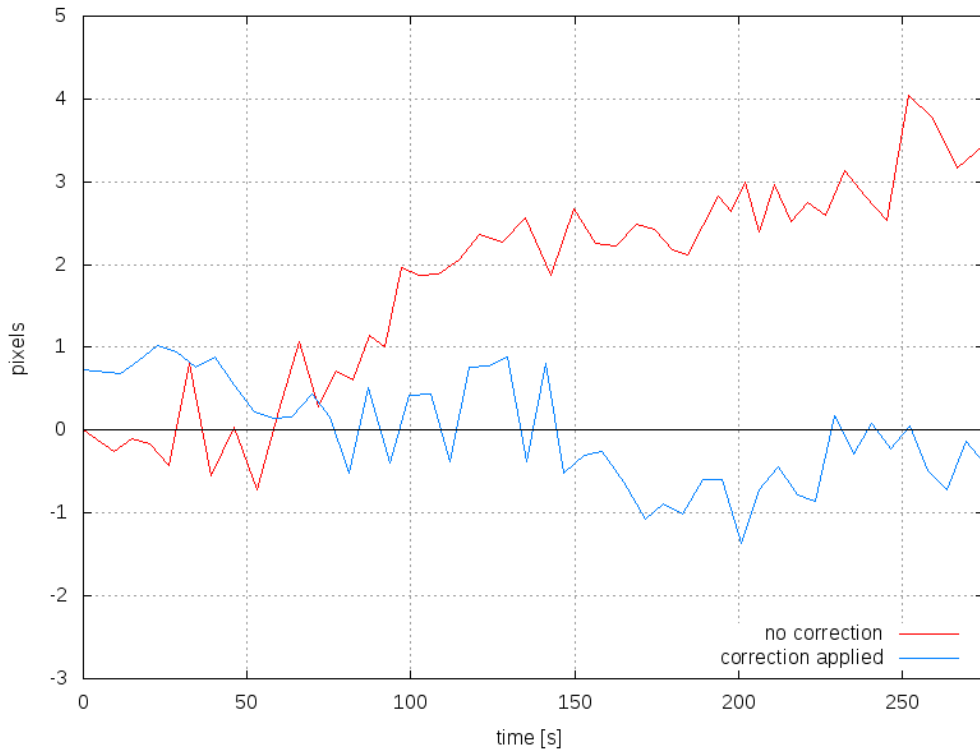
Figure 3.13.: Comparison of mount dynamics with and without applied quartz correction
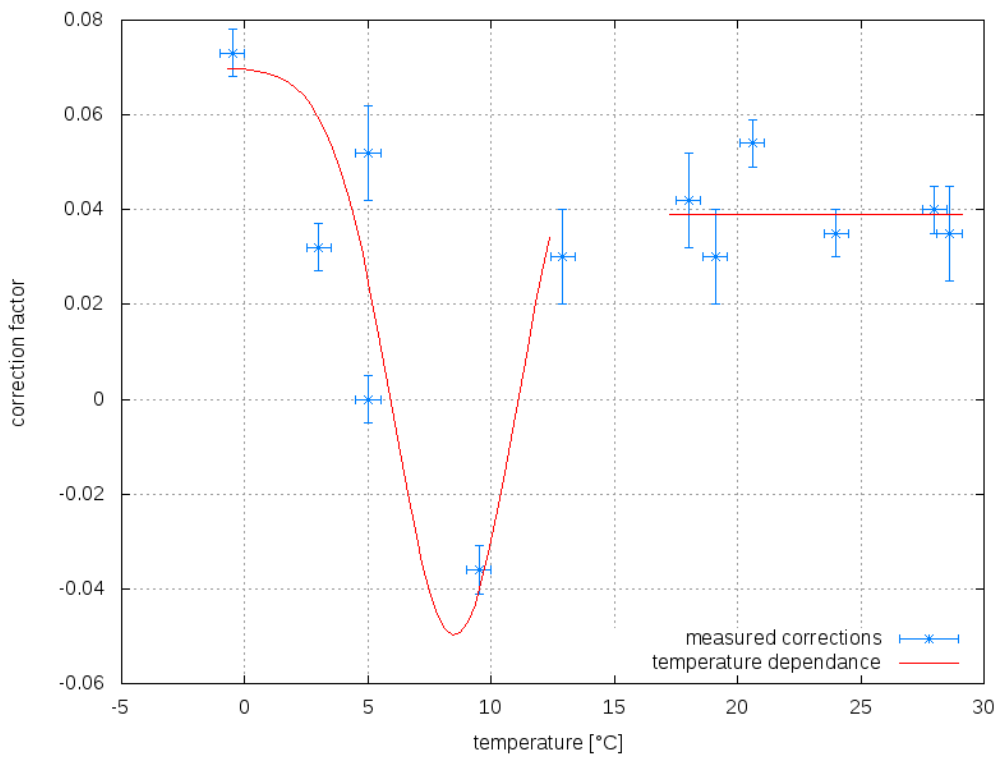
Figure 3.14.: Dependence of the correction factor of the temperature

34

Figure 3.15.: NGC 7380, 20 min exposure with a red filter, unguided

perfectly round. From experience, it can be assumed that even some more minutes of exposure time would still have been possible. However, even this result is far better than the specifications published by the manufacturer, especially if the focal length and the weight of the EHT are taken into account.

To give a summary of the presented results, it can be said that the new mount and the new telescope are capable of delivering high quality results and that the alignment of both systems was very successful.

3.3. SBIG STL 11000M

The STL 11000M is a monochrome CCD camera produced by the *Santa Barbara Instruments Group - SBIG*. It features a Kodak KAI 11000M sensor, where M stands for microlensing, a technique used to enhance the quantum efficiency of an imaging sensor. It is equipped with Anti-Blooming Gates to allow longer exposure times without nasty blooming lines below bright stars. On the other hand, these gates disturb the linearity of the chip for bright sources. The KAI 11000M is an Interline-Transfer Chip. This allows very short exposure times but decreases the filling factor

to about 30%. Interline chips transfer each column into a separated register from where the electrons are shifted to the read-out area[1]. The chip can be cooled down to $-30°$ C to reduce the dark current and pixel defects. An internal filter wheel is capable of storing up to five round 2" filters. Downloading images is done via USB 1.1, which results in comparatively long download times (30 s for a full frame, 12 s or a 2×2 binned frame). The camera hosts an internal guiding chip, which remained unused, because the old interface is incompatible with the new mount.

The photometric shutter makes it possible to take short-exposed images without the characteristic iris-like pattern on the image. This is very important for a precise flatfield correction of images. Our chip suffers from a large amount of hot pixels and a few defect columns. Both effects can be handled very well by using darkframes and flatdarks. A single, unprocessed darkframe is shown in Fig. 3.16. Note that there is a gradient caused by the dark current and the layout of the chip (Interline Transfer).
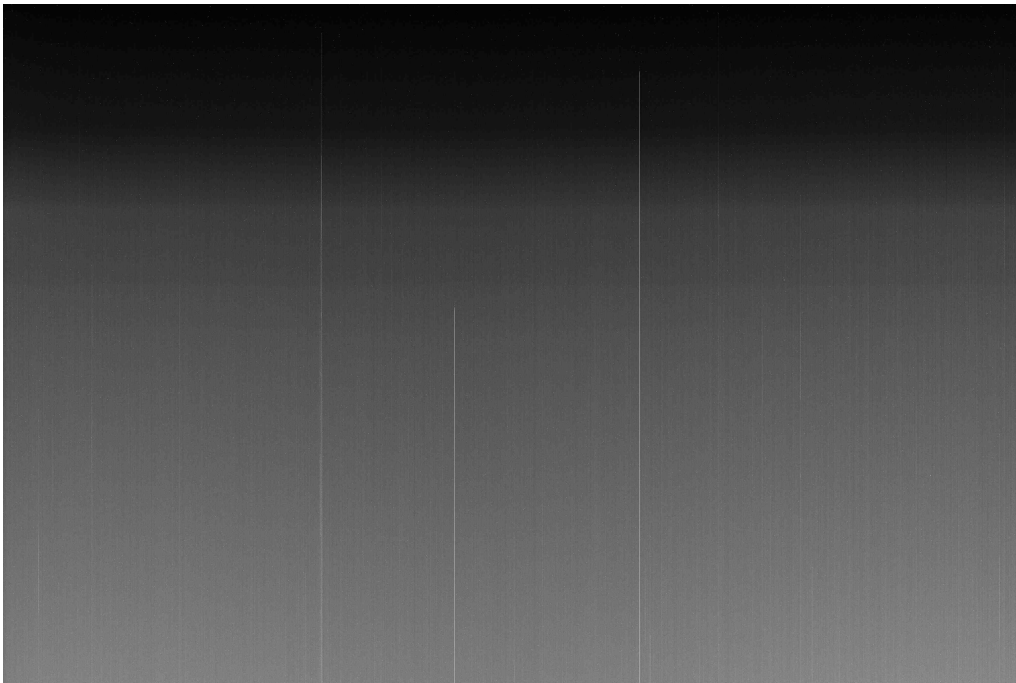
Figure 3.16.: Darkframe STL 11000M, unbinned, 60 s exposure at $T = -17°$ C

3.4. SBIG STX 16803

Since June 2014, the SBIG STX 16803 has been available as successor for the STL 11000M. The STX is a state-of-the-art research camera. The monochrome, quadratic CCD chip has a peak quantum efficiency of 60% at 550 nm[2]. Like all fullframe chips, the 16803 has a filling factor of 100%. This means that the whole surface is sensitive to light. Fullframe chips transfer the charge through the normal pixel towards the read-out area. This requires a shutter in the camera to prevent light from being

---

[1]http://www.pco.de/fileadmin/user_upload/db/download/KAI-11000CMLongSpec.pdf

[2]http://www.ccd.com/pdf/ccd_16m.pdf

detected by the pixels during read-out.

As the STL, the chip of the STX also features Anti-Blooming Gates and microlenses to increase the sensitivity. It can be cooled to $50°\,\mathrm{K}$ below ambient temperature. The STX features an internal guiding chip. Together with a ST-4 interface, this enables enhancing the exposure time without the need to use a secondary guiding camera or applying the quartz correction, at least theoretically. In practice it turns out to be quite time-consuming and frustrating to find an appropriate guiding star. The situation is worsened by the large primary CCD chip. As a consequence, the guiding chip is placed in the very corner of the flattened field of view and the stars are not point-like anymore but elongated in one direction. This results in problems as the guiding program has difficulties with fitting Gaussians to the star-images in order to determine the position on the chip. By reducing the resolution of the guiding chip (binning), the guiding results can be improved as the stars become smaller and rounder.

The camera does not contain an internal filter wheel, but an external device, storing five square 60 mm filters, can be mounted between camera and telescope.

There is a maximum of five defect columns and only very few hotpixel, depending on the temperature of the chip. The defect columns are only visible at temperatures above $0°\,\mathrm{C}$. Figure 3.17 shows a darkframe, taken under the same circumstances as with the STL 11000M. The contrast was enhanced, otherwise the whole image would have been black on printouts. Because of the layout of the chip (fullframe),
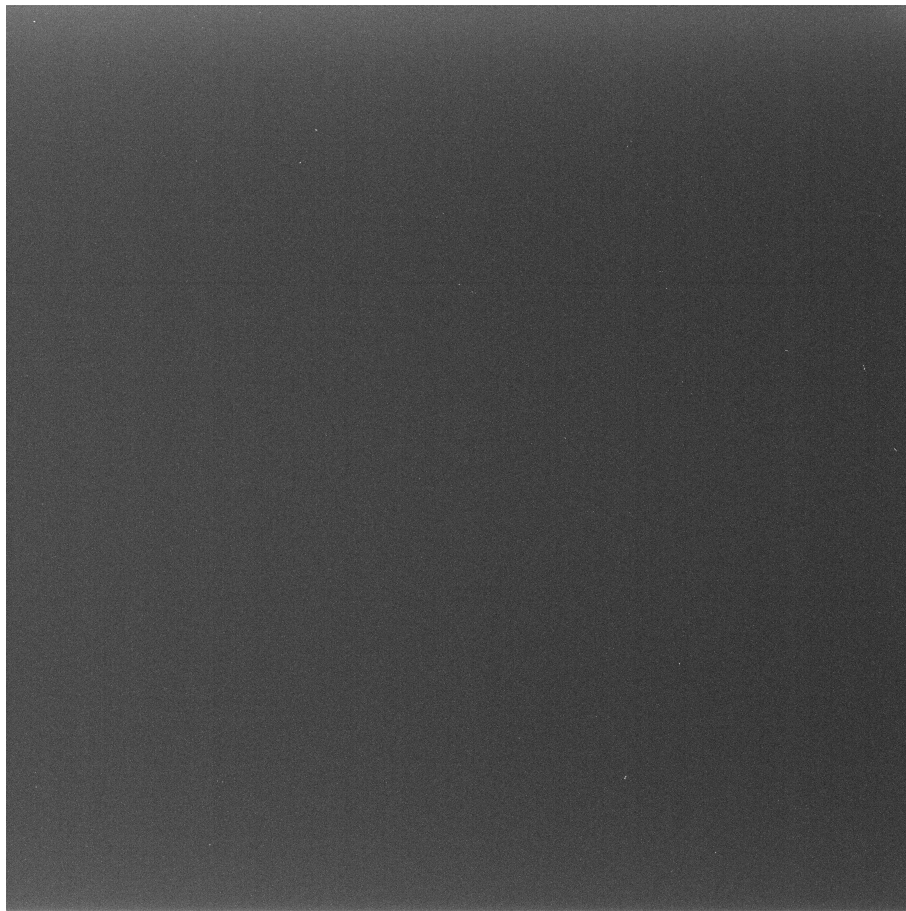
Figure 3.17.: darkframe STX 16803, unbinned, 60 s at $T = -17°\,\mathrm{C}$

virtually no gradient caused by the dark current is visible. In addition the number of hot pixels is comparatively low.

While taking flatframes, we encountered problems with the red filters.

All flat fields were made by using a special flat field panel by Gerd Neumann[1]. These panels consist of an electroluminescent foil between two plastic plates and emit a very even light that is perfect for making flat fields.

If the camera is operated with a 2×2 binning, the sensitivity is too high and all flats are overexposed, even for the shortest exposure time possible. To counteract this problem, a wooden frame was constructed which holds different pieces of plastic sheets. The frame is large enough to cover the whole diameter of the telescope and is placed between the flatfield-plate and the front structure of the telescope. By selecting specific colors of the sheets, it could be achieved that the red-flatfields require an exposure time 4 times longer than the shortest possible timespan.

The SBIG 16803 features a heated sensor window just in front of the CCD. This should guarantee a dew-free surface. In practice, dew problems were encountered during very humid nights only. The electric current to heat the window is quite small. Otherwise, it would induce seeing in the connector between camera and telescope. As a result the middle of the window is cooler than the edges as heat is transferred to the cooled chip, providing a contact surface for condensation. The problem was solved by inserting a small pack of desiccant into the tube before observing so that a more or less moisture-free environment is created. Additionally two desiccant plugs have been inserted into the camera case to reduce moisture on the circuit boards of the camera.

If the camera is not used for more than three days or the humidity in the dome increases to above 65%, the camera should not stay attached to the telescope but should be stored in the dry case.

---

[1]http://www.gerdneumann.net/deutsch/astrofotografie-parts-astrophotography/
aurora-flatfield-panels/uebersicht-aurora-flatfield-panels-overview.html

4. Eclispe timing of sdB and WD binaries with the EHT

4.1. Basic information

For the scientific usage of the EHT it was decided to focus on the eclipse timing of binary systems. As explained in Section 2.4.3, this method can be used to search for third bodies, like exoplanets, in eclipsing binary systems. As it was unclear how the new telescope would perform, taking lightcurves of comparatively bright systems ($\rightarrow$ short exposure times) seemed to be a safe idea. But as described in the previous chapter, there was no need for worries and the new equipment performed much better than expected.

The project is related to the DWARF Project [Pribulla et al., 2012], an observing campaign that tried to gather a large database of eclipse timings from different observatories, including amateur astronomers with large telescopes. But in contrast to the DWARF project, it was decided to limit the targets to sdB and WD binaries (see the following section) and focus on well-known systems with many information about the physical and orbital parameters.

4.2. Acquisition and processing of data

The following chapter describes the acquisition of data with the EHT and its processing.

4.2.1. Target selection

Hot subdwarf B stars and White Dwarfs were selected from the list published in Pribulla et al. [2012], in addition two other eclipsing binary systems containing a White Dwarf were chosen. All targets lay in the northern hemisphere with a declination larger than $-10°$. The brightness covers a range from R=10 mag to R=17 mag and the orbital periods lay below 9 hours. An overview of all targets can be found in Section 4.3 and in Table .1 in the Appendix.

To check if the star is visible and observable from Bamberg, the Object Visibility tool, provided by the Issac Newton Group of Telescopes (ING) was used[1]. This tool determines the best time to observe an object (i.e. when both the separation from the horizon and the moon distance is largest). As it is only important to determine the exact timing of the primary eclipse, it is usually not necessary to cover a full orbital period of the system. The eclipse time can be calculated from the period of the system and the known ephemeris. Both were published in Pribulla et al. [2012]. As it is quite time consuming to do these calculations per hand, a *Python* program

---

[1]`catserver.ing.iac.es/staralt/`

was written. It can be found in Section B.2 in the Appendix.

The program requires the ephemeris, period and the actual date (in years, month and days). It then calculates the corresponding Julian Date (JD) and the first eclipse of the system on the entered date. The next step is entering the number of eclipses that shall be displayed. Long periods usually require only two or three events, while short periods make it necessary to display up to ten or more periods.

The program can also be used as a basis for the O-C calculation performed later on (see Section 4.3.1,) as it provides the ability to predict the eclipse time.

4.2.2. Telescope set-up and focusing

Roughly one hour before the start of the observations, it is helpful to open the dome slit completely. This enables a temperature adjustment between the inside and the outside to reduce dome-seeing during the observations. After removing the covers from the mirrors, the open part of the tube is covered with a black nylon stocking in order to prevent stray light issues.

After the mount has been switched on, it is necessary to synchronize the internal clock of the mount to the local time. Otherwise the impreciseness of the quartz oscillator would lead to increasing differences between real-time and system-time, resulting in a bad pointing accuracy. The website `uhrzeit.org` has been used for the synchronization as it offers a direct link to an atomic clock.

Thereafter, the telescope is slewed to a bright star and focused with a Bathinov mask. An example for a correct focus can be found in Section A in the Appendix. The star has to be centered in the field of view so that the mount can be resynced to its position. This is necessary to maintain the pointing accuracy of the system. Otherwise, small errors of the encoders would add up after some nights.

It is important to select the filter that will be used for the observations before focusing the telescope. All filters are said to be homofocal, but minor differences in the focus-position have been detected, especially with narrow band filters.

Depending on the expected exposure time, it might be helpful to do a long exposure to determine the quartz correction factor. If the exposure time is longer than three minutes, the quartz correction is necessary. If the exposure takes longer than eight minutes, guiding is recommended.

After these preparations, the telescope can be slewed to the selected target. Although the pointing accuracy achieved with objects listed in the control unit (Messier, NGC, etc.) is very good, the accuracy when entering only the coordinates of a target is somehow worse. The target is usually only within 15'. Therefore it is necessary to have a finding chart and to recenter the object manually.

4.2.3. Data acquisition and basic processing

The exposure time should be as short as possible to ensure a good timing resolution but nevertheless be long enough for a suitable S/N ratio. In practice, a difference between the center of the target and the background of about 800 ADU to 1000 ADU is recommended (ADU=Analog to Digital Unit). After selecting the required number of exposures, the AutoGrab dialog controls the camera and the observer's only remaining task is to check the dome from time to time and change the position of the slit.

After finishing the observations three sorts of correction images have to be taken.

- **Darkframes** compensate for hot pixels and a gradient caused by the dark current

- **Flatfields** remove an uneven illumination of the chip and take the different sensitivity of the pixels into account

- **Flatdarks** are taken with the same exposure time as the flats and correct the flats from hot pixels and gradients

The flatfields and flatdarks can be taken before the observations. The number of darks should be around 10 to 15 while it is sufficient to take up to 10 flats and flatdarks.

The basic processing of the data was done using the freeware $FITSWORK$[1]. Fitswork was written by Jens Dierks and is ideal for working with large data. In addition its calculations are operated with 32 bit color-depth and floating decimal, which increases its accuracy.

At first the darks and the flatdarks are averaged to a master(flat)dark. Each flat is corrected with the masterflatdark by subtraction. Afterwards, a masterflat is created by coadding all dark-corrected flats. The masterdark is subtracted from every single light frame and the resulting picture is divided by the masterflat.

Fitswork offers two options within the subtraction of darkframes:

- **Temperature compensation**
  The program reads the CCD temperature from the FITS-Header and interpolates the signal intensity in each darkframe if the temperature has changed. Applying this filter could influence the integrity of the photometric data and was not used. Despite that it is not really necessary with our cameras, as the chip temperature can be kept within some tenth of a degree during the observations, it is helpful when using uncooled cameras for measurements.

- **Hot pixel correction**
  The hot pixel correction detects all hot pixels that have not been removed with the dark subtraction. Afterwards their value can be replaced by the average of the surrounding pixels. This filter was activated, as it proved to work very reliable. Any negative influence on the data is much smaller than it would be if a hot pixel is not detected and used for the photometric analysis.

After theses steps the lightframes are basically ready for a photometric analysis. But to simplify the following procedure all lights should be aligned with each other, so that the image-coordinates of an object do not change within different pictures. This is easily achievable with Fitswork's multi-point alignment algorithm that automatically corrects for shifting, rotation or forging of the pictures.

4.2.4. Photometric measurements

The photometric measurements were done using Russ Laher's Aperture Photometry Tool (APT hereafter)[2]. The information about the program in this section are taken

---

[1]www.fitswork.de/software/

[2]http://www.aperturephotometry.org/

from Laher et al. [2012].

APT is a GUI based photometry program that, unlike other programs i.e. *SExtractor*, forces the user to look at the images he wants to measure. However it is impractical for processing a large number of images, as each one has to be loaded and handled separately (see also Chapter 7). The reason that it was chosen for the analysis of images gained with the EHT is the necessity to look at the data. It can be ensured that the stars are point-like sources and no tracking errors have occurred in any images, that there are not black-, hot-, or missing pixels inside the aperture or the surroundings and that no satellite or airplane passed through the field of view and probably disturbed the measurements.

After loading the image and locating the source of interest, the aperture has to be set up. Usually the aperture is circular, but it is possible to use elliptical apertures to allow to measure galaxies or stellar images that are elongated due to tracking problems.

APT offers different modes for measuring and calculating the brightness of a source. A detailed description can be found in Laher et al. [2012]. For single stars model 2D has proved to work best. Model 2 means that radial profile interpolation has been done for all pixels and D means that a sky-average subtraction is applied. „The average times the number of pixels in the aperture form a product that is the sky contribution subtracted from the integrated image data of the source to get the background-subtracted source intensity" [Laher et al., 2012]. If there are other bright sources in the area that has been selected for the background estimation, it might be helpful to change to model 2B, the sky-median subtraction, as it is less sensitive to other bright sources in the sky annulus. The radial profile interpolation mentioned above makes the analysis less sensitive to the side-effects of noise in the pictures and produces somewhat smoother results than models without interpolation. The profile can be described via

$$S(r) = A + Br + Cr^2 + Dr^3 + Er^4 + Fexp\left(\frac{-r^2}{2\sigma^2}\right) \tag{4.1}$$

S(r) is the brightness with respect to the radial distance from the center, A to F are determined via linear regression and σ is a parameter that can be used for optimizing a fit. Before processing images, the radial-profile has to be determined for one source and is saved. This function should only be applied if the Point-Spread-Function (PSF) of the telescope does not change too much over the field of view. This constraint is fulfilled for the combination of the EHT and the SBIG cameras. Otherwise a wrong interpolation would be done for different sources, leading to incorrect results.

Another feature of APT is the aperture correction. This is a multiplier > 1 that is used to correct for too small apertures, e.g. source intensity outside the aperture. According to Laher et al. [2012] it is always needed because of limited bandwidth considerations. In practice, its use can be justified by looking at the dependence of the S/N ratio of the aperture size. If the size of the aperture is enlarged, the source is more fully contained in the inner annulus, but the noise encompassed is increased and, as a consequence, the S/N ratio is decreased. Therefore it can be helpful to select the radius of the aperture a bit too small. Figure 4.1 shows a typical aperture, displayed as a slice through the source. Figure 4.2 shows the accumulated source intensity. Note that the overall source intensity still grows a bit
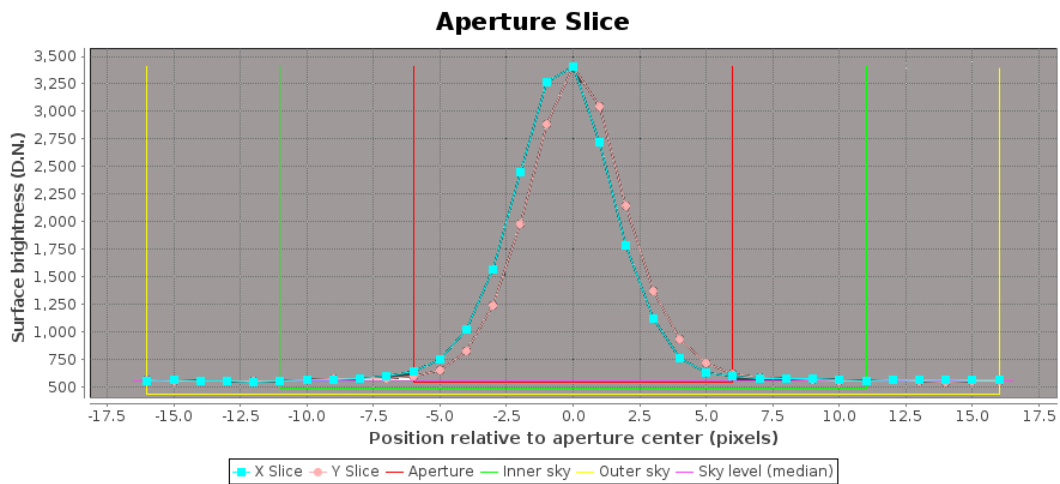
Aperture Slice

Figure 4.1.: Aperture slice through a source. The inner annulus is used to measure the source intensity, while the area between the outer two slices estimates the sky background

after the edge of the inner annulus. This is encompassed by the aperture correction, which is automatically carried out for every picture loaded. If desired, APT can
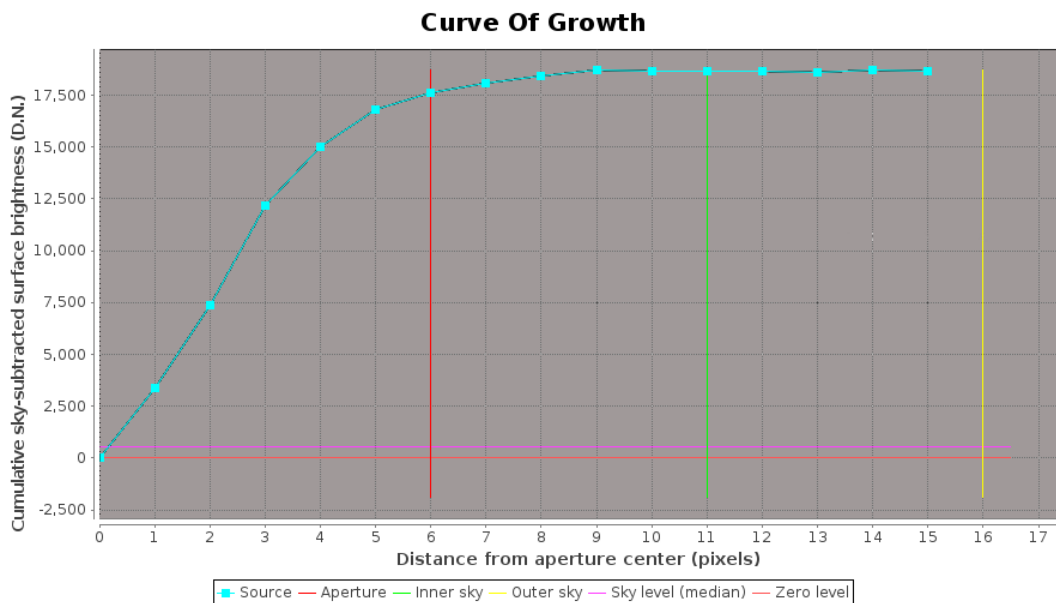
Curve Of Growth

Figure 4.2.: Curve of growth showing the accumulated source intensity and the three apertures

automatically center the aperture on the source. This can either be done manually by clicking the corresponding button or it is done automatically when using the automatic processing of source lists to investigate a larger number of objects in one picture. The center of a source is computed by an iterative method with a maximum of 100 runs. The first iteration is computed from the user-selected position via the bootstrapping algorithm. The iterations follows equation 4.2 for the x-position as

43

well as for the corresponding y-position.

$$x^k_{centroid} + 1 = x^k_{centroid} + \frac{\sum_{i,jES(k)}(x_i - x^k_{centroid})(d_{ij} - d^k_{min})}{\sum_{i,jES(k)}(d_{ij} - d^k_{min})} \qquad (4.2)$$

The sums are over all pixels in the inner annulus. d_{ij} is the image data value at pixel (x_i, y_j). d^k_{min} is the smallest value in the centroid aperture circle. APT reaches sub-pixel resolution, with a minimum accuracy of 0.05 pixels.

Of course, the values for the measured brightness come with an error. The uncertainty displayed by the program follows equation 4.3.

$$\sigma_{src} = \sqrt{\frac{F_{src}}{\eta G N_{depth}} + A_{src}\sigma^2_{sky} + \frac{\kappa(A_{src}\sigma_{sky})^2}{A_{sky}}} \qquad (4.3)$$

F_{src} is the sky-background-subtracted source flux density, G is the gain of the used detector, N_{depth} is the depth of coverage, η is a conversion factor used to switch from image data-units to D.N. (data units), A_{src} is the area of the aperture in square-pixels, σ_{sky} is the sky background standard deviation per pixel, A_{sky} is the size of the area used for the background estimation and κ is a factor to account for different models (for the sky-average subtraction it equals 1.0, for the sky median subtraction is is equal to $(\pi/2)$. Equation 4.3 is only valid for single images, not for coadded ones. The first two terms of the equation are explained in Bertin [2006]. The third term under the square-root takes the uncertainty of the background estimation into account.

After the object of interest has been measured, it is necessary to measure some other stars in the same picture as a reference to check if the overall brightness or sky quality has changed or not. Otherwise these changes could be interpreted to have a stellar origin. The calibration stars should have roughly the same brightnesses as the target and should lie close to it in the image to reduce possible gradient effects. After all pictures and sources have been measured, an output file is generated that lists all the data (and more) necessary and unnecessary for the further processing.

4.2.5. Eclipse timing

Before the eclipses can be determined, the output file generated by APT has to be edited and transferred to a more practical format. This includes removing all unnecessary data and rearranging the lines. This can be done with the *Python* program in Section B.3 in the Appendix.

This program is able to read the APT output file and extracts the important parts. The user can select if he wants the magnitude or the intensity of the star to be used. Furthermore the software can read the FITS-Header of images placed in the same directory, extract the date and start-time of the exposure and combine it with the corresponding photometry values. It is important, that the number of images and processed pictures in the APT file is the same, otherwise an error is generated.

After the new file has been generated, it has to be checked if the calibration stars are constant during the session or if they show intrinsic variations, like eclipses. Therefore their lightcurves have been plotted using $GNUPLOT$[1]. By manually shifting

---

[1]`www.gnuplot.info`

the first datapoint of all comparison stars to the same value (only for the plotting procedure, the value itself was not changed) sudden increases or decreases of brightness could be easily seen during visual inspection. Those stars were removed from the sample and not used for comparison.

Figure 4.3 shows the effect of comparison stars. In the left image, the brightness of DE CVn (see Section 4.3.4) was plotted versus time without any correction. There is a large scattering observable and no eclipse can be seen. After subtracting the mean value of all comparison stars from the original brightness and shifting the continuum to value zero, the right hand side picture results. Now the eclipse can be clearly seen. A larger version of these images can be found in Section D, in the Appendix. The correct time for each data point can be derived from the FITS Header of each
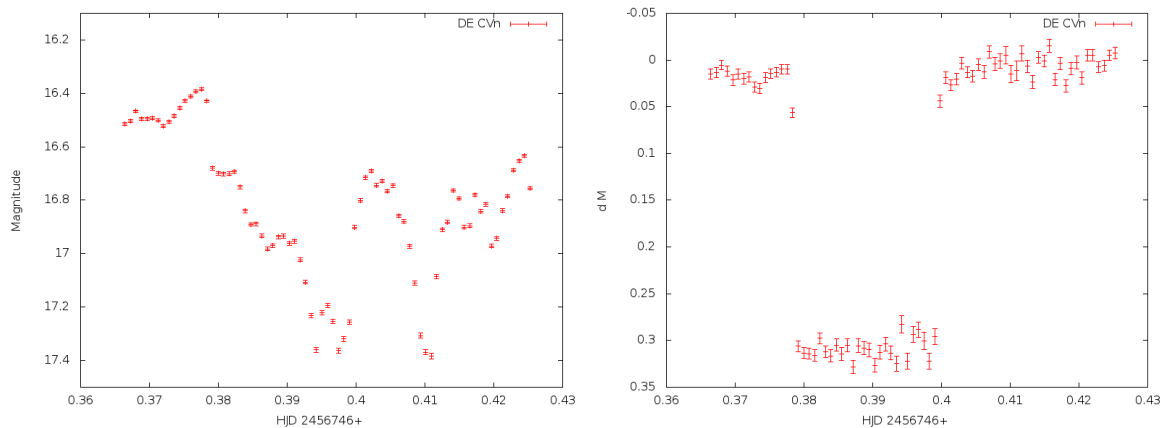
Figure 4.3.: DE CVn before and after applying the brightness correction by comparison stars

picture. It corresponds to the computer time at the beginning of the exposure and is given in hours, minutes and seconds. In order to achieve comparability between different datasets all times had to be shifted to Barycentric Coordinate Time. This means converting the universal time from the header to Julian Date (JD) and applying the barycentric correction. This can be achieved with the self-written *Python* program displayed in Appendix B.4. It is able to read the output file generated in the previous step and to extract the time information. This time is converted to JD in the usual way. Afterwards the barycentric correction (computed with MIDAS manually beforehand) is applied. Finally half the exposure time is added to every data point to shift the image time to mid-exposure time. The result is appended to the original output file. The effects of the shutter delay described in Pribulla et al. [2012] were not applied as it was not possible to measure them adequately. By taking the shortest possible exposure time of 0.18 s for the STX camera into account, their value should not exceed more than a tenth of a second. This means that they are negligible in comparison to the errors claimed by the Gaussian fit explained hereafter.

To determine the exact timing of the eclipse, *GNUPLOT* was used to fit a Gaussian to the eclipse.

$$f(x) = a \cdot \left(\frac{1}{b\sqrt{2\pi}} \right) \exp \left(-\frac{1}{2} \left(\frac{x-c}{b} \right)^2 \right) + d \qquad (4.4)$$

As the x-axis shows the time, the variable c gives back the center of the Gaussian and therefore the timing of the minimum. *GNUPLOT* uses the Marquardt-Levenberg algorithm for the fitting process and the estimation of errors. An example for a Gaussian fitting to a processed lightcurve of HW Vir can be seen in Figure 4.4. For
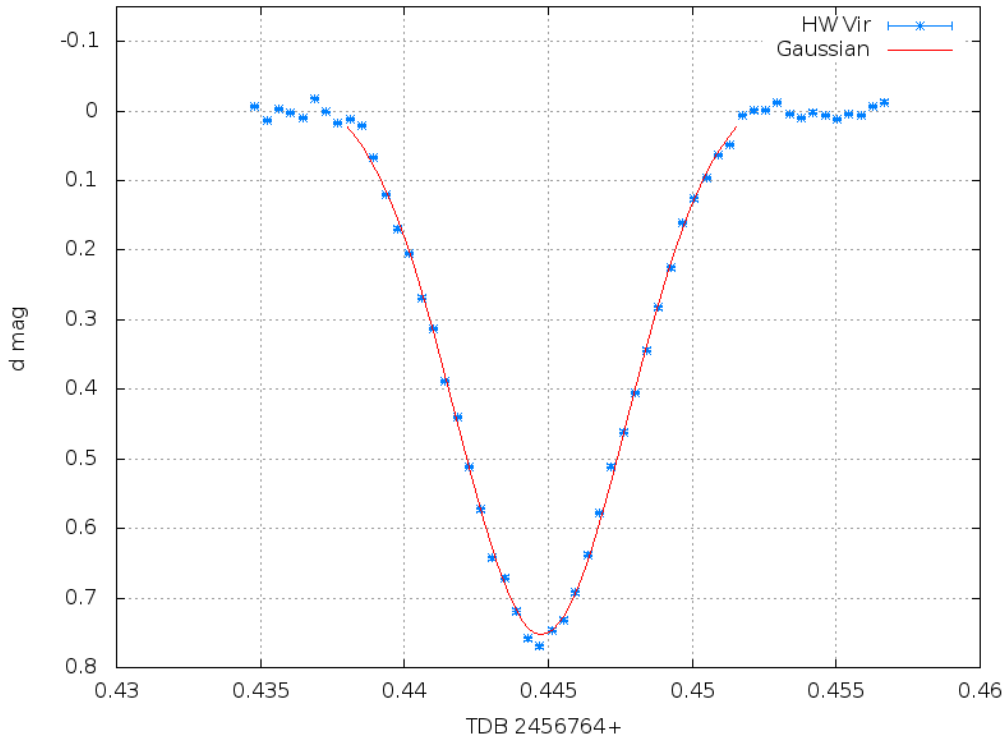
Figure 4.4.: Lightcurve of HW Vir including fitted Gaussian

„rectangular" eclipses, the Gaussian cannot be used. In such cases, the approach described in Section 4.3.4.2 was used.

4.3. Observed stars

A full list of all observed stars and the determined mid-eclipse times can be found in Table .1 and Table .2 in the appendix.
Targeted sdB binaries were V470 Cam, HW Vir, NY Vir, as well as the white dwarf binaries DE CVn, DP Leo and GK Vir.

4.3.1. V470Cam

4.3.1.1. Basic information

V470Cam (=HS0705+6700) was discovered to be an eclipsing binary by a photometric monitoring program at the Nordic Optical Telescope [Drechsel et al., 2001]. Originally it was planned to search for pulsations, but this search did not reveal variations at the appropriate timescales, instead an eclipse lightcurve was discovered. The system, consisting of an sdB and a M dwarf, was found to have a period of 2.952 h and an inclination of 84.4°. For the primary, an effective temperature

of T = 29000 K and a surface gravity of log g=5.4 were derived by a quantitative spectroscopic analysis.

Drechsel et al. [2001] suggested that the further evolution of HS0705 might lead to a cataclismic system with a period below the period gap within 10^9 years.

HS0705 was the third known system of the HW Vir type. Variations in the eclipse timing have been detected, which can be interpreted in several ways. Recent investigations by Beuermann et al. [2012a] indicate that there is a substellar companion to the system.

4.3.1.2. Testbed for accuracy

As V470 Cam was the first eclipsing system that was observed with the EHT, it was used to check the accuracy and quality of the gained data and the reduction process. As Prof. Drechsel was involved in the discovery of the system, it was possible to compare the data from Bamberg to the original data taken with the Nordic Optical Telescope (NOT), a 2.5 m telescope, much larger than the EHT. Figure 4.5 shows the result, with the normalized flux plotted against the orbital phase of the system. Of course, the time resolution of the NOT-data is much better, as the exposure
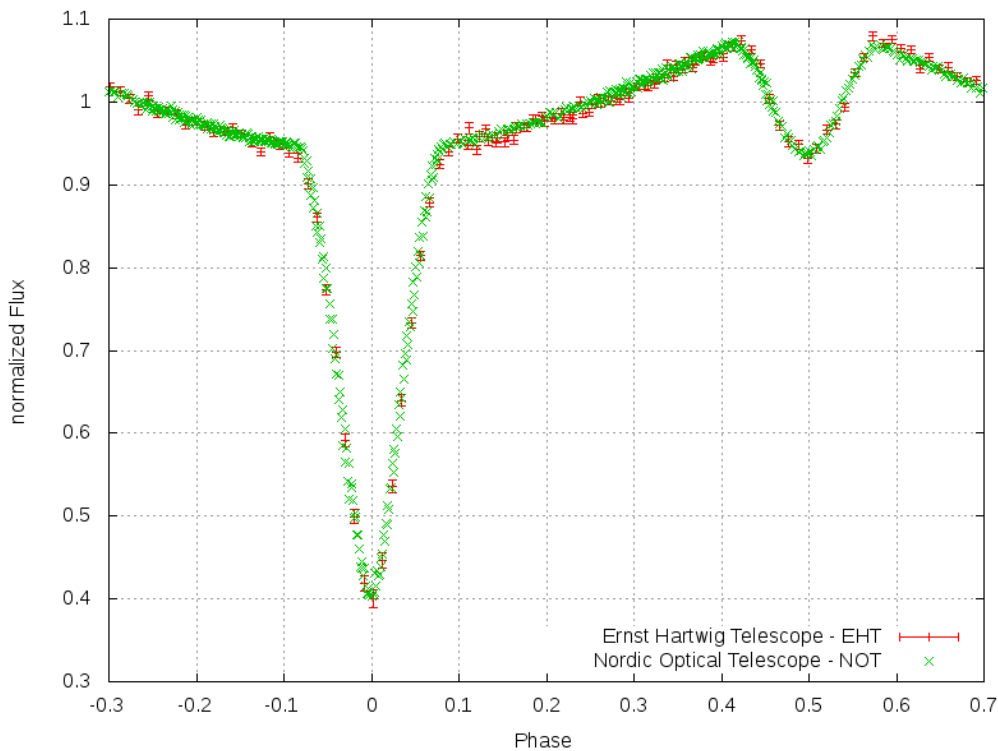
Figure 4.5.: phased and normalized lightcurves of V470 Cam obtained with NOT(green) and EHT(red)

time are drastically reduced due to the larger mirror, but all-in-all the lightcurves show an excellent resemblance. Especially the important depth and shape of the two minima are reproduced exactly. A small scattering of the EHT data after the primary eclipse may be caused by atmospheric distortions that were not entirely corrected by the comparison stars. The problem with the worse time resolution

could be compensated by extending the observation time spent for a single object. As the data need to be phased nevertheless for a lightcurve analysis, data from different nights could be merged to increase the quality of the analysis. For the timing of minima, this is not possible, of course.

As it has been shown, the EHT is able to obtain high quality data and does not have to stand back behind similar telescope systems or even a bit larger telescopes. Therefore the analysis of binary systems has been continued and will go.

4.3.1.3. EHT-Observations and eclipse timing

V470 Cam was observed five times with most datasets covering more than one full orbit. However the very first observation on 31.12.2013 could not be used because of a power outage during the primary eclipse.

The first observations suffered from quite long exposure times without binning, but time after time the exposure time was reduced coming along with greater experience in the photometric measurements and the necessary brightness of the target on the final image. The following figure shows an unphased lightcurve of V470 Cam, covering slightly more than one orbit. Altogether, the following six eclipse times
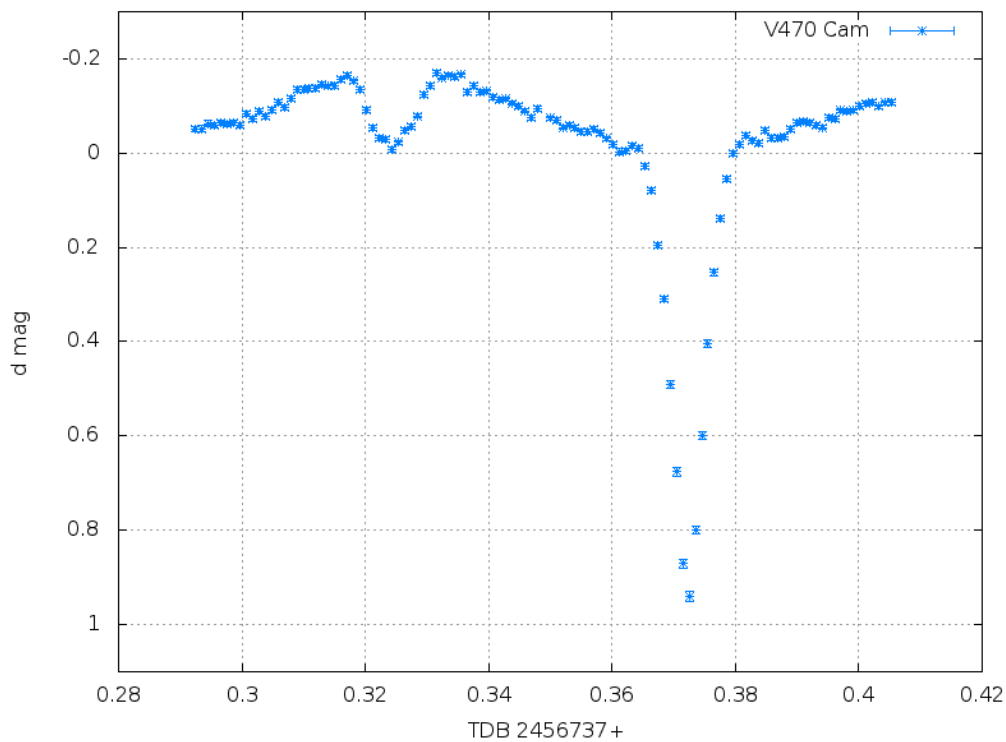
Figure 4.6.: Exemplaric, unphased lightcurve of V470 Cam

could be determined.

$$\text{TCB} = 2456712.312122 \pm 2.96 \cdot 10^{-5}$$

$$\text{TCB} = 2456712.407790 \pm 3.29 \cdot 10^{-5}$$

$$\text{TCB} = 2456712.503441 \pm 6.62 \cdot 10^{-5}$$

48

$$\mathrm{TCB} = 2456726.372817 \pm 3.83 \cdot 10^{-5}$$
$$\mathrm{TCB} = 2456737.372278 \pm 4.31 \cdot 10^{-5}$$
$$\mathrm{TCB} = 2456745.407690 \pm 3.65 \cdot 10^{-5}$$

4.3.1.4. O-C diagram

The comparatively large amount of eclipse timings allows to compute an O-C diagram for V470 Cam.
The first observation of the system wit the EHT was used as a reference point and therefore has an O-C value of 0 s. For the period a value of 0.09564665 d has been used, as provided in Pribulla et al. [2012]. The result can be seen in Figure 4.7. The errors were computed from the errors of the single timings. It is clearly visible that
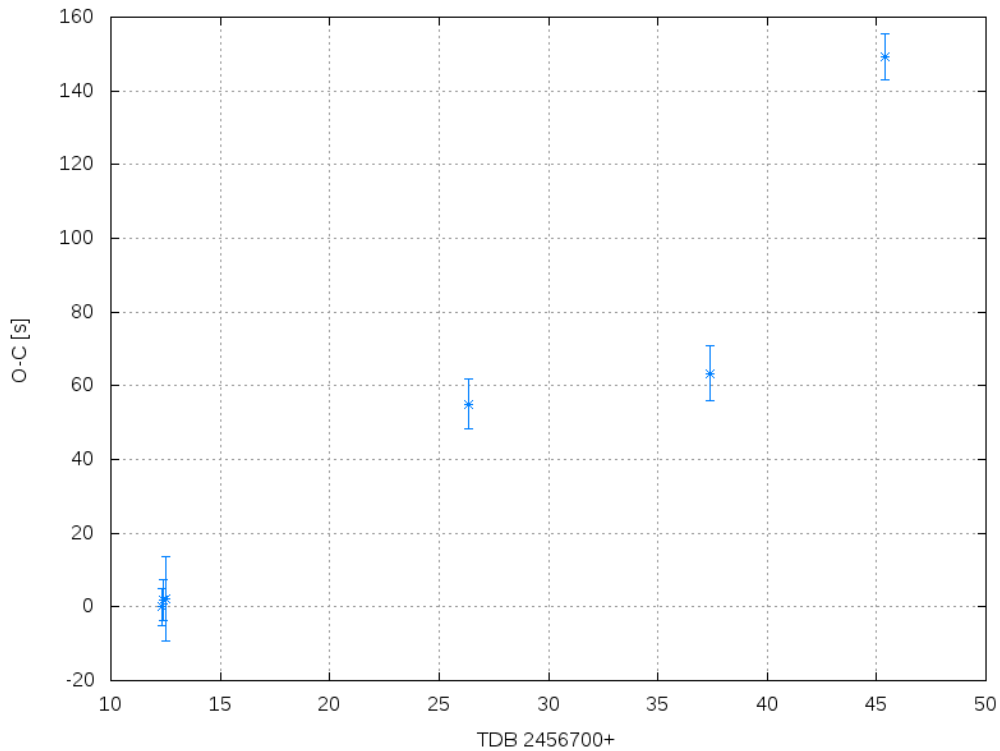
Figure 4.7.: O-C diagram of V470 Cam

the gap between observed and predicted eclipse time has increased dramatically up to more than two minutes. But it has to be mentioned that this increase could also be caused by a slightly inaccurate value for the period. Earlier O-C calculations by Qian et al. [2013] show a sinusoidal variation.
The diagram calculated during this thesis has too few datapoints to present a trustworthy fit, but at least the amplitude of the variations lies within the range presented by Qian et al. [2013].

4.3.2. HW Vir

4.3.2.1. Basic information

HW Vir was the first known sdB/red dwarf system. It was discovered by Menzies and Marang [1986]. Since then, it has been the subject of numerous observations. It has a period of 2.8 h and an average magnitude of $V = 10.0$ mag. The sdB primay has an effective temperature of around $28500°\,K$ and a surface gravity of log g=5.6, as derived from a spectroscopic analysis by Wood and Saffer [1999].

The orbital period changes were examined at first in 1994. Several models have been developed over the years to describe the variations in the O-C diagram. A model by Lee et al. [2009] seemed to describe the period variations correctly, but it failed to predict the latest trend in the data. A new model has been published by Beuermann et al. [2012b] that indicates the presence of two companions. Because of such unpredicted variations it is very important to re-observe those systems from time to time.

4.3.2.2. EHT-Observations and eclipse timing

HW Vir was observed two times with the STX 16803 camera. The system is the brightest one observed for this thesis. Therefore the exposure time could be reduced to 5 s by using the 2×2 binning mode. This leads to an exceptionally high time resolution. As the declination of the system is very low, there was only a short time window during the nights where the star was high enough above the horizon to reduce the atmospheric seeing to a tolerable value. An exemplaric lightcurve of HW Vir and the fitted Gaussian can be seen in Figure 4.8. The second lightcurve of HW Vir didn't
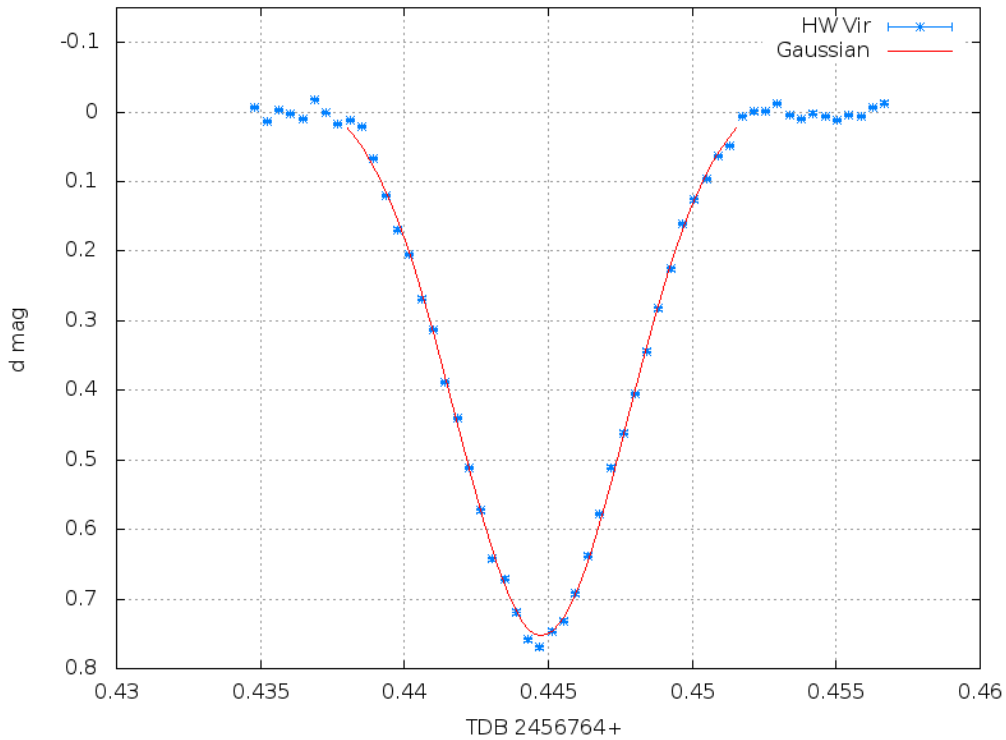
Figure 4.8.: Primary eclipse of HW Vir and applied Gaussian fit

cover a full eclipse, but missed about 50 % of the primary ingress. Nevertheless it was possible to determine the eclipse timing because the fitted Gaussian is a symmetric function that can be set up completely only by one of the edges.

The two eclipse timings are

$$TCB = 245674.444740 \pm 1.745 \cdot 10^{-5}$$

$$TCB = 2456797.434214 \pm 3.091 \cdot 10^{-5}$$

4.3.3. NY Vir

4.3.3.1. Basic information

NY Vir is an eclipsing binary system of HW Vir type. It consists of an sdB + M star and shows a prominent reflection effect. It has an orbital period of 2.42 h and an average magnitude of $V = 13.3$ mag. NY Vir takes a special role among the other systems, as the sdB primary displays short pulsations.

In the latest publications on this system, Qian et al. [2012] showed that the discovered changes in the O-C diagram can be caused by a planet orbiting the system. A continuous decrease of the period might be part of a cyclic variation. This would be an indicator for a fourth object in the system. Further observations are required to confirm this hypothesis.

4.3.3.2. EHT-Observations and eclipse timing

NY Vir was observed three times in April and Mai. Again, the cameras were operated in the binning mode to reduce the necessary exposure time. It was possible to get lightcurves during three primary eclipses, resulting in the following eclipse timings.

$$TCB = 2456768.387636 \pm 2.334 \cdot 10^{-5}$$

$$TCB = 2456797.480147 \pm 7.355 \cdot 10^{-5}$$

$$TCB = 2456802.430139 \pm 2.342 \cdot 10^{-5}$$

Figure 4.9 shows an exemplaric lightcurve. Especially after the primary eclipse there are fluctuations visible. The period of these fluctuations matches the period of the pulsations of NY Vir.

The following image shows a high resolution ULTRACAM/VLT lightcurve of NY Vir, taken from Vučković et al. [2007]. The pulsations can be clearly seen throughout the orbit. Only during the primary eclipse hardly any variations are observable, as the pulsating sdB is covered by its companion.

NY Vir was the only pulsating sdB that was observed during this thesis.
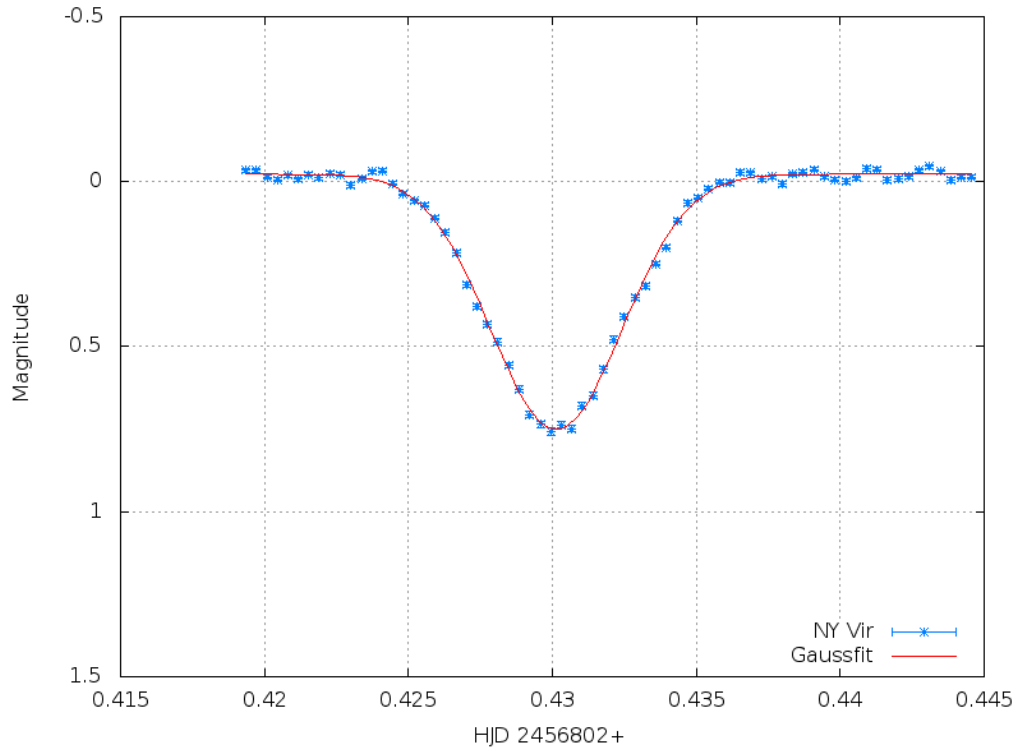
Figure 4.9.: Primary eclipse of NY Vir and applied Gaussian fit
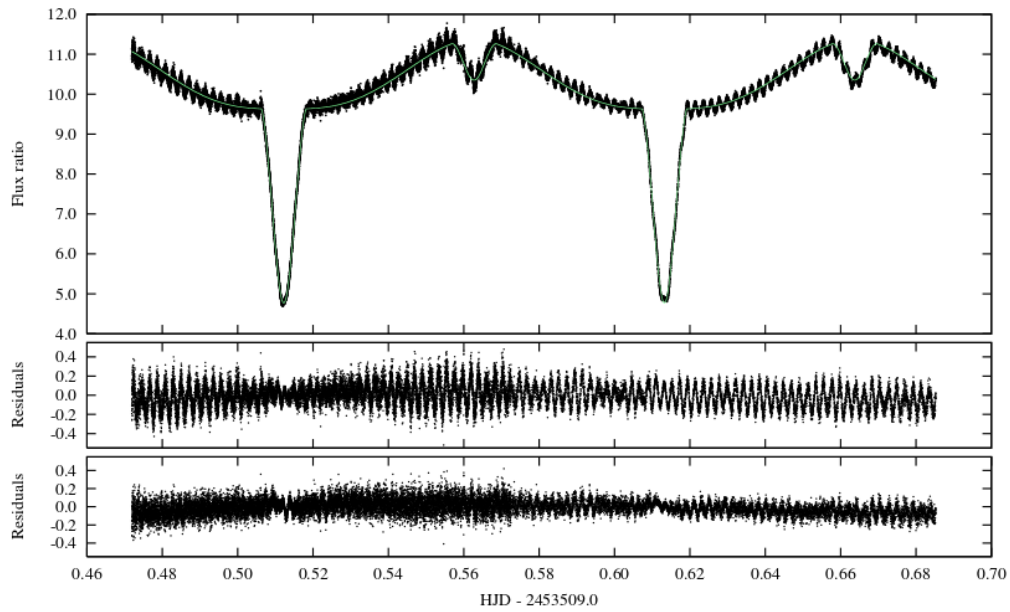
Figure 4.10.: ULTRACAM/VLT lightcurve of NY Vir, *middle panel:* Residuals before subtracting the pulsations, *bottom panel:* residuals after subtraction of the four strongest oscillation modes, taken from[1]

---

[1]Vučković et al. [2007]

4.3.4. DE CVn

4.3.4.1. Basic information

DE CVn is a relatively bright ($V = 12.9\,\mathrm{mag}$) eclipsing system that consists of a white dwarf primary and a red dwarf companion. Therefore the depth of the eclipses is color-dependent. It was first discovered by ROSAT as an X-ray source. The latest analysis was carried out by Parsons et al. [2010]. They focused their analysis on the primary eclipse and combined older ULTRACAM data with more recent observations. As there are only a few reliable points in the O-C diagrams so far, a search for period variations will not be fruitful yet.

4.3.4.2. EHT-Observations and eclipse timing

DE CVn was only observed once, due to the bad weather and the presence of other high priority targets. The observations took place on 03/29/2014.
Because of its long period, it was decided to obtain only data from the primary eclipse. Figure 4.11 shows the visualization derived from the photometric measurements. Because of the rectangular shape, it was not possible to fit a Gaussian to the
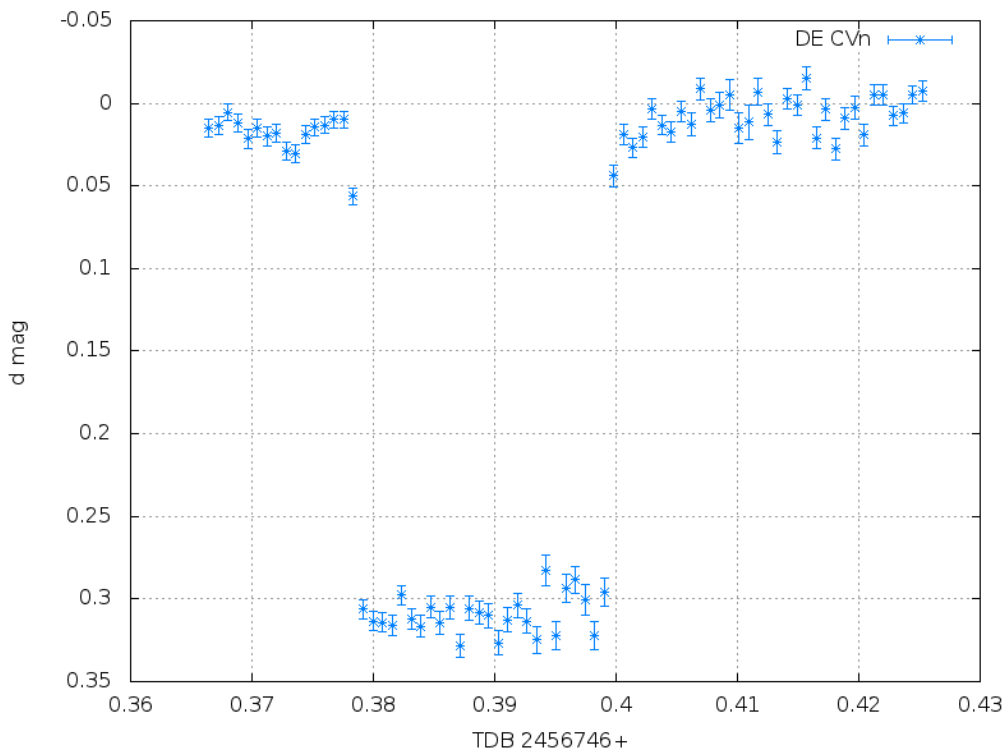
Figure 4.11.: Primary eclipse of DE CVn

eclipse. Therefore it was necessary to obtain the mid-point of the eclipse in another way.
The timing of the first and the last point in the bottom of the eclipse was used to calculate the length of the eclipse. Half of this time was added to the first bottom point of the eclipse. The same procedure was repeated for the first and the last data point right before/after the eclipse. This resulted in two slightly different mid-point

times. The average of both was calculated to

$$TCB = 2456746.3890905 \pm 5.0 \cdot 10^{-5}$$

The error of 4.32 s was estimated from the experiences of other eclipse timings.

4.3.5. DP Leo

4.3.5.1. Basic information

DP Leo is an eclipsing binary system that consists of an white and a red dwarf. It has a very short orbital period of ~ 1.5 h and was discovered back in 1985 as a source of x-rays [Biermann et al., 1985]. The period is among the shortest ever discovered for cataclismic variables. It's apparent magnitude ranges from 17.5 to 19.0, making it quite hard to observe for smaller telescopes. It is known to host at least one exoplanet which is assumed to be a large Jupiter like planet with about 6.4 times the mass of Jupiter [Beuermann et al., 2011]. The O-C curve shows a periodic variation on a timescale of roughly 24 years.

4.3.5.2. EHT-Observations and eclipse timing

Because of the faintness of the system, the observations of DP Leo can be regarded as a test to determine the limits of the EHT.
The photometric data were collected with the STL 11000M and a blue filter. An exposure time of 300 s didn't reveal any sign of the object at full resolution. By applying the 2×2 Binning it was possible to identify the target as a faint signal.
Figure 4.12 shows the resulting lightcurve. One full orbit is covered. Because of the poor timing resolution and the short period of the system, it was only possible to get one datapoint during the primary eclipse. Therefore it is not really suitable to determine the time of the minima of the eclipse. However the reflection effect of the system is clearly visible and the errors are surprisingly small considering the magnitude of the system.
The timing of the one datapoint in the minimum is

$$2456737.445869 \pm 5.0 \cdot 10^{-4}$$

The error was not calculated from a fitted function but estimated.
As the STX 16803 camera has a higher sensitivity than the older model, it would be interesting to observe the system again and check if the time resolution could be improved. As the position of DP Leo didn't allow any observations with the new camera so far, this task has to be postponed beyond the end of this thesis.

4.3.6. GK Vir

4.3.6.1. Basic information

GK Vir is a relatively unstudied system. It was discovered in 1978 by Green et al. [1978]. The latest publication on this system is from Parsons et al. [2012].
It consist of a hot white dwarf primary and a low-mass secondary. Its faintness (V=17.0) and the long orbital period of more than 8 h make it quite hard to observe.
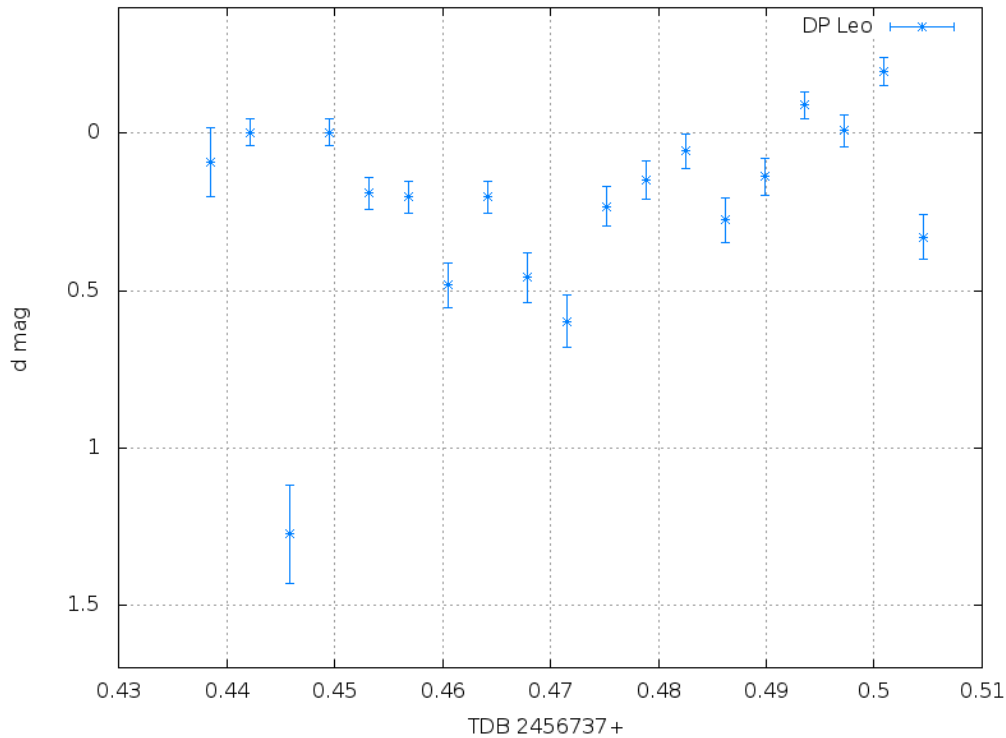
Figure 4.12.: Lightcurve of DP Leo, note that the eclipse is detected at
TDN ~ 2456737.445, te remaining variations are due to the reflection
effect.

The lightcurve hardly shows any sign of a reflection effect.
Parsons et al. [2010] detected small period variations in the O-C diagram. But as there are no datapoints available for the time between 1978 and 2002, no sound statement could be made on possible long-term variations in the system. Therefore it is crucial that this system is re-observed.

4.3.6.2. EHT-Observations and eclipse timing

GK Vir was observed two times with a blue filter and 2×2 Binning. Exposure times were set to 170 s. The long period didn't allow for more observations because the available night time was very short during the summer months. As the observable blue flux of the system is zero during the main eclipse, the datapoints displayed in Figure 4.13 must be seen as upper limits only. It is questionable if the errors given by APT are correct in this special case. It is more likely that they have been underestimated, too. In Figure 4.14 the primary eclipse of GK Vir can be seen. The graph is taken from Parsons et al. [2010] and shows that the flux in the blue band descends to zero during the primary eclipse. To determine the eclipse timing, the same method as with DE CVn was used. As the time resolution is worse and there are fewer datapoints during the primary eclipse, the errors were estimated to

---

[1]Parsons et al. [2010]
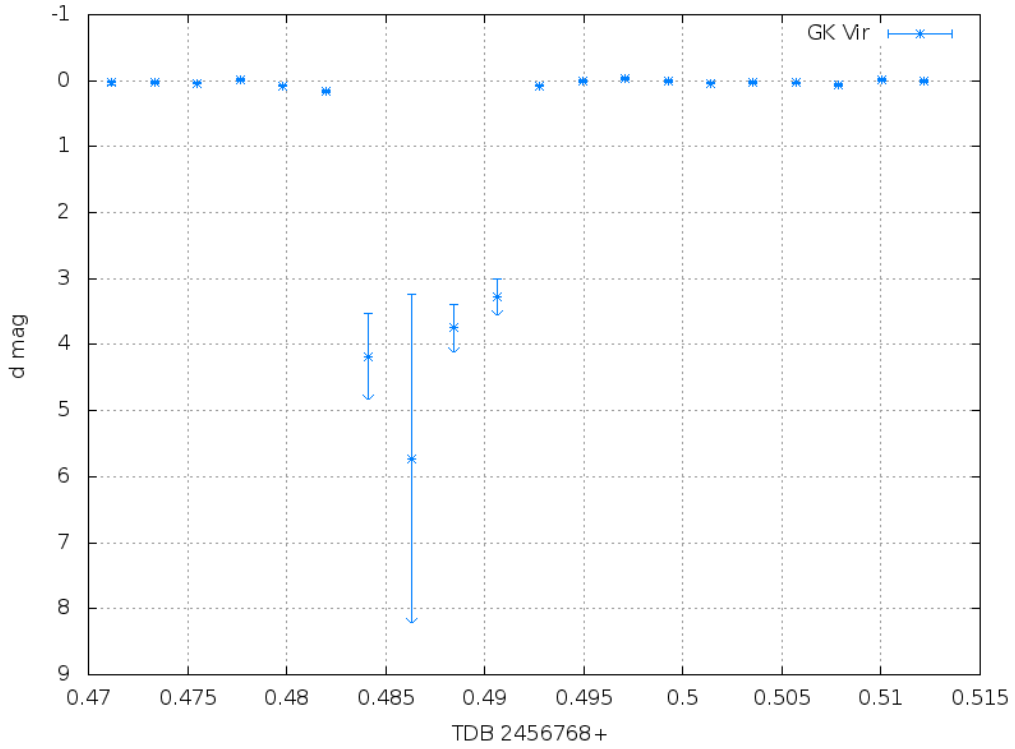
Figure 4.13.: Exemplaric lightcurve of GK Vir, upper limits are indicated as arrows
pointing downwards
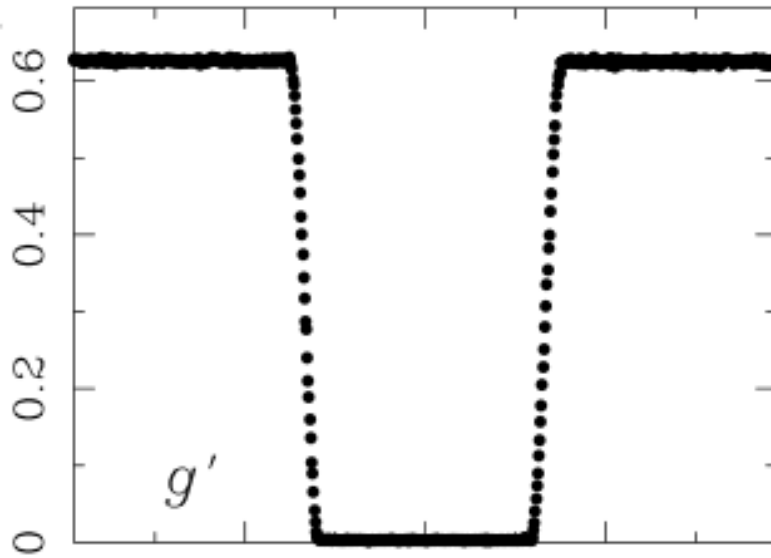
Figure 4.14.: Primary eclipse of GK Vir in the g' band, on the y-axis the flux is
shown, while the x-axis represents a part of the phase, taken from[1]

be somewhat larger. Timings of

$$2456768.4873638 \pm 6.0 \cdot 10^{-5}$$

and
$$2456797.410905 \pm 6.0 \cdot 10^{-5}$$
were found.

As in the case of DP Leo, the data were taken with the STL11000M camera. Because the system has not been observed by larger telescopes for some years, an ongoing examination with the EHT and the new camera is planned. As the time resolution should increase because of the higher sensitivity of the KAI 16803 chip, the timing errors will be reduced.

Nevertheless the results achieved on this system so far are another indicator for the high-performance ability of the EHT. Figure 4.13 shows that the the brightness of the system decreased for more than $4\,\mathrm{mag}$ and and is therefor settled at around $21\,\mathrm{mag}$ in total. Of course, the measured values are only upper limits and the accuracy at these brightnesses is everything but overwhelming but for a telescope with a diameter of only $0.5\,\mathrm{m}$ the achieved results are very respectable.

5. Search for eclipsing MUCHFUSS binaries

5.1. MUCHFUSS project

Despite the determination of eclipse timing, another project was carried out with the EHT. In collaboration with T.Kupfer (Nijmegen), efforts were undertaken to search for eclipses or light variations in binary systems discovered by the MUCHFUSS project. The name stands for Massive Unseen Companion to Hot Faint Underluminous Stars from SDSS.

It aims at finding massive companions to hot subdwarf stars. These systems are predicted to make up to 3% of all close sdB binaries [Geier et al., 2010]. Massive companions can be neutron stars, stellar mass black holes or heavy white dwarfs with masses slightly below the Chandrasekar limit.

Hot sdB stars were selected from the SDSS database by visual inspection of their spectra and constraints on the color. If any high radial velocities were found, the objects were selected for spectroscopic follow up observations to obtain a radial velocity curve. The target selection is e.g. discussed in Geier et al. [2012]

From observations of single lined spectra and the following determination of a minimum mass of the companion, candidate systems with massive companions can be found. Target selection focuses on short period systems with low RV variations or systems with longer periods and a higher RV variations instead.

MUCHFUSS has discovered short period sdB binaries with low mass companions, including brown dwarfs as well. The following image shows the lightcurve of such a system, SDSSJ162256.66+473051.1, consisting of an sdB and a brown dwarf. It was taken from Schaffenroth et al. [2014]. A photometric observation of such systems allows to pin down the parameters of the objects.

Unfortunately it was only possible to observe one target for this project, as most of the available observing time was used for the eclipse timing. The follow-up observation is presented in the following section.

5.2. UVEXJ212257

UVEXJ212257+552609 was observed in the course of the MUCHFUSS project. The system showed variations of its radial velocity and was therefore selected for further observations. It was the first system for which photometric data was collected with the EHT. The follow up observations with the EHT should check if the system is eclipsing or showed other light variations caused by the reflection effect or ellipsoidal variations. The system was observed only once for about 3 hours. As the EHT was brand new at that time and not fully optimized, the exposure time was not reduced to the lowest possible level and set to 300 s without binning. Several gaps
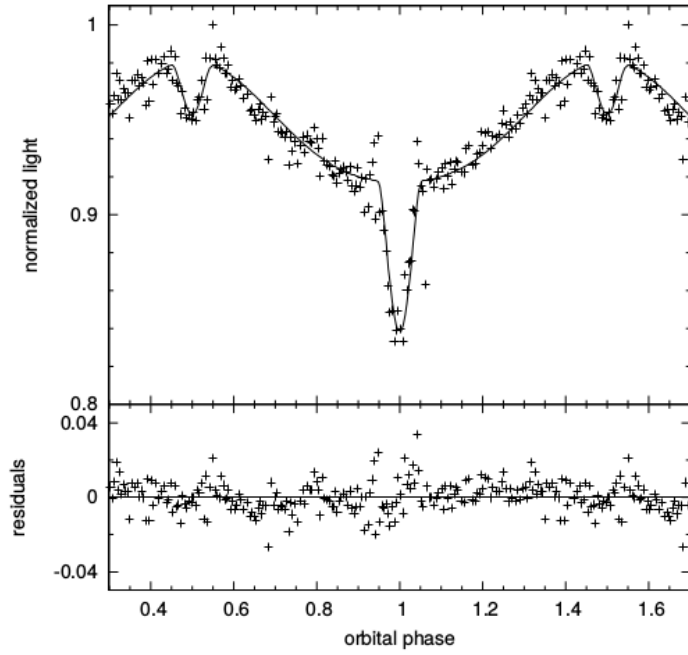
Figure 5.1.: Phased BUSCA lightcurve in B_B of J1622. The solid line demonstrates the best-fitting model. In the bottom panel the residuals can be seen.
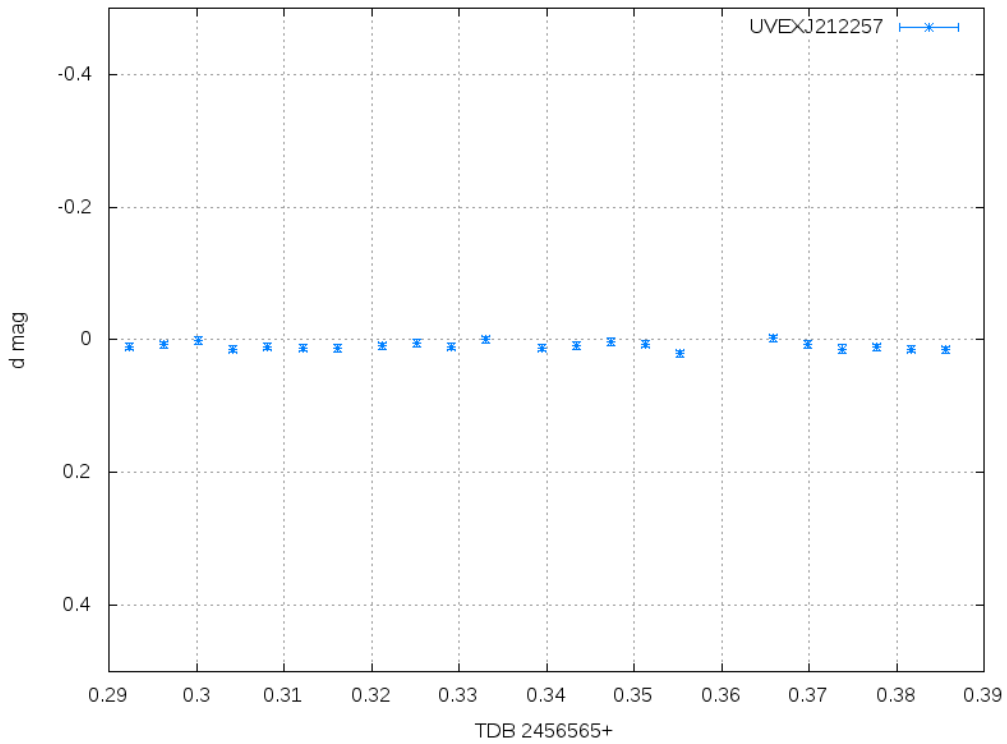
Figure 5.2.: Lightcurve of UVEXJ212257

in the lightcurve displayed in Figure 5.2 were caused by a necessary meridian flip during the observations and the turning of the dome as well as an error concerning

the USB connection of camera and computer. (Meanwhile sufficient experience has been gained so that the whole procedure can be completed within one minute).

The lightcurve does not show any variations with an amplitude larger than $\pm 0.03\,\text{mag}$ on a timescale of several hours. Smaller variations would not be detectable with the EHT. An other follow up observation run in Nijmegen by T.Kupfer several nights later revealed no brightness fluctuations either. It is unknown whether other photometric observations of UVEXJ212257 exist.

The search for eclipsing binaries in the MUCHFUSS database was also the motivation for an observational campaign, the MAPLE project as a successor for the eclipse timing observations. The new project is explained in Chapter 7.

6. PTF 072456

This chapter will be submitted for publication in Astronomy & Astrophysics as

A new HW Vir binary from the Palomar Transient Factory
PTFJ072456+125301 - An eclipsing subdwarf B binary with an M-star companion

by Schindewolf et al.

In the previous chapter, it was shown that the new Ernst-Hartwig-Telescope in Bamberg is capable of providing accurate lightcurves, that are suitable for eclipse timing.

However, the majority of astronomical research is still done with large telescopes with a diameter exceeding one meter. Some of those telescopes are used in surveys, to gather data from a large sky area. One example is the Palomar Transient Factory (PTF hereafter). The PTF is a wide field survey that searches for variable sources and optical transients. It makes use of the 1.2 m Oschin Telescope at Palomar Observatory, equiped with eleven 12k × 8k CCD Camera, and the Palomar 60" telescope [Law et al., 2009]. With each exposure 7.2 square-degrees are covered. In a typical night up to 200 square-degrees are observed [Levitan et al., 2011].

In the context of this survey, a new candidate for a HW Vir system has been discovered at 07:24:56 +12:53:01 and additional spectroscopic observations have been undertaken.

In the next section, the observations and the data reduction is described. Afterwards, the results of the spectroscopic and photometric analysis are presented. The subsequent calculations of the proper motion and kinematics of the system are followed by a discussion of the binary's evolutionary status. The chapter ends with a brief summary of important system parameters and an outlook on future investigations.

6.1. Observations

All data were provided and reduced by colleagues, working at Caltech for the Palomar Transient Factory.

6.1.1. Spectroscopy

The spectra of PTF1J072456+125301 (PTF0724 hereafter) were taken at the Palomar 200" telescope with the Double Spectrograph DBSP using a low resolution (R∼ 1500). The observation took place on August 10, 2010. Thirtyeight spectra were collected, covering a range fom 3000 Å to 11000 Å. The reduction of the spectra was done using the Molly package by Tom Marsh [1].

---

[1] `http://www2.warwick.ac.uk/fac/sci/physics/research/astro/people/marsh/software`

6.1.2. Photometry

Seven lightcurves were examined, almost each covering a full orbit. For all observations a SLOAN g' filter was used and the time span between the lightcurves were usually only a few nights. Each lightcurve consisted of about 150 datapoints. The data were reduced as describend in Levitan et al. [2011]. The section on the photometric reduction is copied from this paper.

„[The images] were de-biased and flat-fielded using the P60 pipeline [Cenko et al., 2006]. The *SEXTRACTOR* package [Bertin and Arnouts, 1996] was used to identify sources in each exposure and their instrumental magnitudes were obtained using optimal point-spread function photometry, [Naylor, 1998] as implemented in the *STARLINK* package *AUTOPHOTOM*[1]. Lightcurves were calculated using a matrix-based, least squares minimization, relative photometry algorithm. The primary goal of any such algorithm is to minimize noise, typically by assuming that certain stars in the field are non-variable and identifying an optimal zero point for each exposure. We expanded on this to simultaneously solve for both zero point and additional de-trending terms as correction for airmass and instrumental changes. The algorithm is similar to that developed in Honeycutt [1992] and is describend in the Appendix of Ofek et al. [2011].

To accomplish the de-trending, we modeled each observation as

$$m_{i,j} = \bar{M}_j + Z_i + \alpha c_j A_i + \sum_{k=1}^{n_k} \beta_k c_j \tag{6.1}$$

where the data needed are the following:

1. $m_{i,j}$: the magnitude of source j on exposure i

2. c_j: a color for each source. The color is required to compensate for stronger effects of airmass in blue stars as well as the differences in CCD efficiency over a range of wavelengths

3. A_i: the airmass of each exposure

The terms to be fitted are the following.

1. Z_i the optimal zero-point term of each exposure

2. $\bar{M}_j$: the mean magnitude term of the source

3. α: the airmass calibration coefficient for all exposures and sources

4. β_k: the kth telescope/instrument calibration coefficient, for $k = 1, 2, \ldots, n_k$ where n_k is the number of telescopes. This term is introduced to take into account the different response of each telescope/instrument. For lightcurves with data from only one instrument (as in our case), these terms were not used.

It is important to ensure that all stars used for the solution are not variable. We restricted the stars used to those found in 80%-100% of all exposures, depending

---

[1]http://www.starlink.ac.uk/docs/odot45.htx/node33.html

on the lightcurve, and iteratively removed any sources with high residuals. Since the solution is not unique unless reference magnitudes are provided, we used blue magnitudes from USNO-B 1.0.

The rms errors used for the analysis are based on the median scatter of other stars with similar magnitude present in at least 50% of observations. " [Levitan et al., 2011]

However, only six of the seven lightcurves were used for the photometric analysis, as one of them was too noisy.

The PTF lightcurves show a reflection effect and grazing eclipses (see Figure 6.3). The primary minimum is quite deep, with the flux descending to about 25% of the flux at phase 0.25 (being normalized to 1, see Figure 6.3). The ephemeris was determined by fitting parabolas to the core of the primary eclipses. The period could be easily derived because several lightcurves covered more than one full orbit, containing two primary minima.

The ephemeris of the primary minimum is given by:

$$HJD = 2455295.64113(8) + 0.09976(84)$$

6.2. Spectroscopic analysis

6.2.1. Radial velocity curve

The first part of our analysis was the determination of the radial velocity (RV) curve. Since the system is single-lined, the analysis is straight forward. We made use of SPAS (see Section 2.2.1) to determine the radial velocity for each spectrum. A combination of Gaussians, Lorentzians and polynomials was fitted to the Balmer and helium lines visible in the spectra (see Table .3 in the Appendix).

Because the phase shift between the primary and secondary minima is 0.5, the orbit of PTF0724 must be circular (Figure 6.3). Therefore we fitted a sine curve to the RVs, using the period we gained from the photometric analysis. However, small eccentricities cannot be completely excluded. Figure 6.1 shows the phased RV curve with the best-fit solution. All phases of the orbit are well covered. We derived a semiamplitude of K $= 101.25 \pm 3.2$km s^{-1} and a system velocity of $\gamma = -25.69 \pm 2.44$ km s^{-1}. The period derived from the sinusoidal fit (P$= 0.0985$ d) is consistent (within the errormargins) with the period derived from photometry (P$=0.0997$ d). The mass function is found to be

$$f(m) = \frac{PK^3}{2\pi G} = \frac{M_2^3 \sin^3 i}{(M_1 + M_2)^2} = 0.0108 \, M_\odot \tag{6.2}$$

6.2.2. Atmospheric parameters

Due to the poor signal-to-noise ratio of the individual spectra, we had to shift and coadd the single velocity-corrected spectra to improve the S/N ratio and to be able to derive the atmospheric parameters with reasonable precision.

Effective temperature, surface gravity and helium abundance were determined by fitting synthetic spectra to the Balmer and helium lines of the coaded spectra. The
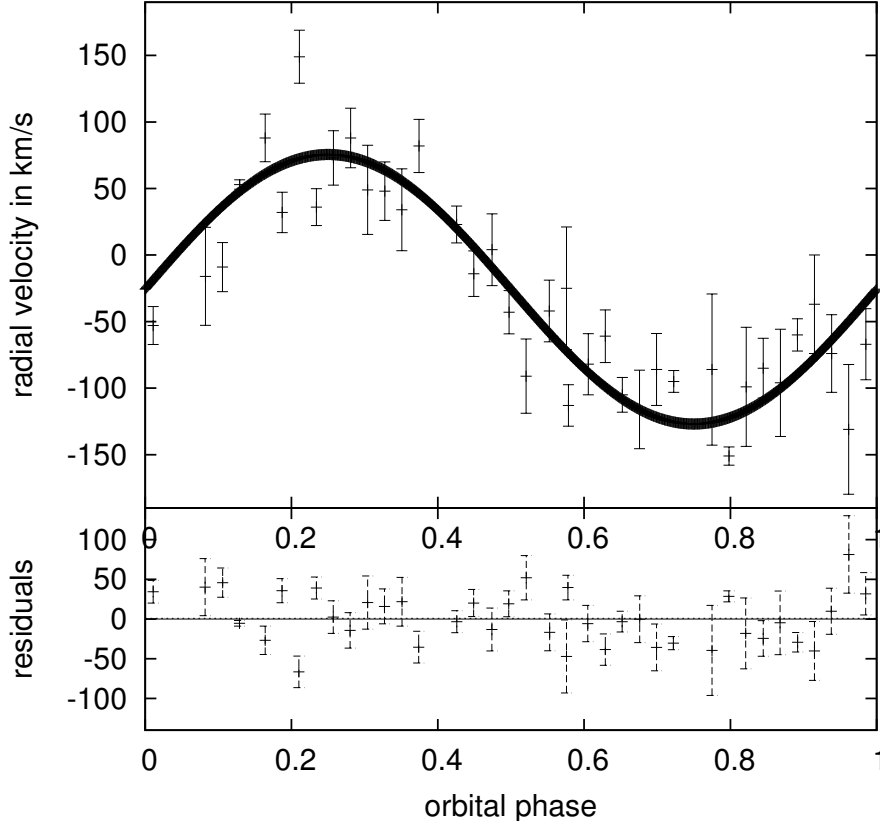
Figure 6.1.: Radial velocity plotted against orbital phase of PTF0724. In the bottom panel the residuals can be seen.

synthetic spectra were calculated by using LTE model atmospheres with solar metallicity and metal line blanketing by Heber et al. [2000]. The derived parameters are: $T_{eff} = 33900 \pm 350\,K$, log g $= 5.74 \pm 0.08$ and log y $= -2.02 \pm 0.07$.

The inclination of the orbit is well constrained by photometry ($i = 83.5°$, see Section 6.3). Adopting the canonical mass for the sdB we find a mass ratio of q=0.33 by making use of the mass function.

In Figure 6.2 the position of PTF0724 in a (T_{eff}, log g) diagram is compared to other sdBs in close binary systems with known periods (see Maxted et al. [2002]). Furthermore the graph contains the position of the Extreme Horizontal Branch (Zero Age- and Terminal Age-) and tracks for EHB and post EHB evolution for different masses of the primary sdB by Dorman et al. [1993].

Its position in the graph indicates that PTF0724 seems to be a normal, evolved sdB close to core helium exhaustion. Similar systems lie in the same regime.

6.3. Lightcurve analysis

The seven lightcurves were phased, normalized and merged to one lightcurve, see Figure 6.3. Small scattering of the datapoints, mainly before and after the primary eclipse, remained. We could not identify a certain single lightcurve as being respon-
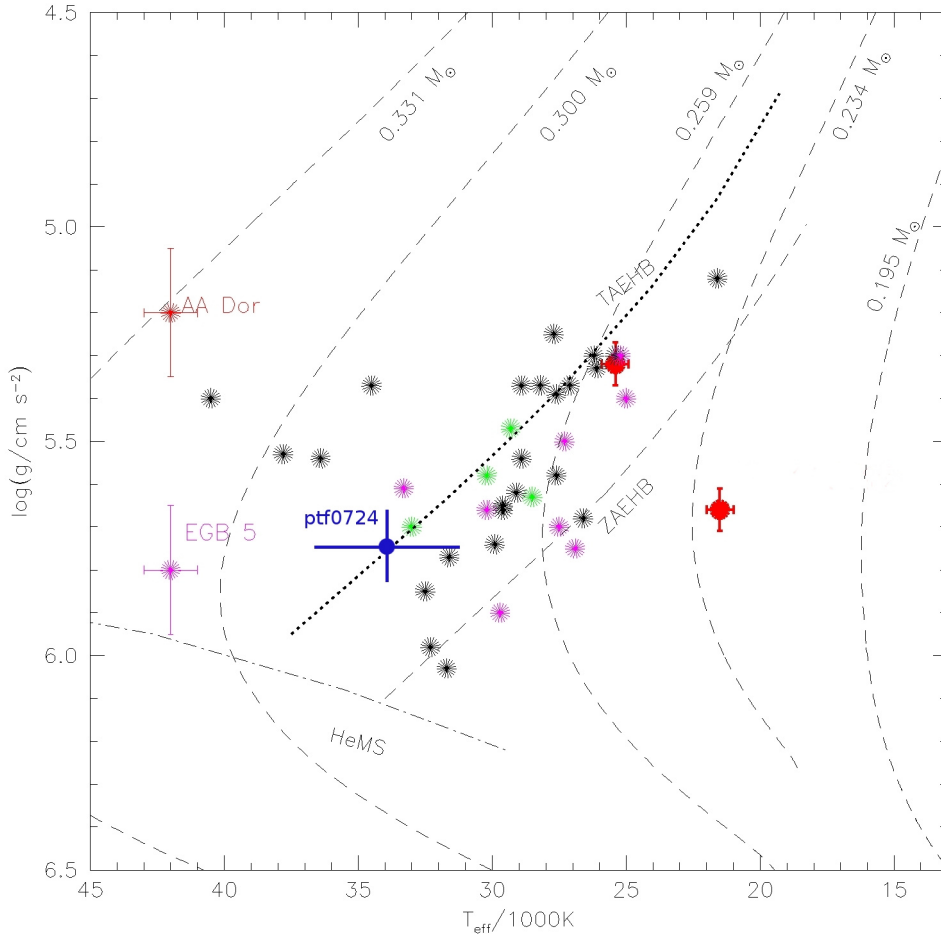
Figure 6.2.: Position of PTF0724 in a (T_{eff}, log g) diagram in comparison to other known sdB stars in close binary systems with known periods [Maxted et al., 2002] and models for post RGB evolution by Driebe et al. [1998]. Adopted from Heber et al. (2003). In addition the Zero- and Terminal Age Horizontal Branch are shown.

sible for this effect.

The analysis was performed by using the MORO (MOdified ROche Program, see Drechsel et al. 1995). The effective temperature and the surface gravity of the primary component was derived from the spectroscopic analysis (see Section 6.2.2). Because of its early spectral type, the gravity darkening exponent can be fixed at $g_1 = 1$, as one would expect for radiative outer envelopes [von Zeipel, 1924]. For the companion, we used $g_2 = 0.32$ [Lucy, 1967]. The linear limb darkening coefficients for the primary were interpolated from the table of Wade and Rucinski [1985] and fixed at $x_1 = 0.190$. The radiation pressure parameter [Drechsel et al., 1995] of the secondary was set to zero because of the low temperature of the secondary star. That means that the effects of the radiation pressure of the shape on this star is negligible. All results obtained with different sets of parameters resulted in negligible third light. Hence there is no evidence for a third body in the system, and l_3 was set to zero.

To be sure that a specific set of parameters is a global solution and not only a lo-

cal one, a multitude of different start parameters was chosen. The mass ratio was varied from 0.3 to 0.5 and the start values for A_2, Ω_1 and Ω_2 were changed. All in all, roughly 28000 different parameter sets were calculated. This was only possible by using the computation power of the Remeis Computer Cluster.

To estimate the quality of the lightcurve fit, the sum of the squared residuals of all points to the synthetic lightcurve is calculated. The solution with the smallest sum is supposed to be best. Unfortunately the difference between several solutions for different mass ratios turned out to be very small. Therefore a unique solution could no be determined. It turned out that the best solutions grouped around a mass ratio of q = 0.435. This is significantly different from the mass ratio we derived from the mass function under the assumption of an sdB having the canonical mass of $0.47\,M_\odot$ ($q_{\mathrm{mass}} = 0.33$). Therefore the search was limited to a mass ratio in the range from $q = 0.31$ to $q = 0.35$ and tried a larger number of different parameter sets for each mass ratio. It was found, that there is a solution for q=0.33 that reproduces the lightcurve quite well. The standard deviation sigma (indication for the quality of the fit) of this parameter set is among the best 2 % of alls sigmas and the $\Delta\chi^2$ of the two fits indicates that the difference between both is only slightly above 1σ. Sigma is defined as

$$\sigma_{\mathrm{fit}}(x) = \sqrt{\frac{n}{n-m}\frac{1}{\sum_{\nu=1}^{n}}\sum_{\nu=1}^{n}\omega_\nu d_\nu^2(x)} \tag{6.3}$$

d_ν are the residuals, the difference between observational data and the calculated model and ω_ν is a weight that can be used to increasingly consider several data points, e.g. the bottom of the primary eclipse, m is the number of start parameters for the simplex algorithm.

The solution of the light and RV curves provides us with empirical mass-radius relations for the sdB as well as for its companion, while surface gravity of the sdB provides an independent one for the primary (see Figure 6.4). The empricial mass-radius relation matches predictions for low mass main sequence stars very well. Figure6.4 shows the relation for the sdB and Figure 6.5 for the companion. Both solutions could reproduce the shape of the lightcurve very well. Especially the important ingress and egress are reproduced perfectly (see Figure 6.3). The lightcurves and residuals for both solutions look exactly the same, for the naked eye. Therefore only the solution and residuals for $q = 0.33$ are shown in Figure 6.3.
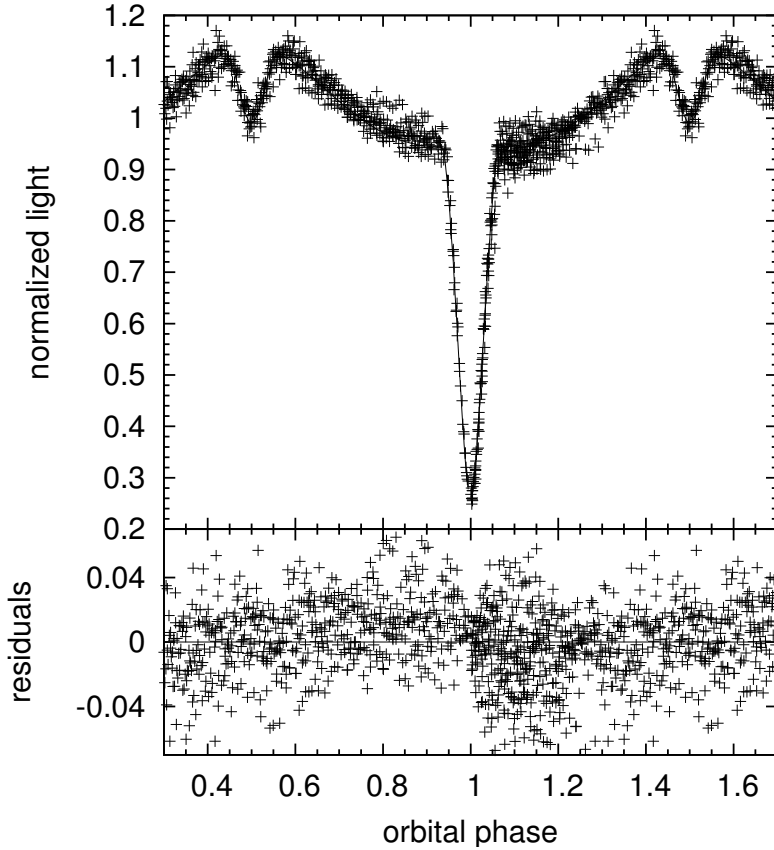
Figure 6.3.: Phased lightcurve of PTF0724 for q=0.33. The solid line demonstrates the best fitting model. In the bottom panel the residuals can be seen.

As the reduced χ^2 for each solution is well above 1, the question arises if the errors in the photometric measurements are underestimated. If so, this could be a hint for unresolved pulsations superposed on the eclipse curve.

Both solutions show an albedo for the companion that exceeds 1 (A_2=1.8). No reasonable fits for lower values of A_2 were found. As only lightcurves taken with the SLOAN g' filter were used for the analysis, the value is not thrustworthy anyway. To determine if the computed value corresponds to the real properties of the star, lightcurves taken in other wavelengths are required.
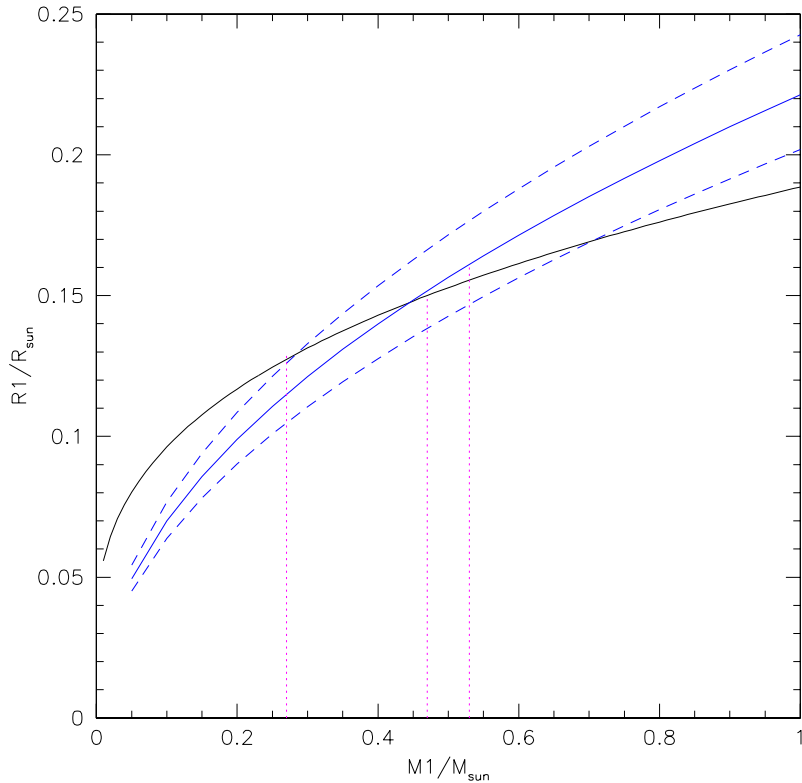
Figure 6.4.: Comparison of the sdB mass-radius relation from the analysis of the lightcurve to those derived from different gravities and resulting sdB masses of $0.27\,M_\odot$, $0.526\,M_\odot$ and the canonical mass of $0.47\,M_\odot$. Provided by U.Heber

Regarding the sdB mass-radius relation, it can be seen that all solutions lie within the expected range calculated from theoretical models, with the solution for $M_{sdB} = 0.27\,M_\odot$ just slightly outside the error margins. The same applies for the companion, which is a M-dwarf star due to its low mass and the low temperature determined from the analysis.

However we are unable to decide which of the solutions is correct. Therefore, both will be discussed in Section 6.5.

The tables at the end of this section, give a summary of all parameters derived from the analysis of the lightcurve.

6.4. Proper motion & kinematics

An analysis of the proper motion and the kinematics of PTF0724 was conducted, but the quality of the results was quite poor as they suffered from very large errors. Therefore it is not shown here, but can be found in Section G in the Appendix.

6.5. Evolutionary status

To discuss the evolutionary status of PTF0724 it is helpful to compare its parameters to those of other known systems.
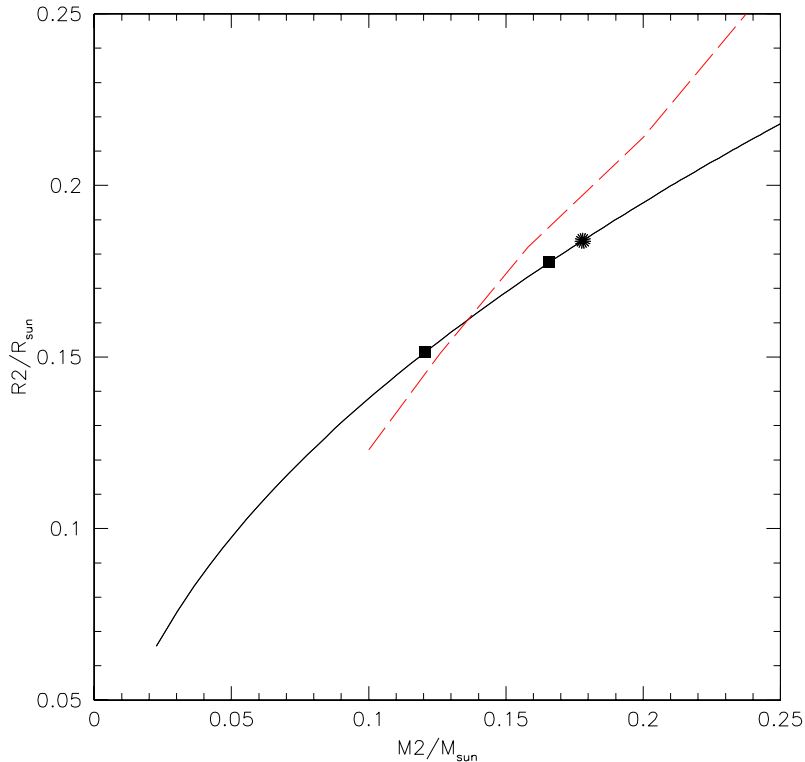
Figure 6.5.: Comparison of the companions mass-radius relation derived from the analysis of the lightcurve to relations for M-type dwarfs (dashed: theoretical predictions from Baraffe and Chabrier [1996]). Filled circle: sdB has canonical mass $(0.47\,M_\odot)$; hash key: sdB masses for lightcurve solutions. Provided by U.Heber

Depending on the mass of the sdB star, two different evolutionary tracks are possible, the post-RGB and the EHB scenario (see Section 2.3.1).

6.5.1. post-RGB scenario

If one focuses on the low mass sdB, the post-RGB scenario is most probable: We assume that PTF0724 has lost most of its hydrogen envelope in the common envelope phase. The remaining He core does not exceed the canonical mass that is necessary to ignite helium (helium flash). Therefore the star can be classified as a pre helium white dwarf that cools down to become a He white dwarf. Presently, the star contracts, therefore its temperature and gravity should increase with time. Afterwards it will move to the cooling sequence.

The short period of the system suggests it to be in a post common envelope stage.

6.5.2. EHB scenario

If we assume the (almost) canonical mass solution to be correct, another evolutionary status becomes realistic.

In this case, the remaining helium core is massive enough to sustain helium burning,

it is an EHB star, like most of the other known sdBs. This means that the sdB would evolve to higher temperature and lower log g. It is most likely that it has been formed in the common envelope channel due to its short period. The conclusions for the companion star remain valid.

If we compare the lifetime of the different evolutionary stages, it can be recognized that the pre He WD stage would only last for several million years, while the core helium burning sdB can remain much longer in its actual state.

By taking into account that it is much more likely to find a sdB with a mass around the canonical one than a very lightweight one, we prefer the mass ratio of $q = 0.33$ implicating a sdB mass of $0.526 \pm 0.05 M_{\odot}$. It is important to remember that it is not possible to finally exclude one or the other solution based on the available data, but the most plausible assumption is that it is a normal EHB star.

6.6. Conclusion

The star PTF1J072456+125301 was found to be an eclipsing binary with an orbital period of 0.09977 d. We performed a spectroscopic and photometric analysis to pin down the system parameters and investigate its state of evolution.

The analysis of the light curve revealed a mass ratio of q = 0.33, resulting in an sdB mass of $0.56 \pm 0.05 M_{\odot}$ which is close to the canocial mass for a star of that type. Its effective temperature $T_{\mathrm{eff}} = 33900 \pm 350 \, \mathrm{K}$ and the surface gravity of about $\log g = 5.7$ are located in a regime slightly above the Extreme Horizontal Branch.

The companion has a mass of $0.174 \pm 0.016 M_{\odot}$ and a temperature of $(3300 \pm 300) \mathrm{K}$. Hence it is an M-dwarf and PTF0724 is a HW Vir system. It is the 15th binary of this kind.

Further observations of this interesting system should be aimed at gaining spectra with better quality. It could become possible to determine if the atmospheric parameters of the system change with the orbital phase, due to the reflection effect. If spectral features from the heated atmosphere of the companion could be detected in high-resolution spectra, the mass ratio could be recalculated directly from the spectra and it could be checked if there are any discrepancies with our lightcurve-based solution. But as the system is very faint, this might turn out to be impossible.

A lightcurve with a higher resolution and a better S/N can be used to check for unresolved pulsations.

Lightcurves obtained with different filters would allow to improve the determination of the albedo for the companion.

Fixed parameters:		
$q\,(=M_2/M_1)$		0.33
$T_{\mathrm{eff}}(1)$	[K]	33900
g_1^b		1.0
g_2^b		0.32
x_1^c		0.190
A_1^a		1.0
δ_2^d		0.0

Adjusted parameters:		
i	[°]	83.56 ± 0.3
$T_{\mathrm{eff}}(2)$	[K]	3300 ± 300
A_2^a		1.8 ± 0.2
Ω_1^f		5.544 ± 0.20
Ω_2^f		2.885 ± 0.15
$\frac{L_1}{L_1+L_2}^g$		0.99978 ± 0.00064
δ_1		0.0006 ± 0.0003
x_2		0.510 ± 0.05
l_3^f		0.00 ± 0.001

Roche radii^h:		
$r_1(\mathrm{pole})$	[a]	0.191 ± 0.011
$r_1(\mathrm{point})$	[a]	0.193 ± 0.012
$r_1(\mathrm{side})$	[a]	0.192 ± 0.011
$r_1(\mathrm{back})$	[a]	0.193 ± 0.010
$r_2(\mathrm{pole})$	[a]	0.209 ± 0.013
$r_2(\mathrm{point})$	[a]	0.227 ± 0.013
$r_2(\mathrm{side})$	[a]	0.214 ± 0.017
$r_2(\mathrm{back})$	[a]	0.223 ± 0.015

^{a} Bolometric albedo

^{b} Gravitational darkening exponent

^{c} Linear limb darkening coefficient; from Wade and Rucinski [1985]

^{d} Radiation pressure parameter, see Drechsel et al. [1995]

^{e} Fraction of third light at maximum

^{f} Roche potentials

^{g} Relative luminosity; L_2 is not independently adjusted,
but recomputed from r_2 and $T_{\mathrm{eff}}(2)$

^{h} Fractional Roche radii in units of separation of mass centres

Table 6.1.: Adopted lightcurve solution, q=0.33

PTF1J072456+125301		
i	°	83.56 ± 0.2
M_{sdB}	$[M_\odot]$	0.526 ± 0.05
M_{comp}	$[M_\odot]$	0.174 ± 0.016
a	$[R_\odot]$	0.792 ± 0.025
R_{sdB}	$[R_\odot]$	0.153 ± 0.005
R_{comp}	$[R_\odot]$	0.173 ± 0.005
$\log g(\mathrm{sdB, phot})$		5.79 ± 0.014
$\log g(\mathrm{sdB, spec})$		5.75 ± 0.08

Table 6.2.: Parameters of PTF0724, q=0.33

Fixed parameters:		
$q\,(= M_2/M_1)$		0.435
$T_{\mathrm{eff}}(1)$	[K]	33900
g_1^b		1.0
g_2^b		0.32
x_1^c		0.190
A_1^a		1.0
δ_2^d		0.0
Adjusted parameters:		
i	[°]	83.82 ± 0.2
$T_{\mathrm{eff}}(2)$	[K]	3200 ± 300
A_2^a		1.8 ± 0.1
Ω_1^f		5.485 ± 0.10
Ω_2^f		3.452 ± 0.09
$\frac{L_1}{L_1+L_2}{}^g$		0.99982 ± 0.00064
δ_1		0.001 ± 0.003
x_2		0.565 ± 0.01
l_3^f		0.00 ± 0.001
Roche radii^h:		
$r_1(\mathrm{pole})$	[a]	0.194 ± 0.010
$r_1(\mathrm{point})$	[a]	0.196 ± 0.012
$r_1(\mathrm{side})$	[a]	0.195 ± 0.011
$r_1(\mathrm{back})$	[a]	0.196 ± 0.010
$r_2(\mathrm{pole})$	[a]	0.209 ± 0.014
$r_2(\mathrm{point})$	[a]	0.214 ± 0.013
$r_2(\mathrm{side})$	[a]	0.212 ± 0.013
$r_2(\mathrm{back})$	[a]	0.218 ± 0.015

^{a} Bolometric albedo
^{b} Gravitational darkening exponent
^{c} Linear limb darkening coefficient; from Wade and Rucinski [1985]
^{d} Radiation pressure parameter, see Drechsel et al. [1995]
^{e} Fraction of third light at maximum
^{f} Roche potentials
^{g} Relative luminosity; L_2 is not independently adjusted,
but recomputed from r_2 and $T_{\mathrm{eff}}(2)$
^{h} Fractional Roche radii in units of separation of mass centres

Table 6.3.: Adopted lightcurve solution, q=0.435

PTF1J072456+125301		
i	°	83.82 ± 0.2
M_{sdB}	$[M_\odot]$	0.27 ± 0.025
M_{comp}	$[M_\odot]$	0.118 ± 0.01
a	$[R_\odot]$	0.648 ± 0.02
R_{sdB}	$[R_\odot]$	0.126 ± 0.004
R_{comp}	$[R_\odot]$	0.139 ± 0.004
$\log g(\mathrm{sdB, phot})$		5.66 ± 0.02
$\log g(\mathrm{sdB, spec})$		5.75 ± 0.08

Table 6.4.: Parameters of PTF0724, q=0.435

7. Summary & Outlook

This thesis dealt with the setup and the operation of the Ernst-Hartwig-Telescope at the Remeis Observatory Bamberg and the analysis of a new HW Vir system from the Palomar Transient Factory.

The analysis of the binary from the Palomar Transient Factory revealed the system's HW Vir nature and determined all relevant parameters. It is somewhat remarkable that the flux descends to almost $25\,\%$ during the primary eclipse. This value is among the largest ever observed for all HW Vir systems. PTF is the 15th HW Vir system ever discovered. For further investigation, the determined proper motion and position in the galaxy can be compared to similar systems.

Regarding the other part of the thesis, it was shown that the new equipment is capable of delivering lightcurves and photometric data with very good quality. While the shape of lightcurves stands the comparison with larger telescopes and professional cameras, cutbacks have to made regarding the time resolution. The light polluted sky of Bamberg turned out to be no significant problem, at least not while observing with a blue filter. Due to the target selection, no photometric data has been gathered through other filters.

For searching exoplanets with the LITE method, the achieved accuracy is (far) better than necessary.

Therefore a new scientific project had to be searched to keep the location Bamberg and the EHT alive, regarding the observations. By having the technical possibilities and limitations of the telescope in mind, it soon became clear that the only reasonable usage would lie in the field of photometry again. As the Observatory is already highly involved in the MUCHFUSS project (see Section 5.1) it was only logical to try to find a common interest here. While there are already lots of spectroscopically observed targets in the MUCHFUSS database, only very few of them have been observed photometrically. It was decided to not only limit the observations on MUCHFUSS targets but also observe other known sdB/O systems listed in the GALEX database by Roy Ostensen[1].

It was decided to limit the targets to those brighter than $16\,\text{mag}$ and a declination above $-10°$. This still results in roughly 500 systems.

In a first step, a large number of different targets is observed per night. Looking at every system for about $60\,\text{min}$ to $90\,\text{min}$ should be enough to detect variations in the brightness. If a system doesn't show any changes it will be observed one or two more nights. Variable targets will be given more observation time to eventually cover one full orbit.

The project can be seen as a successor to the observation of UVEXJ212257 that was already done for the MUCHFUSS project.

As every scientific research project a name was needed. It was decided to name the project MAPLE: *Muchfuss Aperture Photometry and Lightcurves with EHT*[2]. And

---

[1] http://www.ster.kuleuven.be/~roy/galex/galex.html
[2] http://www.sternwarte.uni-erlangen.de/Maple.html

as most scientific projects, MAPLE has its own logo. At the moment an automatic

Figure 7.1.: MAPLE logo, designed by Rebekka Kaufmann

data reduction pipeline for the EHT is under construction. This program will be able to call APT from the command line and perform the photometric analysis of a large number of pictures automatically and present the results in a graphical output. It is planed to extend the program to perform the analysis already during the observations. This will not only save a lot of time but also increase the effectiveness of the EHT as it could exactly be seen when there are enough datapoints for a certain target (e.g. after the primary eclipse).

The big advantage of the EHT is its availability. It is neither one of the largest research telescopes nor is the environment (close to the city) the best, but as no other observational projects are carried out in Bamberg, the majority of clear nights could be used without any overbooking or the danger of overrides.

This makes the Remeis Observatory a rather interesting facility for small campaigns and revives the tradition of observing variable stars in Bamberg that had been paused for more than 50 years.

Bibliography

Baader-Planetarium. Planewave cdk - anleitung zur kollimation.

I. Baraffe and G. Chabrier. Mass–Spectral Class Relationship for M Dwarfs. *The Astrophysical Journal*, 461:L51, Apr. 1996. doi: 10.1086/309988.

E. Bertin. Automatic Astrometric and Photometric Calibration with SCAMP. In C. Gabriel, C. Arviset, D. Ponz, and S. Enrique, editors, *Astronomical Data Analysis Software and Systems XV*, volume 351 of *Astronomical Society of the Pacific Conference Series*, page 112, July 2006.

E. Bertin and S. Arnouts. SExtractor: Software for source extraction. *A&A*, 117: 393–404, June 1996.

K. Beuermann, J. Buhlmann, J. Diese, S. Dreizler, F. V. Hessman, T.-O. Husser, G. F. Miller, N. Nickol, R. Pons, D. Ruhr, H. Schmülling, A. D. Schwope, T. Sorge, L. Ulrichs, D. E. Winget, and K. I. Winget. The giant planet orbiting the cataclysmic binary DP Leonis. *A&A*, 526:A53, Feb. 2011. doi: 10.1051/0004-6361/201015942.

K. Beuermann, P. Breitenstein, B. Debski, J. Diese, P. A. Dubovsky, S. Dreizler, F. V. Hessman, K. Hornoch, T.-O. Husser, G. Pojmanski, M. Wolf, P. R. Woźniak, P. Zasche, B. Denk, M. Langer, C. Wagner, D. Wahrenberg, T. Bollmann, F. N. Habermann, N. Haustovich, M. Lauser, F. Liebing, and F. Niederstadt. The quest for companions to post-common envelope binaries. II. NSVS14256825 and HS0705+6700. *A&A*, 540:A8, Apr. 2012a. doi: 10.1051/0004-6361/201118105.

K. Beuermann, S. Dreizler, F. V. Hessman, and J. Deller. The quest for companions to post-common envelope binaries. III. A reexamination of <ASTROBJ>HW Virginis</ASTROBJ>. *A&A*, 543:A138, July 2012b. doi: 10.1051/0004-6361/201219391.

P. Biermann, G. D. Schmidt, J. Liebert, S. Tapia, P. A. Strittmatter, S. West, H. S. Stockman, H. Kuehr, and D. Q. Lamb. The new eclipsing magnetic binary system E 1114 + 182. *The Astrophysical Journal*, 293:303–320, June 1985. doi: 10.1086/163238.

T. M. Brown. *A Far Ultraviolet Analysis of the Stellar Populations in Elliptical and s0 Galaxies*. PhD thesis, THE JOHNS HOPKINS UNIVERSITY, 1997.

B. Carroll and D. Ostlie. *An Introduction to Modern Astrophysics*. 2007.

S. B. Cenko, D. B. Fox, D.-S. Moon, F. A. Harrison, S. R. Kulkarni, J. R. Henning, C. D. Guzman, M. Bonati, R. M. Smith, R. P. Thicksten, M. W. Doyle, H. L. Petrie, A. Gal-Yam, A. M. Soderberg, N. L. Anagnostou, and A. C. Laity. The

Automated Palomar 60 Inch Telescope. *Publications of the Astronomical Society of the Pacific*, 118:1396–1406, Oct. 2006. doi: 10.1086/508366.

G. Chauvin, A.-M. Lagrange, C. Dumas, B. Zuckerman, D. Mouillet, I. Song, J.-L. Beuzit, and P. Lowrance. A giant planet candidate near a young brown dwarf. Direct VLT/NACO observations using IR wavefront sensing. *A&A*, 425:L29–L32, Oct. 2004. doi: 10.1051/0004-6361:200400056.

N. L. D'Cruz, B. Dorman, R. T. Rood, and R. W. O'Connell. The Origin of Extreme Horizontal Branch Stars. *The Astrophysical Journal*, 466:359, July 1996. doi: 10.1086/177515.

B. Dorman, R. T. Rood, and R. W. O'Connell. Ultraviolet Radiation from Evolved Stellar Populations. I. Models. *The Astrophysical Journal*, 419:596, Dec. 1993. doi: 10.1086/173511.

H. Drechsel, S. Haas, R. Lorenz, and S. Gayler. Radiation pressure effects in early-type close binaries and implications for the solution of eclipse light curves. *A&A*, 294:723–743, Feb. 1995.

H. Drechsel, U. Heber, R. Napiwotzki, R. Østensen, J.-E. Solheim, F. Johannessen, S. L. Schuh, J. Deetjen, and S. Zola. HS 0705+6700: A new eclipsing sdB binary. *A&A*, 379:893–904, Dec. 2001. doi: 10.1051/0004-6361:20011376.

T. Driebe, D. Schoenberner, T. Bloecker, and F. Herwig. The evolution of helium white dwarfs. I. The companion of the millisecond pulsar PSR J1012+5307. *A&A*, 339:123–133, Nov. 1998.

F. R. Ferraro, B. Paltrinieri, F. Fusi Pecci, C. Cacciari, B. Dorman, and R. T. Rood. Hubble Space Telescope Ultraviolet Observations of the Cores of M3 and M13. *The Astrophysical Journal*, 484:L145–L148, Aug. 1997. doi: 10.1086/310780.

G. Fontaine, Brassard, P., Charpinet, S., Green, E. M., Randall, S. K., and Van Grootel, V. A preliminary look at the empirical mass distribution of hot b subdwarf stars. *A&A*, 539:A12, 2012. doi: 10.1051/0004-6361/201118220. URL `http://dx.doi.org/10.1051/0004-6361/201118220`.

S. Geier, U. Heber, A. Tillich, H. Hirsch, H. Edelmann, V. Schaffenroth, T. Kupfer, S. Müller, P. F. L. Maxted, R. Østensen, P. Podsiadlowski, T. Marsh, B. Gänsicke, L. Morales-Rueda, G. Nelemans, R. Napiwotzki, E. W. Günther, and L. Carone. Hot subdwarfs in binary systems and the nature of their unseen companions. *Astrophysics and Space Science*, 329:91–99, Oct. 2010. doi: 10.1007/s10509-010-0327-9.

S. Geier, V. Schaffenroth, H. Hirsch, A. Tillich, U. Heber, P. F. L. Maxted, R. H. Østensen, B. N. Barlow, S. J. O'Toole, T. Kupfer, T. Marsh, B. Gänsicke, R. Napiwotzki, O. Cordes, S. Müller, L. Classen, E. Ziegerer, and H. Drechsel. MUCHFUSS - Massive Unseen Companions to Hot Faint Underluminous Stars from SDSS. *Astronomische Nachrichten*, 333:431, June 2012. doi: 10.1002/asna.201211684.

R. F. Green, D. O. Richstone, and M. Schmidt. PG 1413+01 - A white dwarf-red dwarf eclipsing binary. *The Astrophysical Journal*, 224:892, Sept. 1978. doi: 10.1086/156439.

U. Heber. Hot Subdwarf Stars. *Annu. Rev. Astro. Astrophys*, 47:211–251, Sept. 2009. doi: 10.1146/annurev-astro-082708-101836.

U. Heber, I. N. Reid, and K. Werner. Spectral analysis of multi mode pulsating sdB stars. II. Feige 48, KPD 2109+4401 and PG 1219+534. *A&A*, 363:198–207, Nov. 2000.

H. Heinicke. "gm4000 hps bedienungsanleitung, 2012.

H. Hirsch. Hot subluminous stars: On the search for chemical signatures of their genesis, 2009.

R. K. Honeycutt. CCD ensemble photometry on an inhomogeneous set of exposures. *Publications of the Astronomical Society of the Pacific*, 104:435–440, June 1992. doi: 10.1086/133015.

J. Kallrath and A. P. Linnell. A new method to optimize parameters in solutions of eclipsing binary light curves. *The Astrophysical Journal*, 313:346–357, Feb. 1987. doi: 10.1086/164971.

D. Kilkenny, C. Koen, D. O'Donoghue, and R. S. Stobie. A new class of rapidly pulsating star - I. EC 14026-2647, the class prototype. *MNRAS*, 285:640–644, Mar. 1997.

R. R. Laher, V. Gorjian, L. M. Rebull, F. J. Masci, J. W. Fowler, G. Helou, S. R. Kulkarni, and N. M. Law. Aperture Photometry Tool. *Publications of the Astronomical Society of the Pacific*, 124:737–763, July 2012. doi: 10.1086/666883.

N. M. Law, S. R. Kulkarni, R. G. Dekany, E. O. Ofek, R. M. Quimby, P. E. Nugent, J. Surace, C. C. Grillmair, J. S. Bloom, M. M. Kasliwal, L. Bildsten, T. Brown, S. B. Cenko, D. Ciardi, E. Croner, S. G. Djorgovski, J. van Eyken, A. V. Filippenko, D. B. Fox, A. Gal-Yam, D. Hale, N. Hamam, G. Helou, J. Henning, D. A. Howell, J. Jacobsen, R. Laher, S. Mattingly, D. McKenna, A. Pickles, D. Poznanski, G. Rahmer, A. Rau, W. Rosing, M. Shara, R. Smith, D. Starr, M. Sullivan, V. Velur, R. Walters, and J. Zolkower. The Palomar Transient Factory: System Overview, Performance, and First Results. *Publications of the Astronomical Society of the Pacific*, 121:1395–1408, Dec. 2009. doi: 10.1086/648598.

J. W. Lee, S.-L. Kim, C.-H. Kim, R. H. Koch, C.-U. Lee, H.-I. Kim, and J.-H. Park. The sdB+M Eclipsing System HW Virginis and its Circumbinary Planets. *AJ*, 137:3181–3190, Feb. 2009. doi: 10.1088/0004-6256/137/2/3181.

D. Levitan, B. J. Fulton, P. J. Groot, S. R. Kulkarni, E. O. Ofek, T. A. Prince, A. Shporer, J. S. Bloom, S. B. Cenko, M. M. Kasliwal, N. M. Law, P. E. Nugent, D. Poznanski, R. M. Quimby, A. Horesh, B. Sesar, and A. Sternberg. PTF1 J071912.13+485834.0: An Outbursting AM CVn System Discovered by a Synoptic Survey. *The Astrophysical Journal*, 739:68, Oct. 2011. doi: 10.1088/0004-637X/739/2/68.

L. B. Lucy. Gravity-Darkening for Stars with Convective Envelopes. *Zeitschrift für Astrophysik*, 65:89, 1967.

P. f. L. Maxted, U. Heber, T. R. Marsh, and R. C. North. The binary fraction of extreme horizontal branch stars. *MNRAS*, 326:1391–1402, Oct. 2001. doi: 10.1111/j.1365-8711.2001.04714.x.

P. F. L. Maxted, T. R. Marsh, U. Heber, L. Morales-Rueda, R. C. North, and W. A. Lawson. Photometry of four binary subdwarf B stars and the nature of their unseen companion stars. *MNRAS*, 333:231–240, June 2002. doi: 10.1046/j. 1365-8711.2002.05406.x.

M. Mayor and D. Queloz. A Jupiter-mass companion to a solar-type star. *Nature*, 378:355–359, Nov. 1995. doi: 10.1038/378355a0.

J. W. Menzies and F. Marang. A New B-Subdwarf Eclipsing Binary with an Extremely Short Period. In J. B. Hearnshaw and P. L. Cottrell, editors, *Instrumentation and Research Programmes for Small Telescopes*, volume 118 of *IAU Symposium*, page 305, 1986.

M. W. Muterspaugh, M. Konacki, B. F. Lane, and E. Pfahl. Observational Techniques for Detecting Planets in Binary Systems. *ArXiv e-prints*, May 2007.

T. Naylor. An optimal extraction algorithm for imaging photometry. *MNRAS*, 296: 339–346, May 1998. doi: 10.1046/j.1365-8711.1998.01314.x.

E. O. Ofek, D. A. Frail, B. Breslauer, S. R. Kulkarni, P. Chandra, A. Gal-Yam, M. M. Kasliwal, and N. Gehrels. A Very Large Array Search for 5 GHz Radio Transients and Variables at Low Galactic Latitudes. *The Astrophysical Journal*, 740:65, Oct. 2011. doi: 10.1088/0004-637X/740/2/65.

S. G. Parsons, T. R. Marsh, C. M. Copperwheat, V. S. Dhillon, S. P. Littlefair, R. D. G. Hickman, P. F. L. Maxted, B. T. Gänsicke, E. Unda-Sanzana, J. P. Colque, N. Barraza, N. Sánchez, and L. A. G. Monard. Orbital period variations in eclipsing post-common-envelope binaries. *MNRAS*, 407:2362–2382, Oct. 2010. doi: 10.1111/j.1365-2966.2010.17063.x.

S. G. Parsons, T. R. Marsh, B. T. Gänsicke, A. Rebassa-Mansergas, V. S. Dhillon, S. P. Littlefair, C. M. Copperwheat, R. D. G. Hickman, M. R. Burleigh, P. Kerry, D. Koester, A. Nebot Gómez-Morán, S. Pyrzas, C. D. J. Savoury, M. R. Schreiber, L. Schmidtobreick, A. D. Schwope, P. R. Steele, and C. Tappert. A precision study of two eclipsing white dwarf plus M dwarf binaries. *MNRAS*, 420:3281–3297, Mar. 2012. doi: 10.1111/j.1365-2966.2011.20251.x.

E.-M. Pauli, U. Heber, R. Napiwotzki, M. Altmann, and M. Odenkirchen. 3D-Kinematics of White Dwarfs from the SPY-Project. In D. Koester and S. Moehler, editors, *14th European Workshop on White Dwarfs*, volume 334 of *Astronomical Society of the Pacific Conference Series*, page 81, July 2005.

PlaneWave-Instruments. Electronic focuser accessory hand controller instructions.

T. Pribulla , M. Vaňko, M. Ammler-von Eiff, M. Andreev, A. Aslantürk, N. Awadalla, D. Baluďanský, A. Bonanno, H. Božić, G. Catanzaro, L. Çelik, P. E. Christopoulou, E. Covino, F. Cusano, D. Dimitrov, P. Dubovský, P. Eigmueller, E. M. Esmer, A. Frasca, Ľ. Hambálek, M. Hanna, A. Hanslmeier, B. Kalomeni, D. P. Kjurkchieva, V. Krushevska, I. Kudzej, E. Kundra, Y. Kuznyetsova, J. W. Lee, M. Leitzinger, G. Maciejewski, D. Moldovan, M. H. M. Morais, M. Mugrauer, R. Neuhäuser, A. Niedzielski, P. Odert, J. Ohlert, İ. Özavcı, A. Papageorgiou, Š. Parimucha, S. Poddaný, A. Pop, M. Raetz, S. Raetz, Y. Romanyuk, D. Ruždjak, J. Schulz, H. V. Şenavcı, G. Srdoc, T. Szalai, P. Székely, D. Sudar, C. T. Tezcan, M. E. Törün, V. Turcu, O. Vince, and M. Zejda. The Dwarf project: Eclipsing binaries - precise clocks to discover exoplanets. *Astronomische Nachrichten*, 333:754, Oct. 2012. doi: 10.1002/asna.201211722.

S.-B. Qian, L.-Y. Zhu, Z.-B. Dai, E. Fernández-Lajús, F.-Y. Xiang, and J.-J. He. Circumbinary Planets Orbiting the Rapidly Pulsating Subdwarf B-type Binary NY Vir. *The Astrophysical Journal Letters*, 745:L23, Feb. 2012. doi: 10.1088/2041-8205/745/2/L23.

S.-B. Qian, G. Shi, S. Zola, D. Koziel-Wierzbowska, M. Winiarski, T. Szymanski, W. Ogloza, L.-J. Li, L.-Y. Zhu, L. Liu, J.-J. He, W.-P. Liao, E.-G. Zhao, J.-J. Wang, J. Zhang, and L.-Q. Jiang. A search for substellar objects orbiting the sdB eclipsing binary HS 0705+6700. *MNRAS*, 436:1408–1414, Dec. 2013. doi: 10.1093/mnras/stt1659.

I. Ribas. *Cof. Ser. Astrophysics of Variable Stars*, 349, 2006.

H. Ritter and U. Kolb. Catalogue of cataclysmic binaries, low-mass X-ray binaries and related objects (Seventh edition). *A&A*, 404:301–303, June 2003. doi: 10.1051/0004-6361:20030330.

V. Schaffenroth. Subdwarf b-sterne in binärsystemen: Drei neue hw vir-typen und die durchmusterung des corot anticenter-feldes, 2010.

V. Schaffenroth, S. Geier, U. Heber, T. Kupfer, E. Ziegerer, C. Heuser, L. Classen, and O. Cordes. Binaries discovered by the MUCHFUSS project. SDSS J162256.66+473051.1: An eclipsing subdwarf B binary with a brown dwarf companion. *A&A*, 564:A98, Apr. 2014. doi: 10.1051/0004-6361/201423377.

A. Tillich, S. Geier, U. Heber, H. Hirsch, P. F. L. Maxted, T. Marsh, B. Gänsicke, R. Napiwotzki, R. Østensen, and R.-D. Scholz. The HYPER-MUCHFUSS project - target selection and analysis. *Astrophysics and Space Science*, 329:63–68, Oct. 2010. doi: 10.1007/s10509-010-0306-1.

H. von Zeipel. Radiative equilibrium of a double-star system with nearly spherical components. *MNRAS*, 84:702, June 1924.

M. Vučković, C. Aerts, R. Östensen, G. Nelemans, H. Hu, C. S. Jeffery, V. S. Dhillon, and T. R. Marsh. The binary properties of the pulsating subdwarf B eclipsing binary <ASTROBJ>PG 1336-018</ASTROBJ> (NY Virginis). *A&A*, 471:605–615, Aug. 2007. doi: 10.1051/0004-6361:20077179.

R. A. Wade and S. M. Rucinski. Linear and quadratic limb-darkening coefficients for a large grid of LTE model atmospheres. *A&A*, 60:471–484, June 1985.

R. F. Webbink. Double white dwarfs as progenitors of R Coronae Borealis stars and Type I supernovae. *The Astrophysical Journal*, 277:355–360, Feb. 1984. doi: 10.1086/161701.

R. E. Wilson and E. J. Devinney. Realization of Accurate Close-Binary Light Curves: Application to MR Cygni. *The Astrophysical Journal*, 166:605, June 1971. doi: 10.1086/150986.

J. H. Wood and R. Saffer. Spectroscopy of the post-common envelope binary HW Virginis. *MNRAS*, 305:820–828, May 1999. doi: 10.1046/j.1365-8711.1999.02501. x.

List of Figures

82

List of Tables

Acknowledgements

Appendix

A. Focus

Figure .2.: Correct focus with a Bathinov mask [1]

[1]daltonskygazer.com/wp-content/uploads/2014/08/In-Focu.jpg

B. Python programs

B.1. quartz.py

```python
import math

print("Quartzkorrektur GM 4000 HPS (SBIG STL 11k/STX 16803 und CDK 20'')")

print(".............................................................")

##########################################################################
errortime=1

while errortime==1:
  time = input("Belichtungszeit/[s]:")
  try:
    ct=int(time)
    errortime=0
  except:
    print("FEHLER:Bite nur integer Zahlen ohne Einheit eingeben!")

errorlength=1

while errorlength==1:
  length = input("Laenge der Strichspur/[Pixel]: ")
  try:
    cl=float(length)
    errorlength=0

  except:
    print("FEHLER:Laenge der Strichspur bitte ohne Einheiten angeben!")
```

```python
28
29 errorangle=1
30
31 while errorangle==1:
32    angle = input("Winkel der Deklination/[°]: ")
33    try:
34       ca=float(angle)
35       errorangle=0
36    except:
37       print("FEHLER:Winkel in Grad bitte ohne Einheit angeben!")
38
39 ##################################################################
40 def transform(angle):
41    a = math.radians(float(angle))
42    return a
43 a=transform(angle)
44
45 def correction(time,length):
46    c=((((2150*float(length))/4008)/float(time))/(14.959*math.cos(a)))*100
47    return c
48 c=correction(time,length)
49 ##################################################################
50 print("Korrekturfaktor=",c,"%")
51 print(".............................................................")
52 print("gerundeter Wert für die Steuerung:",round(c,3),"%")
53 print("Clear skies!")
```

B.2. ephemeris.py

```python
import sys
print("#####################")
print("Eclipse calculator V 1.2")
print("#####################")
LoopI=1#known ephemeris
while LoopI==1:
  n=input("known ephemeris:")
  try:
      zero=float(n)
      LoopI=0
  except:
      print("Unkown input!")
zero=float(n)

LoopII=1#Period
while LoopII==1:
  p=input("Period/[d]:")
  try:
      period=float(p)
      LoopII=0
  except:
      print("Unkown input!")
period=float(p)

LoopIII=1#Year
while LoopIII==1:
  j=input("Year:")
  try:
      year=int(j)
```

```python
30          LoopIII=0
31      except:
32          print("Unkown input!")
33  year=int(j)
34
35  LoopIV=1#Month
36  while LoopIV==1:
37      m=input("Month:")
38      try:
39          month=int(m)
40          LoopIV=0
41      except:
42          print("Unkown input!")
43  month=int(m)
44
45  LoopV=1#Day
46  while LoopV==1:
47      t=input("Day:")
48      try:
49          day=int(t)
50          LoopV=0
51      except:
52          print("Unkown Input!")
53  day=int(t)
54  ###############################################################
55
56  if month==1 or month==2:
57      Year=year-1
58      Month=month+12
59  else:
60      Year=year
```

```python
    Month=month

A=int(Year/100)
B=2-A+int(A/4)
JD=int(365.25*(Year+4716))+int(30.6001*(Month+1))+day+B-1524

print("today:(JD):",JD)
###################################################################
X=((JD-zero)/period)
Y=1-(X%1)
Rest=Y*period
print("rest of periods (days):",Rest)
HR=Y*period*24#rest in hours
MR=(HR%1)*60#rest in minutes
SR=(MR%1)*60#rest in seconds

print("first eclipse:", 12+int(HR),":",int(MR),":",int(SR),"UT")
#Recalculation of period
H_per=int(period*24)
M_per=int(((period*24)%1)*60)
S_per=float(((((period*24)%1)*60)%1)*60)
print("Period:",H_per,":",M_per,":",round(S_per,2))
LoopVI=1#Number of cycles
while LoopVI==1:
    num=input("How many cycles should be added?")#Perionds
    try:
        number=int(num)
        LoopVI=0
    except:
        print("Unkown input! Only use integer numbers!")
number=int(num)
```

```python
92 ################################################################
93 HR=HR+12
94 for i in range (0,number):
95     i=i+1#start loop
96     HR=int(HR)+H_per
97     MR=int(MR)+M_per
98     SR=int(SR)+S_per
99     if SR>60:
100       SR=SR-60
101       MR=MR+1
102       if MR>60:
103               MR=MR-60
104               HR=HR+1
105               if HR>23:
106                   HR=HR-24
107               else:pass
108       else:pass
109     else:
110       if MR>60:
111               MR=MR-60
112               HR=HR+1
113               if HR>23:
114                   HR=HR-24
115               else:pass
116       else:
117         if HR>23:
118             HR=HR-24
119
120     print("next eclipse:",HR,":",MR,":",round(SR,2))
121 print("All times are UT!")
```

B.3. outut.py

```
1  print("Bitte warten...")
2  import sys
3  import pyfits
4
5  print("APT-Output Converter V3.2")
6  print("(Für eine beliebige Anzahl an Vergleichssterne)")
7  print("-------------------------")
8
9  SchleifeI=1
10 while SchleifeI==1:
11     inputname=input("Input-Datei:")#Name der Start-Datei
12     try:
13         d=open(inputname)
14         print("Input-Datei geoeffnet!")
15         SchleifeI=0
16     except:
17         print("Dateizugriff nicht erfolgreich!")
18         # sys.exit(0)
19
20 #Gesamten Text einlesen
21 alledaten=d.read()
22 print("Daten eingelesen!")
23
24 d.close()
25 print("Input-Datei geschlossen!")
26
27 #Umwandeln in Liste von Zeilen
28 zeilenliste=alledaten.split(chr(10))#chr(10) liefert Unicode Zeichen für Zeilenende
29
```

```python
30  print("Liste von Zeilen erzeugt!")
31  print("Ausgabe:")
32
33  #Zeilen unwandeln in Listen
34  li=[]
35  for zeile in zeilenliste:
36    if zeile:
37      zwliste=zeile.split(",")#auf richtige Trennung achten!!!
38      li.append([str(zwliste[i]) for i in range(0,37)])
39
40  #jetzt das so und so [...] Element der Liste ausgeben, für alle Zeilen!
41  for p in li:
42    print(p[0],p[10],p[12],p[11])#number, mag, mag uncertainty,aperture correction
43  print("Ausgabe abgeschlossen!")
44
45  #Abfrage der #Referenzsterne fuer korrekte Ausgabe
46  SchleifeII=1
47  while SchleifeII==1:
48    refstar=input("Anzahl der Referenzsterne:")
49    try:
50      control_ref=int(refstar)
51      print("Referenzsterne gespeichert")
52      SchleifeII=0
53    except:
54      print("Nur integer Zahlen eingeben!")
55  control_ref=int(refstar)
56
57  #neues CSV-File erzeugen
58  SchleifeIII=1
59  while SchleifeIII==1:
60    outputname=input("Output .CSV-Datei:")#Name der Start-Datei
```

```
61    try:
62       a=open(outputname,"w")#mit "w" wird bestehende Datei überschrieben
63       print("neues CSV-File angelegt und geöffnet!")
64       SchleifeIII=0
65    except:
66       print("Dateizugriff nicht erfolgreich!")
67       #sys.exit(0)
68
69 z=0#Zaehler fuer die laufende Nummer im Outputfile
70
71 ##############################################################################
72 abfrage=input("Sollen die Aufnahmezeiten aus dem FITS-Header eingelesen werden? (J/N)")
73 frage=str(abfrage)
74
75 if frage=="J" or frage=="j":
76    SchleifeIVa=1
77    while SchleifeIVa==1:
78       anfang=input("Nummer des ersten FITS-Bildes:")
79       try:
80          start=int(anfang)
81          SchleifeIVa=0
82       except:
83          print("Es gibt nur ganze Bilder...")
84
85    SchleifeIVb=1
86    while SchleifeIVb==1:
87       ende=input("Nummer des letzten FITS-Bildes:")
88       try:
89          ziel=int(ende)
90          SchleifeIVb=0
91       except:
```

```python
         print("Es gibt nur ganze Bilder...")

  SchleifeV=1
  while SchleifeV==1:
    dateiname=input("Dateiname FITS-File eingeben (ohne lfd.Nr.)!")
    name=str(dateiname)
    try:
      header_primary=pyfits.getheader(name+str(zahl).zfill(4)+".fit")
      SchleifeV=0
    except:
      print("Datei nicht gefunden!")
  #x=0#Zähler für Ausgabe des Fits Headers
  for i in range(start,ziel):
    start=start+1
    header_primary=pyfits.getheader(name+str(start).zfill(4)+".fit")
    header_primary[9]=header_primary[9].replace("T",";").replace(".000","").replace("2014-","")
    #milisekunden löschen, jahr löschen, T durch; ersetzen
    print(header_primary[9])

  print("Zeit-Format angepasst!")

else:
  pass

start=int(anfang)#reset von start, nur zu Sicherheit

SchleifeV=1
while SchleifeV==1:
  Entscheidung=input("Sollen die Magnituden oder die Intensitäten herausgeschrieben werden? (mag/int)")
  Wahl=str(Entscheidung)
  if Wahl=="mag":
```

```python
        print("Es werden Magnituden verwendet!")
        print("Nur für differentielle Photometrie zu benutzen!")
        SchleifeV=0
    elif Wahl=="int":
        print("Es werden Intensitäten verwendet!")
        print("ACHTUNG! Intensität in D.U. (data units) angegeben! Normierung beachten!")
        print("(Nur für dieefferentielle Photometrie zu benutzen!!!")
        SchleifeV=0
    else:
        print("Bitte Eingabe überprüfen!")

Wahl=str(Entscheidung)

if Wahl=="mag":
    for p in li:
        if str(p[0])==str(1):#z wird nur bei jedem ...Eintrag hochgezaehlt, entsprechend einem neuen Bild
            z=z+1
            start=start+1
            a.write(str(z)+","+str(p[14])+","+str(p[15])+",")
        elif str(p[0])>str(1) and str(p[0])<=str(control_ref):
            a.write(str(p[14])+","+str(p[15])+",")
        elif str(p[0])==str(control_ref+1):
            if frage==str("J") or frage==str("j"):
                header_primary=pyfits.getheader(name+str(start).zfill(4)+".fit")
                a.write(str(p[14])+","+str(p[15])+","+
                header_primary[9].replace("T",";").replace(".000","").replace("2014-","")+"\n")
            else:
                a.write(str(p[14])+","+str(p[15])+"\n")
        elif str(p[0])==str("Number"):
            pass
```

```python
elif Wahl=="int":
  for p in li:
    if str(p[0])==str(1):#z wird nur bei jedem ...Eintrag hochgezaehlt, entsprechend einem neuen Bild
      z=z+1
      start=start+1
      a.write(str(z)+","+str(p[10])+","+str(p[12])+",")
    elif str(p[0])>str(1) and str(p[0])<=str(control_ref):
      a.write(str(p[10])+","+str(p[12])+",")
    elif str(p[0])==str(control_ref+1):
      if frage==str("J") or frage==str("j"):
          header_primary=pyfits.getheader(name+str(start).zfill(4)+".fit")
          a.write(str(p[10])+","+str(p[12])+","+
          header_primary[9].replace("T",";").replace(".000","").replace("2014-","")+"\n")
      else:
          a.write(str(p[10])+","+str(p[12])+"\n")
    elif str(p[0])==str("Number"):
      pass

else:
  print("Wie sind Sie denn hier hin gekommen?")
  sys.exit(0)
print("Datensaetze eingetragen!")

a.close()

print("Output-Datei geschlossen!")
print("Viel Spaß beim weiteren Auswerten ;-)")
```

B.4. JDcorrection.py

```
1 #Die Aufnahmedaten im FITS Header der SBIG Kameras sind schon in UTC umgerechnet sein
2 #Eine Korrektur von MEZ/MESZ ist daher nicht notwendig!
3
4 import sys
5 print("Juliansiches Datum erzeugen")
6
7 SchleifeI=1#Inputdatei
8 while SchleifeI==1:
9   inputname=input("Input-Datei:")#Name der Start-Datei
10   try:
11       d=open(inputname)
12       print("Input-Datei geoeffnet!")
13       SchleifeI=0
14   except:
15       print("Dateizugriff nicht erfolgreich!")
16
17 SchleifeII=1#Jahreszahl
18 while SchleifeII==1:
19   J=input("Jahreszahl:")
20   try:
21       jahr=int(J)
22       SchleifeII=0
23   except:
24       print("Eingabe nicht erkannt")
25 jahr=int(J)
26
27
28 SchleifeIII=1#baryzentrische Korrektur
29 while SchleifeIII==1:
```

```python
30    bar=input("baryzentrische Korrektur eingeben:")
31    try:
32        bar_cor=float(bar)
33        SchleifeIII=0
34    except:
35        print("Eingabe nicht erkannt! Nur Float Zahlen eingeben!")
36 barycor=float(bar)
37
38 SchleifeIV=1#Belichtungszeit für shiften der Aufnahmen auf mid-exposure time
39 while SchleifeIV==1:
40    exposure=input("Belichtungszeit[s]:")
41    try:
42        exptime=int(exposure)
43        SchleifeIV=0
44    except:
45        print("Eingabe nicht erkannt!Nur integer zahlen Eingeben, ohne Einheiten")
46 exptime=int(exposure)
47
48 #Gesamten Text einlesen
49 alledaten=d.read()
50 print("Daten eingelesen!")
51
52
53 d.close()
54 print("Input-Datei geschlossen!")
55
56 #Umwandeln in Liste von Zeilen
57 zeilenliste=alledaten.split(chr(10))#chr(10) liefert Unicode Zeichen für Zeilenende
58 #del zeilenliste[0] in der neusten Version von output.py (ohne Beschriftung) nicht mehr nötig
59 del zeilenliste[-1] #wegen Zeilenumbruch in output.py
60 print("Liste von Zeilen erzeugt!")
```

```python
#Zeilen  unwandeln  in  Listen
li=[]
for  zeile  in  zeilenliste:
  if  zeile:
    zwliste=zeile.split(",")#auf  richtige  Trennung  achten!!!
    li.append([wert  for  wert  in  zwliste])

print("Ausgabe:")
for  p  in  li:
  print(p[0],p[-1])#number,  FITS  HEADER  TIME
print("Ausgabe  abgeschlossen!")

SchleifeIV=1#Outputdatei
while  SchleifeIV==1:
  outputname=input("Output-Datei:")#Name  der  Start-Datei
  try:
      outputfile=open(outputname,  "w")
      print("Output-Datei  geoeffnet!")
      SchleifeIV=0
  except:
      print("Dateizugriff  nicht  erfolgreich!")
    #  sys.exit(0)

outputfile=open(outputname,  "w")


times  =  []
for  time_with_date  in  li:#Aufspaltung  der  FITS-Header  Information
  date_and_time  =  time_with_date[-1].split(";")#-1  greift  auf  letzten  Eintrag  der  zeile  zu
  time  =  date_and_time[-1]
```

```python
92    date = date_and_time[0]
93    time_splitted = time.split(":")
94    date_splitted = date.split("-")
95
96    #Umbenennung
97    M=int(date_splitted[0])
98    D=int(date_splitted[1])
99    h=int(time_splitted[0])
100   m=int(time_splitted[1])
101   s=int(time_splitted[2])
102
103   if M==1 or M==2:
104       Jahr=jahr-1#Jahr ungleich jahr, da sonst der neue Wert als Anfangswert
105       #bei einem erneutzen Schleifendurchlauf gesetzt wird
106       M=M+12
107   else:
108       Jahr=jahr
109
110   A=int(Jahr/100)
111   B=2-A+int(A/4)
112   H=(h/24)+(m/1440)+(s/86400)#Bestimmung der Nachkommastelle für einen Tag
113   JD=int(365.25*(Jahr+4716))+int(30.6001*(M+1))+D+H+B-1524.5
114   JD_barycor=JD+barycor#Anwenden der baryzentrischen Korrektur
115   JD_shifted=JD_barycor+((exptime/2)/(24*3600))#Shift auf Mid-exposure time.
116   #Umrechnung auf Tagesbruchteile
117   JD_shifted2=str(JD_shifted)
118   print(JD_shifted2)
119   times.append(JD_shifted2)
120 print("Ausgabe JD abgeschlossen!")
121
122 for zeile in zeilenliste:
```

```
123    outputfile.write(zeile)
124    outputfile.write(",")
125    outputfile.write(str(times[zeilenliste.index(zeile)]))
126    outputfile.write("\n")
127
128 outputfile.close()
129 print("Output-Datei geschlossen!")
```

C. Mount-dynamics
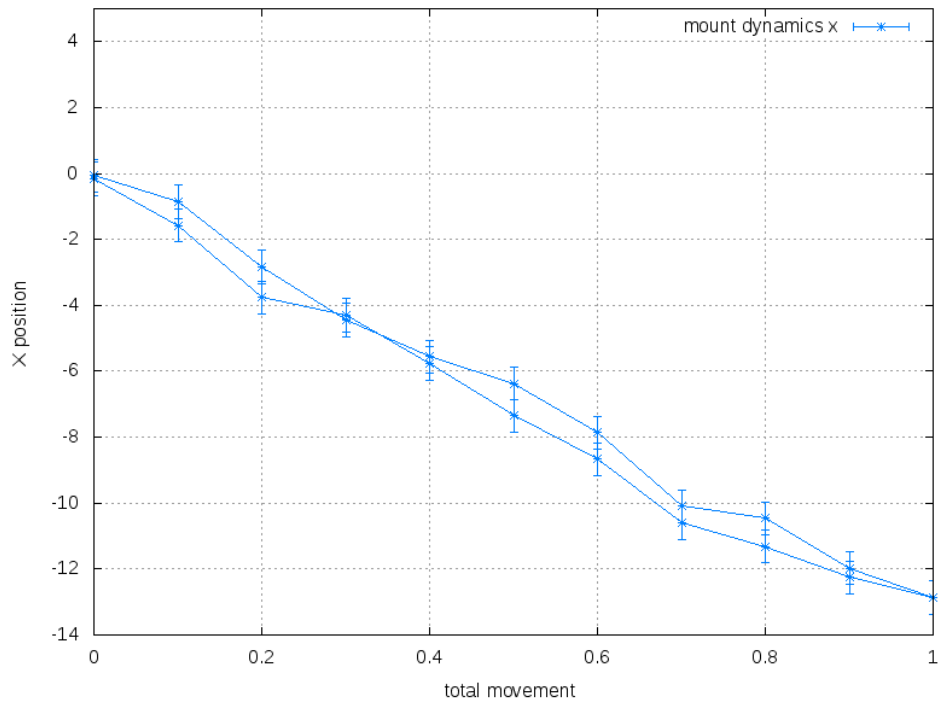
Figure .3.: mount-dynamics for x-movement 0.1 s
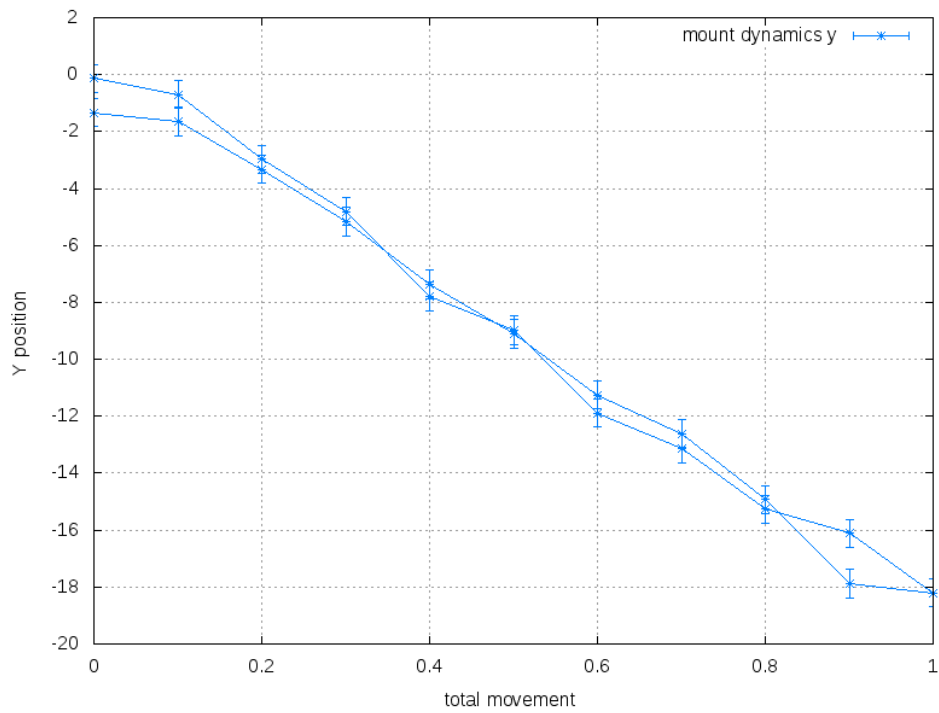
Figure .4.: mount-dynamics for y-movement 0.1 s
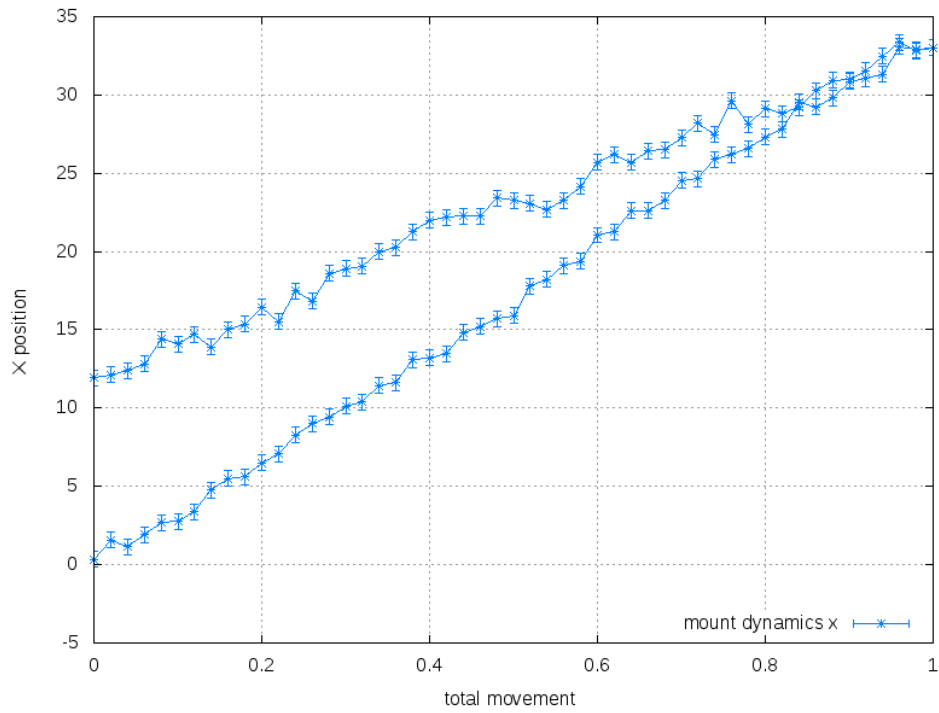
Figure .5.: mount-dynamics for x-movement 0.04 s
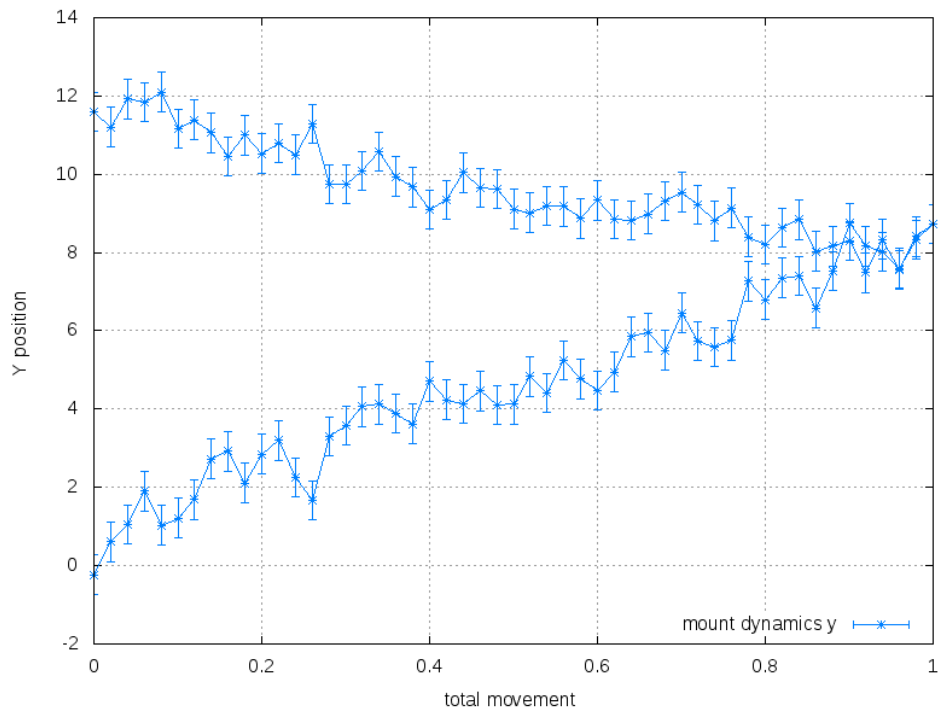
Figure .6.: mount-dynamics for y-movement 0.04 s

D. Reference stars
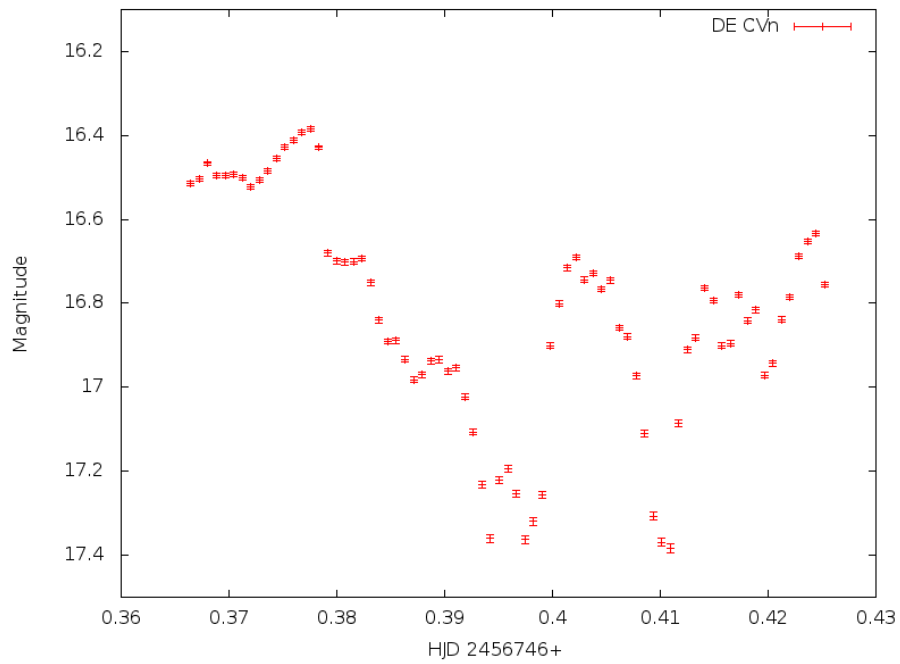
Figure .7.: Lightcurve of DE CVn before applying the brightness correction by comparrison stars
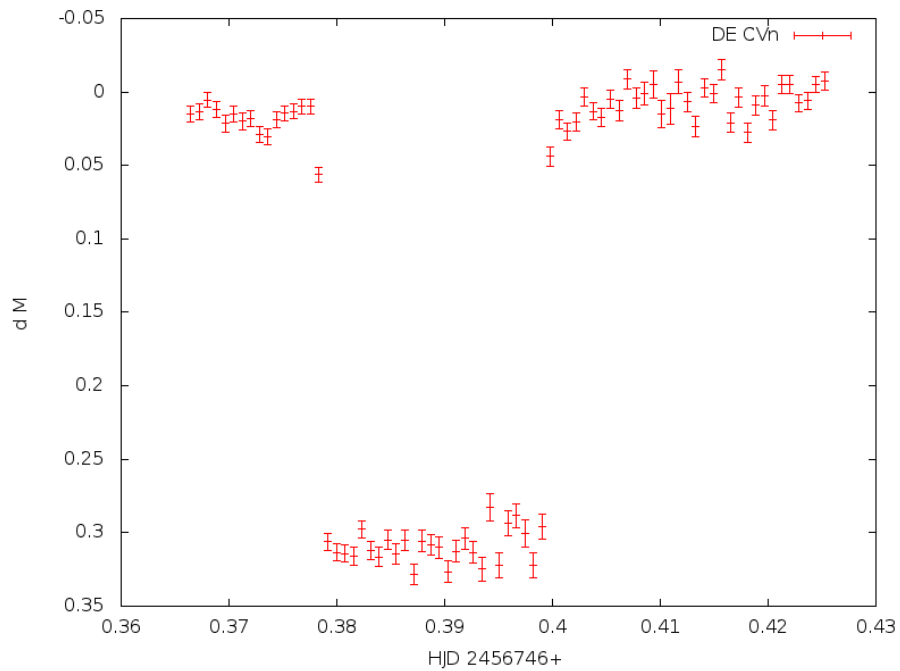
Figure .8.: Lightcurve of DE CVn after applying the brightness correction by comparrison stars

E. Target and eclipse timings

E.1. Target list

Object	α_{2000}	δ_{2000}	Sp.type	Period [days]	V
V470 Cam	07 10 42.1	+66 55 44	sdB+M	0.09564665	14.7
DP Leo	11 17 16.0	+17 57 41.1	DA/M5V(?)	0.0623628565	17.5
HW Vir	12 44 20.2	-08 40 17	sdB+M6-7	0.11671947	10.5
DE CVn	13 26 53.3	+45 32 47	M3V+DA	0.36413940	12.8
NY Vir	13 38 48.1	-02 01 49	sdB+M5	0.10101598	13.3
GK Vir	14 15 36.5	+01 17 17.7	WD+M3V	0.3443308388	17.0
UVEXJ212257	21 22 57.8	+55 26 09	dA+dM	(?)	$\sim 15(?)$

Table .1.: Overview of observed objects and their properties (as far as known)

E.2. Overview of mid eclipse timings

Object	date of observations	mid eclipse timing (TCB)	error [d]
V470 Cam	02/23/2014	2456712.312122	$2.963 \cdot 10^{-5}$
V470 Cam	02/23/2014	2456712.40779	$3.288 \cdot 10^{-5}$
V470 Cam	02/23/2014	2456712.503441	$6.632 \cdot 10^{-5}$
V470 Cam	03/09/2014	2456726.372817	$3.833 \cdot 10^{-5}$
V470 Cam	03/20/2013	2456737.372278	$4.305 \cdot 10^{-5}$
V470 Cam	03/28/2014	2456745.40759	$3.652 \cdot 10^{-5}$
NY Vir	04/20/2014	2456768.387636	$2.344 \cdot 10^{-5}$
NY Vir	05/19/2014	2456797.480147	$7.355 \cdot 10^{-5}$
NY Vir	05/24/2014	2456802.430139	$2.342 \cdot 10^{-5}$
HW Vir	04/16/2014	2456764.44474	$1.745 \cdot 10^{-5}$
HW Vir	05/19/2014	2456797.434214	$3.091 \cdot 10^{-5}$
GK Vir	04/20/2014	2456768.4873638	$6.0 \cdot 10^{-5}$
GK Vir	05/19/2014	2456797.410905	$6.0 \cdot 10^{-5}$
DP Leo	03/20/2014	2456737.445869	$5.0 \cdot 10^{-4}$
DE CVn	03/29/2014	2456746.3890905	$5.0 \cdot 10^{-5}$

Table .2.: Observed objects and determined mid eclipse timings

F. RV measurements PTF0724

HJD	RV in km/s	
2455477.930387	-113	±15.6
2455477.933084	-82	±23
2455477.935414	-61	±19.8
2455477.937745	-105	±13.2
2455477.940076	-116	±29.5
2455477.942406	-86	±27.1
2455477.944737	-95	±8.2
2455477.949969	-86	±56.8
2455477.952300	-151	±6.9
2455477.954630	-99	±44.8
2455477.956961	-85	±22.4
2455477.959292	-96	±40.3
2455477.961622	-60	±12.2
2455477.963953	-37	±37.1
2455477.966283	-74	±29.2
2455477.968614	-131	±48.8
2455477.970944	-67	±26.8
2455477.973524	-53	±14.3
2455477.980647	-16	±36.4
2455477.982977	-9	±18.5
2455477.985308	+53	±3.5
2455477.988790	+88	±17.9
2455477.991121	+32	±15.2
2455477.993452	+149	±19.9
2455477.995782	+36	±13.8
2455477.998113	+73	±20.5
2455478.000443	+88	±22.4
2455478.002774	+49	±33.5
2455478.005105	+48	±22
2455478.007435	+34	±30.8
2455478.009766	+82	±20
2455478.014909	+23	±13.8
2455478.017240	-14	±17.2
2455478.019727	+4	±27
2455478.022058	-43	±16.3
2455478.024389	-91	±27.9
2455478.027550	-42	±23.2
2455478.029881	-25	±46.1

Table .3.: Radial velocities with errors of PTF0724

G. Proper motion & kinematics of PTF0724

PTF0724 is the faintest HW Vir type system with derived parameters. The distance was calculated to 4.4 ± 0.4 kpc. Therefore this system is a good candidate to be member of the old halo population. However, a detailed kinematic analysis is crucial. To determine the kinematics of PTF0724 in our galaxy, it is important to know its proper motion and its distance. Together with the radial velocity of the system, its trajectory can be calculated.

To calculate the proper motion we compared the position of the system to a reference background at many different epochs. The general procedure is described e.g. in Tillich et al. [2010]. We used the photographic plates listed in Table .4, obtained from the Digitized Sky Survex [1].

Survey	Epoch	Plate	Exp. Time (min)
POSS-I O	1955-03-22	XO482	12
POSS-E Red Plate	1955-03-22	XE482	50
Quick-V Northern	1985-01-18	N482	20
POSS-II Red	1989-01-28	XP629	90
POSS-II Red	1989-11-06	XP701	70
POSS-II N	1995-11-17	XI629	90
POSS-II Blue	1996-11-13	XJ629	55
POSS-II Blue	1998-01-27	XJ701	35

Table .4.: Overview of plates used for calculating the proper motion

One of the plates served as a reference and we selected 70 objects. Their position was determined by fitting 2-dimensional Gaussians to the center of the brightness distributions. The same objects were selected on all plates. By comparing the position of the objects on every plate with the reference plate we were able to identify moving objects. Normally galaxies are used as background reference objects. Unfortunately the position around PTF0724 has not been covered by the SDSS survey yet. Therefore there are no information available if an object is in fact a galaxy or only a faint star. For this reason it was decided to measure lots of potential galaxies and compare their position for the different epochs. If the detected movement was within the accuracy of the measurement the object was used as a reference, otherwise it was erased from the sample.

Figure .9 shows the relative position of PTF0724 in miliarseconds for different epoches. A linear fit was used to determine the proper motion to $PM_x = -1.771 \pm 4.68$ mas yr^{-1} and $PM_y = 4.984 \pm 6.41$ mas yr^{-1}. This means that the proper motions is consistent with zero. To be able to determine the kinematics of PTF0724 with regard to the Galactic plane we calculated the radial velocity $U = -43.022 \pm 38.176$ km s^{-1} and the rotational velocity $V = 363.492 \pm 124.763$ km s^{-1}. A Monte-Carlo simulation with a depth of 10000 was used to estimate the errors. If the proper motion of PTF0724 is assumed to be exactly zero, the value for the radial velocity is $U = -72.414$ km s^{-1} and the rotational velocity is $V = 256.441$ km s^{-1}.

Figure .10 shows the position of PTF0724 in an U-V-Diagram with respect to a

---

[1] https://stdatu.stsci.edu/cgi-bin/dss_plate_finder

$$PM_x = -1.771436 \pm 4.675681 \text{ mas yr}^{-1}$$
$$PM_y = 4.984222 \pm 6.413180 \text{ mas yr}^{-1}$$
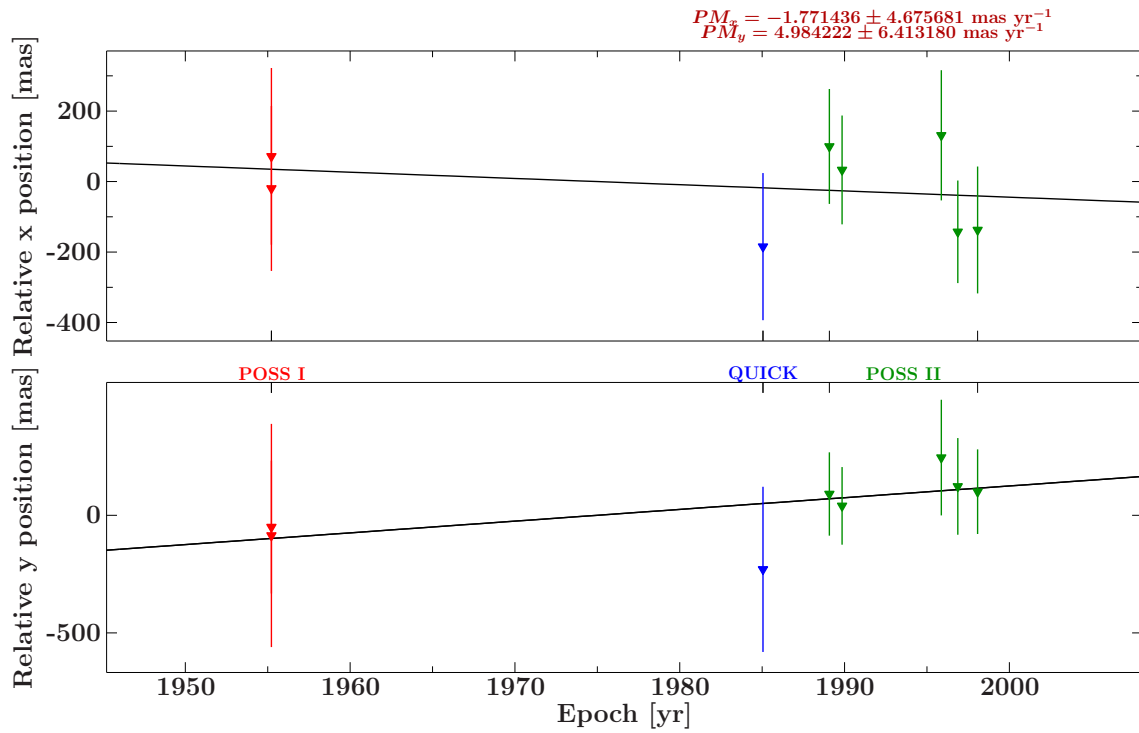
Figure .9.: Proper motions for PTF0724

sample of 398 white dwarfs taken from the SPY-Project [Pauli et al., 2005]. The positions for both possible pairs of Galactic velocities are shown. In addition the 3σ limits for the thin and the thick disk are displayed. If a star is placed outside of the
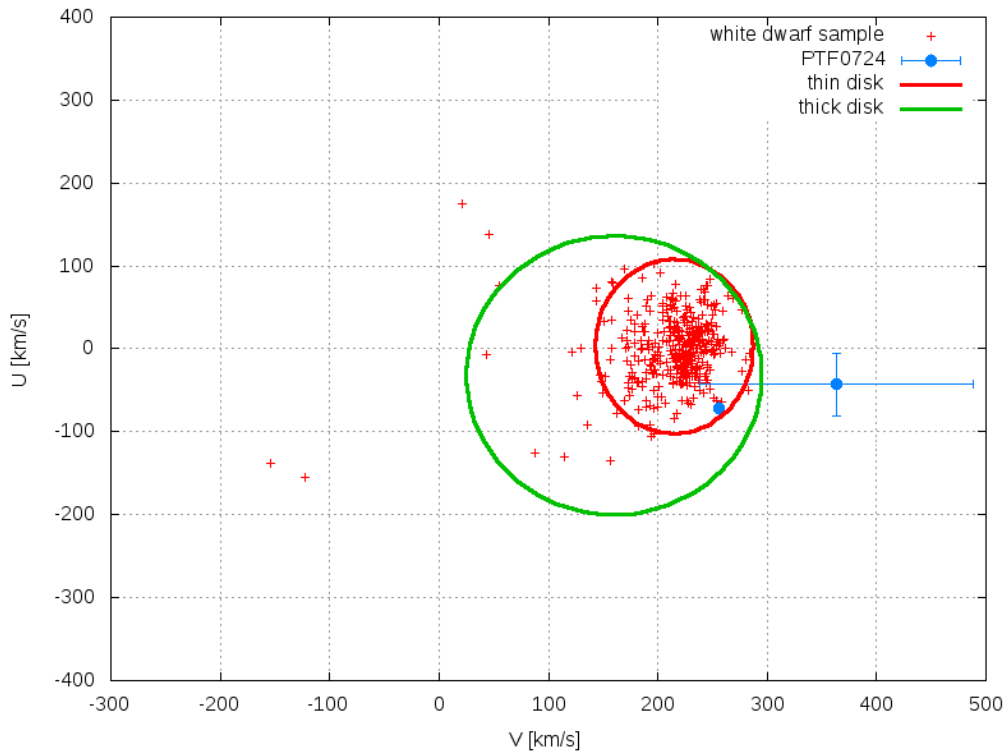
Figure .10.: U-V velocity diagram for PTF0724, position for a proper motion of zero is shown without errorbars, adopted from Pauli et al. [2005]

limits for the disk it must be a halo object. Stars within the limits may belong to the disk, but can also be halo objects.

Because of the large error margins for the rotational velocity, it is somewhat difficult to decide if PTF024 is a halo object or not. But as a disk star moving ahead of the thick disk would be very unlikely, PTF0724 is indeed most likely a halo object, therefore belonging to population I. This conclusion is supported by some of the orbital tracks that were calculated with the MC simulation mentioned above and exceeded a distance of 10 kpc from the galactic plane.

A discussion for the effect of the halo position on the properties and the evolution of PTF0724 is omitted here, as no examinations of other HW Vir system concerning this topic have been published so far.

Erklärung

Hiermit bestätige ich, dass ich diese Arbeit selbstständig und nur unter Verwendung der angegebenen Hilfsmittel angefertigt habe.

Bamberg, den 27.11.2014

Markus Schindewolf